INVESTIGATION OF SHORT FATIGUE CRACK GROWTH AND DAMAGE TOLERANCE IN ADDITIVE MANUFACTURED Ti-6Al-4V

by

Michael C. Waddell

A Thesis

Submitted to the Faculty of Purdue University

In Partial Fulfillment of the Requirements for the degree of

Master of Science in Aeronautics and Astronautics

School of Aeronautics & Astronautics

West Lafayette, Indiana

December 2018

THE PURDUE UNIVERSITY GRADUATE SCHOOL
STATEMENT OF COMMITTEE APPROVAL

Dr. Michael D. Sangid, Chair

School of Aeronautics and Astronautics

Dr. Weinong Chen

School of Aeronautics and Astronautics

Dr. Tyler N. Tallman

School of Aeronautics and Astronautics

Approved by:

Dr. Weinong Chen

Head of the Graduate Program

ACKNOWLEDGMENTS

Undertaking a Masters research program would not be possible without the help and support of many. First and foremost, I wish to pass on my gratitude to my major Professor, Dr. Michael D. Sangid. It was an amazing opportunity to work as a member within Professor Sangid's Advanced Computational Materials and Experimental Evaluation (ACME^2) laboratory. The one on one guidance and support I received were crucial to my completion, the lessons I learnt from his leadership and wealth of knowledge on all things fatigue will last forever. I would like to express my thanks to Dr. Kevin F. Walker, Defence Science and Technology Organization (DSTO), for his considerable time and effort spent encouraging, supporting and providing advice and materials for my research. Having the opportunity to collaborate with and learn from Dr. Walker's substantial experience helped shape and guide my research from day one. To all the members of the ACME^2 laboratory, thank you for the many laughs and the assistance and advice, nothing within this research is possible without your help and input from your own previous works. A number of special mentions are warranted, Alex Mallory and Imad Hanhan for your direct assistance with many sometimes thankless tasks, a number of the results presented within this thesis would not be possible without you. Ritwik Bandyopadhyay your expertise in numerous fatigue related topics and your direct support with data collection and processing of synchrotron data made this work possible. The two experiments conducted at the Advanced Photon Source (APS), Argonne National Laboratory were funded by the United States Department of Energy Office of Science. I appreciatively acknowledge the opportunity to conducted experiments at APS beamlines, 2-BM and 6-BM. A special thank you to the beamline scientists, Dr. Xianghui Xiao, Dr. Jun-Sang Park and Dr. Andrew Chuang for all your help in getting the most out of the allotted beam times. To Rachel Roth and Kenneth Rodriguez among the many things you helped with, your assistance with reconstructing the tomography data was greatly appreciated. Finally thank you to the Royal Australian Air Force for funding my program and making this work possible.

TABLE OF CONTENTS

LIST OF TABLES vii
LIST OF FIGURES viii
ABBREVIATIONS xiii
ABSTRACT xiv
1. INTRODUCTION 1
1.1 Background 2
1.2 Aim and Research Questions 9
1.3 Thesis Overview 9
2. LITERATURE REVIEW 11
2.1 Additive Manufacturing 11
2.1.1 Background 11
2.1.2 Additive Manufacturing 11
2.1.3 Selective Laser Melting – Ti-6Al-4V 13
2.2 X-ray Synchrotron Computed Micro-tomography 23
2.2.1 Background 23
2.2.2 µXSCT Measurement Principles 24
2.2.3 µXSCT Image Reconstructions 25
2.2.4 µXSCT Measurement Applications and Results 26
2.3 High Energy Dispersive Diffraction 26
2.3.1 Background 26
2.3.2 EDD Strain Measurement Principles 28
2.3.3 EDD Strain Measurement Source, Setup and Techniques 29
2.3.4 EDD Strain Measurement Applications and Results 32
2.4 Previous Work 35
2.4.1 Background 35
2.4.2 Results 36
3. SAMPLE MATERIAL AND PRE-CRACKING 38
3.1 Material Properties and Sample Details 38
3.2 Sample Geometry 42

3.3 Elastic Notch Stress Concentration Factor 43
3.4 Pre-cracking....44
4. X-RAY SYNCHROTRON COMPUTED MICRO-TOMOGRAPGHY EXPERIMENTAL METHOD 51
4.1 Background and Overview 51
4.2 In-situ Loading....51
4.3 Sample Mounting 52
4.4 Beam Settings 53
4.5 In-situ Fatigue Crack Growth Experimental Procedure 53
5. X-RAY SYNCHROTRON COMPUTED MICRO-TOMOGRAPGHY RECONSTRUCTIONS 55
5.1 Background and Overview 55
5.2 TomoPy Reconstructions 55
5.3 Pre-processing....56
5.4 Reconstruction 57
5.5 Post Processing 58
5.6 Thresholding and Visualisation 59
6. FATIGUE CRACK GROWTH ANALYSIS AND RESULTS 62
6.1 Background and Overview 62
6.2 Measurement Methods 63
6.3 Crack Growth and Path Evolution 64
6.4 Scanning Electron Microscope Images 67
6.5 Results 71
6.5.1 Crack Deflections, Initiation and Defects....71
6.5.2 Short Fatigue Crack Growth....80
6.5.3 Microindentation Hardness 81
6.6 Discussion 82
7. POROSITY AND LACK OF FUSION ANALYSIS AND RESULTS 86
7.1 Background and Overview 86
7.1 Measurement Methods 86
7.2 Visualization 88

7.3 Scanning Electron Microscope Images 90
7.4 Build Direction 92
7.5 Results 94
7.6 Discussion 96
8. ENERGY DISPERSIVE DIFFRACTION EXPERIMENTAL METHOD 98
8.1 Background and Overview 98
8.2 In-Situ Loading and Sample Mounting 98
8.3 Region of Interest 99
8.4 Beam Settings 101
8.1 Strain Measurement Experimental Method 102
8.2 Strain Measurement Calculations 103
8.3 Strain Measurement Results 104
8.4 Strain Measurement Accuracy 107
9. ENERGY DISPERSIVE DIFFRACTION ANALYSIS AND RESULTS 108
9.1 Background and Overview 108
9.2 Estimate for Plastic Zone 108
9.3 Results 109
9.4 Discussion 114
10. CONCLUSIONS AND RECOMMENDATIONS 116
10.1 Conclusion 116
10.2 Recommendations 118
APPENDIX 119
REFERENCES 122

LIST OF TABLES

Table 1.1. Short crack classifications by characteristic length scales [19], [20], [23]. 5

Table 2.1. ASTM classification and naming conventions of AM methods [7], [8], [42]. 12

Table 2.2. Strain classifications and associated characteristic lengths, adopted from Withers [74]. 28

Table 3.1. Chemical composition of Ti-6Al-4V powder used in SLM applications, manufactured by TLS Technik GmbH & Co in Germany [64]. 38

Table 3.2. SLM build parameters used to manufacture Ti-6Al-4V samples, the difference in energy density is used to differentiate the build conditions as trial or optimized. 39

Table 3.3. Matrix showing the correlated sample number, specimen designation and original CT sample naming conventions, build condition and characterization methods employed. 41

Table 3.4. Non-cumulative fatigue cycle data, per sample, for pre-cracking, in-situ µXSCT, in-situ EDD and fracture as applicable. 49

Table 5.1. List of parameters and the values as inputs for the TomoPy tools used for the reconstructions of raw tomography data. 61

Table 6.1. Summary of the build direction and build condition for samples 1, 2 and 3. 62

Table 6.2. Showing measurements of observed crack deflections, bridging of cracks surfaces and bifurcations for samples 1, 2 and 3. Minimum crack deflection distance reported, 10 μm. 79

Table 6.3. Results from Vickers hardness microindentation testing on two different build conditions.....82

Table 7.1. Volume fraction calculation data and results. Note, all volumes are in $\mu m3$. 88

LIST OF FIGURES

Figure 1.1. Schematic illustration of Paris law and Fatigue Crack growth regimes for Mode I (opening) cracks in metals..... 2

Figure 1.2. Schematic illustration of potential deviations in Short crack growth from the Paris law, showing increased or decreased rates and growth below the ΔK, threshold limit [14]..... 4

Figure 1.3. Crack growth per cycle in depth, a, and length, c, due to grain boundary interactions [29]. 6

Figure 1.4. Short crack growth rates for various ΔK showing the variability in various aluminum alloys alongside the large crack growth data [21], [29], [31]. 8

Figure 2.1. Schematic representation of AM powder bed fusion techniques, adopted from Santos [9].....14

Figure 2.2. Generalized schematic of a powder bed AM process [39]. 15

Figure 2.3. Gong et al. proposed SLM process window for Ti-6Al-4V, with hatch spacing and layer thickness constant (Raymor powder) [51]. 16

Figure 2.4. As built SLM AM Ti-6Al-4V exhibiting a martensitic morphology consisting of fine α'plates, adopted from Cain et al [3]. 17

Figure 2.5. Fine α' microstructure common to AM Ti-6Al-4V, the white dotted lines are suspected former β boundaries, sample was stress relieved with a horizontal build orientation [56]. 18

Figure 2.6. Various energy densities and their corresponding pore characteristics of spherical and irregular, for additive manufactured Ti-6Al-4V [55]. 21

Figure 2.7. Example of LOF defects with or without un-melted powder particles in SLM AM Ti-6Al-4V adopted from Liu et al. [64] 22

Figure 2.8. Showing established trends for resolution and acquisition times for μXSCT facilities[66]. 23

Figure 2.9. Basic μXSCT schematic [67]. 24

Figure 2.10. Resolution and penetration of various residual strain measuring techniques, as of 2012. Grey represents destructive methods [72]. 27

Figure 2.11. A typical schematic for a synchrotron source EDD experiment. (NSLS) [79]. 30

Figure 2.12. Slit configuration experiments are showing the effect on beam spot size and shape, intensity distributions and images of the scattered intensity behind the slit system [80]. 31

Figure 2.13. Schematic of an APS EDD experimental setup, showing beam direction, slits and detectors [77]. 31

Figure 2.14. Diffraction spectrum from stainless steel under 5MPa load, crosses indicate measured data, line fit via a Rietveld method, ticks indicate expected peaks, and lower graph is the difference [82]. 32

Figure 2.15. 316H austenitic steel compact tension sample geometry showing EDD mapped area and diffraction spectrum with inaccurate Gaussian peak fit [73]. 33

Figure 2.16. 316H austenitic steel compact tension EDD elastic strain (ε_{22}) map and strain measurement comparison for EDD, neutron diffraction and FEA [73]. 34

Figure 2.17. Comparison of typical Titanium linear-friction weld residual strain measurements, EDD (left) and Neutron Diffraction (right) [85], [86]. 35

Figure 2.18 Compact tension specimens and build directions. X-Z: Vertical Build and X-Y: Horizontal build [64]. 36

Figure 2.19. Long FCG rates for vertical and horizontal build SLM AM Ti-6Al-4V CT specimens of the same build condition [64]. 37

Figure 3.1. SLM Solutions GmbH, SLM 250HL system similar to the one used to manufacture Ti-6Al-4V samples used within this work [87]. 39

Figure 3.2. Scanning strategy used to manufacture Ti-6Al-4V samples is the alternating bi-directional with 90° rotation each layer. 40

Figure 3.3. Schematic representation of the applicable locations and build directions for the vertical and horizontal samples. 41

Figure 3.4. Diagram schematic of sample geometry in mm, gauge cross section and corner notch positon and dimensions. 42

Figure 3.5. Diagram schematic of samples showing build layers, a vertical sample will always have crack propagation parallel to build layer, horizontal sample has infinite crack propagation direction to build layer orientations. 43

Figure 3.6. Finite element analysis, showing ten–node tetrahedral elements, stressed mesh and local notch yield stress [89]. 44

Figure 3.7. Extract from the Military Handbook (MIL-HDBK-5J), showing S/N curves for annealed room temperature extruded Ti-6AL-4V, with Kt = 2.8, used as an initial estimate for pre-cracking load [91]. 46

Figure 3.8. MTS fatigue test apparatus setup used for all pre-cracking, example of a 20x image showing a crack initiating from notch root on sample 6. 47

Figure 3.9. Indicates axial misalignment when mounting a sample in to the MTS fatigue test apparatus. Sample 6, at 50,000 cycles, crack length is approximately 200 μm and load was 825 N for this image. 47

Figure 3.10. Notch root of sample 4 at 58,000 cycles, unloaded 50 N (left) and loaded 850 N (right) showing confirmation of a crack. 48

Figure 3.11. Data log printout of fatigue cycle testing, showing minimal variation in output variables at 3 Hz, $\sigma min = 50$, $\sigma max = 780$ and $R = 0.06$. Note, these value are close to the stress values tested in this work, data log taken during testing of machine capabilities. 50

Figure 4.1. Experimental setup used for tomography at 2-BM, APS. 51

Figure 5.1. Overview of the TomoPy process steps available for reconstruction and correction of images from raw synchrotron radiographs [93] 56

Figure 5.2. Reconstructed slice (image domain) from sample 1, with notch and crack front evident. Slice without the use of TomoPy tools to remove zingers and stripes/rings (a), and slice showing results after removal (b). 57

Figure 5.3. Rotation center parameter effects shown as incorrect with evidence of blurring, streaking and misalignment (a) and optimized (b). 58

Figure 5.4. Different stages of ring artifact removal are shown, without any ring removal tools (a), Tomopy ring removal showing dark contrast artifacts remaining (b) and reasonably homogenous contrast obtained through the bulk via the Matlab script (c).....59

Figure 5.5. Sample 1 images showing a high correlation of fracture surface features for an SEM image, post complete fracture (a) and a reconstructed tomography scan, Avizo rendering (b). ...60

Figure 6.1. Summary of the notch to build layer orientations for samples 1, 2 and 3. 63

Figure 6.2. Example of Avizo three dimensional renderings of the FCG tomography reconstructions, sample 1 is shown at 120,550 cycles with a crack length of 632 μm.....63

Figure 6.3. Example of the two measurement methods used to obtain the short FCG data, orthogonal measurement, (a), and three dimensional measurement, (b). 64

Figure 6.4. Sample 1 crack evolution, (a-d), and orthogonal views described by the sectioning planes ‘aa’ and ‘bb’. 65

Figure 6.5. Sample 2 crack evolution, (a-d), and orthogonal views described by the sectioning planes ‘aa’ and ‘bb’. 66

Figure 6.6. Sample 3 crack evolution, (a-d), and orthogonal views described by the sectioning planes ‘aa’ and ‘bb’. 67

Figure 6.7. Sample 1 post fracture SEM image (148,269 cycles), (a), and measurement technique for crack growth to final failure (tomography scan at 124,550 cycles), (b). Images (c) and (d) are close up fracture surface views.....68

Figure 6.8. Sample 2 post fracture SEM image (123,548 cycles), (a), with (b) and (c) close up images of the fracture surface.....69

Figure 6.9. Sample 3 post fracture SEM image (140,433 cycles), (a), with (b) and (c) close up images of the fracture surface.....70

Figure 6.10. Sample 1, 3D Avizo rendering and 2D orthogonal slice at the notch root showing three individual cracks at 100,000 cycles at crack length of 135 μm. 71

Figure 6.11. Sample 2, 3D Avizo rendering and 2D orthogonal slice at the notch root showing five individual cracks (and numerous micro cracks) at 78,000 cycles and a crack length of 162 μm.....72

Figure 6.12. Sample 3, 3D Avizo rendering and 2D orthogonal slice at the notch root showing four individual cracks at 73,000 cycles and a crack length of 215 μm.....73

Figure 6.13. Sample 1 at 120,550 cycles, showing steps at free surface and notch root (crack initiation site), a bifurcation has also occurred at the crack front. 73

Figure 6.14. Sample 1, 120,550 cycles showing free surface steps and the entire crack surface..74

Figure 6.15. Different 3D rendering views showing sample 1 crack surface, pores and a bifurcation, in the bottom images the crack is growing from the notch towards the reader. 75

Figure 6.16. Different 3D rendering views showing sample 2 crack morphology, crack growing from the notch towards the reader. 50 μm out from the notch (top) and 90 μm out from the notch (bottom). 77

Figure 6.17. Sample 1, 102,6000 cycles showing a free surface step and the entire crack surface. 77

Figure 6.18. da/dN vs ΔK for compact tension samples with the same notch to build layer orientation as sample 2 (black) and sample 3 (red), adopted from Liu et al. [64]. 80

Figure 6.19. Crack length vs cycles plot for samples 1, 2 and 3. 81

Figure 6.20. Vickers Hardness indentations on sample 2. 82

Figure 7.1. Example of the Avzio data attributed to each identified pore, pore of interest (large green) highlighted by the yellow cross hairs. 87

Figure 7.2. Sample 1 showing pores highlighted in color from the Avizo porosity analysis.....88

Figure 7.3. Sample 2 showing pores highlighted in color from the Avizo porosity analysis.....89

Figure 7.4. Sample 3 showing pores highlighted in color from the Avizo porosity analysis.....89

Figure 7.5. Exploded view of the largest pore seen in sample 3 (purple pore in Figure 7.4).....90

Figure 7.6. SEM images of sample 2 semi spherical porosity (both) showing possible internal ridges (right).....90

Figure 7.7. SEM images of sample 3 elongated and irregular shaped porosity. 91

Figure 7.8. SEM image of sample 3 showing a LOF defect. 91

Figure 7.9. SEM image of sample 5 showing large (> 600 μm) porosity defect as the possible cause for failure at 24,200 cycles.....92

Figure 7.10. Sample 3 likely build layer to notch orientation using LOF defects elongated lengths as indication. Sample schematic from Figure 3.5 shown to illustrate build layers. 93

Figure 7.11. Sample 2, elongated porosity defects evident from the SEM images in the fast fracture region, used to infer the build direction. Sample schematic from Figure 3.5 shown to illustrate build layers.....94

Figure 7.12. CDF plot of pore volumes with a minimum threshold set at 27 voxels. 95

Figure 7.13. CDF plot of the sphericity of all pores above the minimum threshold of 27 voxels. 95

Figure 8.1. Experimental setup used for EDD at 6-BM, APS.....99

Figure 8.2. EDD grid on region of interest only (sample not shown), showing beam spot size of 30 x 30 μm, with a 5 μm overlap. The total number of grid locations was 6 x 24 which resulted in a 155 x 630 μm region of interest. To note, the elongated (2-3 mm) gauge volume length in the beam direction. Coordinate system is the fixed lab system. 100

Figure 8.3. Chosen region of interest overlaid on a schematic of the sample, showing interaction with propagating crack front. Three coordinate systems, two fixed to the sample and one fixed to the lab are also depicted. 101

Figure 8.4. FCG propagation into the region of interest used for EDD experiment. Total fatigue cycles between each load step is 2000 cycles. Crack growth was approximately 150 μm total. 102

Figure 8.5. Results from an unloaded EDD line scan far from the gauge volume, showing inter-planar spacing corresponding to the third α peak. Fitted with a normal distribution the mean value of 2.22598 Å is used for the strain free lattice parameter estimate. 103

Figure 8.6. Sample rotation coordinate system used during EDD experiment. 104

Figure 8.7. Rotation angles used during EDD sample, three Ω angles with three χ angles for each Ω were used for a total of nine unique configurations. 104

Figure 8.8. Example of a diffraction pattern obtained, peak fit via MATLAB Pseudo-Voight function shown in red. 105

Figure 8.9. Figure 8.10. Showing the accuracy of the inversion process as sensitive to Ω0 rotation [77]. 107

Figure 9.1. Load step 3 tomography scan of the region of interest, all porosity throughout the volume collapsed onto the (1, 2) plane, crack and pores shown in blue. 109

Figure 9.2. Sample 1, load step 1, EDD strain component contour plots (top) and region of interest tomography scans (bottom). Load at 825 N and total cycles 120,550. 110

Figure 9.3. Sample 1, load step 2, EDD strain component contour plots (top) and region of interest tomography scans (bottom). Load at 825 N and total cycles 122,550. 111

Figure 9.4. Sample 1, load step 3, EDD strain component contour plots (top) and region of interest tomography scans (bottom). Load at 825 N and total cycles 124,550. 112

Figure 9.5. Sample 1, EDD strain component contour plots (top) and region of interest tomography scans (bottom). Load at 0 N and total cycles 124,550. 113

ABBREVIATIONS

ACME^2	Advanced Computational Materials and Experimental Evaluation
DSTO	Defence Science and Technology Organization
SLM	Selective Laser Melting
FCG	Fatigue Crack Growth
μXSCT	X-ray Synchrotron Computed Micro-Tomography
EDD	Energy Dispersive Diffraction
LEFM	Linear Elastic Fracture Mechanics
AM	Additive Manufactured
SIF	Stress Intensity Factor
μ-CT	Computed Micro-Tomography
FF-HEDM	Far-Field High Energy Diffraction Microscopy
NSLS	National Synchrotron Light Source, United States
APS	Advanced Photon Source
CME2	Copley Motion Explorer 2 V7.0
CDF	Cumulative Distribution Function
LFW	Linear Friction Welding
VH	Vickers Hardness

ABSTRACT

Author: Waddell, Michael, Waddell. MSAAE
Institution: Purdue University
Degree Received: December 2018
Title: Investigation of Short Fatigue Crack Growth and Damage Tolerance in Additive Manufactured Ti-6Al-4V
Committee Chair: Michael D. Sangid.

Aeronautical products additively manufactured by Selective Laser Melting (SLM), are known to have fatigue properties which are negatively impacted by porosity defects, microstructural features and residual stresses. Little research is available studying these phenomena with respect to the short fatigue crack growth (FCG) inconsistency problem, the large focus being on the long FCG. This thesis seeks to add useful knowledge to the understanding of the mechanisms for short crack growth variability in SLM manufactured Ti-6Al-4V, with the two variables for the process conditions and build directions investigated. An in-situ FCG investigation using x-ray synchrotron computed micro-tomography (μXSCT) was used to visually observe and quantify the short crack path evolution. Crack growth, deflections and porosity interactions were noted and discussed in relation to microstructure, build layer thickness and build layer orientation. A novel use of in-situ energy dispersive x-ray diffraction (EDD) was able to show the lattice strains evolving as a propagating crack moved through a small region of interest. The results presented show the ability to reliably obtain all six elastic strain tensor components, and interpret useful knowledge from a small region of interest.

There are conflicting views in literature with respect to the damage tolerance behavior of as built SLM manufactured Ti-6Al-4V. In the 2018 review by Agius et al., the more prominent studies were considered with Leuders et al. showing the highest long FCG rates for cracks parallel to the build layer and Cain et al. showing cracks propagating through successive build layers as highest [1]–[3]. Cain et al. and Vilaro et al. report significant anisotropy in long FCG for different build orientations whereas Edwards and Ramulu present similar FCG behavior for three different build directions [2]–[5]. Kruth et al. concluded that for optimized build parameters without any (detectable) pores, the building direction does not play a significant role in the fracture toughness

results [6]. All of the mentioned literature reported α' martensitic microstructures and the presence of prior β grain structures for as built SLM Ti-6Al-4V.

No studies to the authors knowledge have considered the short FCG of SLM manufactured Ti-6Al-4V and its implications to the conflicting damage tolerance behaviors reported in literature [1]. In this work small cross-sectional area (1.5 x 1.5 mm) samples in two different build conditions of as built SLM Ti-6Al-4V are studied. The short FCG rate of three different build directions was considered with cracks parallel to the build layers shown to be the most damaging. The microstructure and build layer are shown to be the likely dominant factors in the short FCG rate of as built Ti-6Al-4V. In terms of porosity, little impact to the propagating short crack was seen although there is local elastoplastic behavior around these defects which could cause toughening in the non-optimized build parameter samples tested. The fracture surfaces were examined using a Scanning Electron Microscope (SEM) with the results showing significant differences in the behavior of the two build conditions. From the microindentation hardness testing undertaken, the smooth fracture surface of the optimized sample correlated with a higher Vickers Hardness (VH) result and therefore higher strength. The non-optimized samples had a 'rough' fracture surface, a lower VH result and therefore strength. Furthering the knowledge of short FCG in SLM manufactured Ti-6Al-4V will have positive implications to accurately life and therefore certify additive manufactured aeronautical products.

1. INTRODUCTION

As an emerging technology, additive manufactured (AM) materials quickly garnered interest in the aerospace industry for their potential comparative manufacturing advantages over conventional methods [7]. Notably, the ability to create layer-wise complex geometries and material properties, that can be customized or functionally graded, has driven current research interests [8], [9]. We are already seeing the impact of this research as direct changes to the engineering product life cycle. These changes are evident by the compressed timeframe for prototyping, rapidly manufactured individual and small-batch end use products and an overall cost reduction in manufacturing and prototyping tooling [10]. Although many of the AM methods have already seen decades of development, it is the recent proliferation of commercially available systems that has the aerospace industry investing heavily in these technologies [11].

As a highly regulated industry, the numerous commercially available systems and constantly improving technologies has presented an issue to aerospace organizations. This rapid growth has meant a set of fully mature design principles, manufacturing guidelines and standards is not necessarily readily available or reflective of recent advancements. These are required before widespread certification and acceptance into service of AM products is seen, particularly in safety/fatigue critical applications [8].

With the 1970's introduction of damage tolerance design requirements (after numerous accidents and reviews, ref [12]), aeronautical products were assumed to have an initial undetectable flaw and the growth to detectable size, then to failure, analyzed to provide a useable life [12], [13]. Similarly, to conventionally manufactured metals and alloys, AM products exhibit significant variation in fatigue life, particularly for short cracks. This variability leads to reductions in fatigue life for aeronautical products and upwards cost drivers for the engineering product life cycle. Understanding the short crack growth properties for AM materials is an important step in furthering the use of this emerging technology.

1.1 Background

Linear Elastic Fracture Mechanics (LEFM) is the most common framework used to understand the propagation of fatigue cracks in engineering metals and alloys used in aerospace applications. There proceeded a number of important advancements leading up to the 1960's when Paris used LEFM to suggested a relationship between crack growth rate, $\frac{da}{dN}$ and stress intensity range, ΔK. Equation 1.1. states the Paris power law relationship, C and n are constants related to material properties [14].

$$\frac{da}{dN} = C(\Delta K)^n \tag{1.1}$$

From Paris's work, there are three distinct regimes of fatigue crack growth, Threshold Regime (I), Paris Regime (II) and Final Fracture (III). Figure 1.1 illustrates the regimes and applicability of the Paris relationship to the Paris Regime, a straight line on a log-log plot.

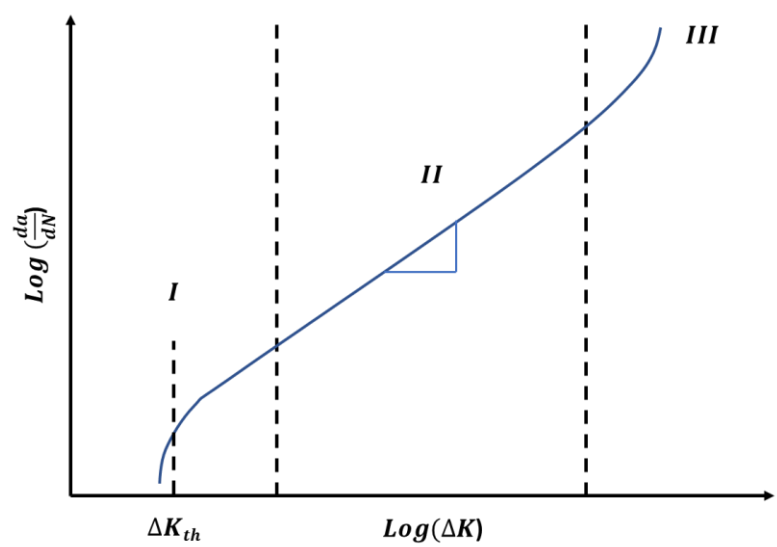

Figure 1.1. Schematic illustration of Paris law and Fatigue Crack growth regimes for Mode I (opening) cracks in metals.

Regime I is typically described as the 'initiation' phase or 'stage I' and is mainly concerned with short crack propagation. Regime I is considered intra-granular in nature for typical ambient environments and crack behavior is highly dependent on microstructural characteristics. Regime

II is the 'propagation' phase, where long crack propagation is well modelled by the Paris law and this stable crack growth is insensitive to the microstructure. Regime III is the unstable fast crack propagation phase which leads to final fracture.

Prior to the Paris law relationship researchers had sought to gain an understanding of the stress fields near the tip of a crack. Traced back to the thermodynamic energy arguments for crack advancement, postulated by Griffith and extended through the 1950's by Orowan and Irwin, two energy components for the creation of new surfaces were discovered [15], [16]. The surface energy by Griffith and the more dominant energy, that absorbed by plastic deformation. Irwin then proceeded to study stress fields near the crack tip of 5 different cracked plate configurations, in all cases Irwin discovered that at a relatively small distance from the crack tip the stress distributions matched [17]. Equation 1.2 and 1.3 are the form of Irwin's results for stress in the y axis, σ_y and x axis, σ_x, K is the stress intensity, v is Poisson's ratio and σ_{ox} is a superimposed uniform compression.

$$\sigma_y = \frac{K}{\sqrt{2\pi r}} \cos\frac{\theta}{2}\left\{1 + sin\frac{\theta}{2}\sin\frac{3\theta}{2}\right\};\ as\ r \to 0 \tag{1.2}$$

$$\sigma_x = \frac{K}{\sqrt{2\pi r}} \cos\frac{\theta}{2}\left\{1 + sin\frac{\theta}{2}\sin\frac{3\theta}{2}\right\} - \sigma_{ox};\ as\ r \to 0 \tag{1.3}$$

Equation 1.4 is Irwin's Stress Intensity Factor (SIF) with, K stress intensity, $f(g,a)$ a non-dimensional factor dependent on geometry of cracked component and crack length, σ the reference stress and a the crack half-length (or radius for penny-shaped cracks). It was by taking the range of this stress intensity K, from the applied stress, that Paris was able to illustrate his relationship for crack growth per cycle.

$$K = f(g,a)\sigma\sqrt{\pi a} \tag{1.4}$$

A clear limitation of the Paris law is the ability to characterize or quantify the crack growth rate of small cracks within the Threshold Regime. It is understanding this regime that has attracted considerable research, as the majority of the fatigue life of metals and alloys used in aerospace

applications can occur within. As far back as 1979, researchers such as Schijve had shown that for metals and alloys with a polished surface, crack initiation through to 100µm in size can account for more than 60% of total life [18]. Furthermore, a significant amount of research is available that highlights the large variability in growth rates within this regime, this includes statements from Miller and Suresh implying that the use of extrapolated long crack growth data can lead to significantly non-conservative fatigue life predictions [19], [20].

In 1975 Pearson conducted a set of experiments on commercial aluminum alloys and very clearly concluded that short crack growth was anomalous, it differs from that of long cracks [21]. Since then it has been shown that short crack growth rates can increase or decrease as stress intensity range increases, including complete arrest for low driving forces. Figure 1.2 shows examples of these deviations within the Threshold Regime, as suggested by Donahue et al [22]. Short cracks can be observed growing at stress intensities lower than those associated with the long crack threshold value, ΔK_{th} [19], [20]. Finally, for cracks with a characteristic length similar to grain size, boundary effects and tortuosity of the crack path play a significant role in the crack growth rate. These effects can even cause complete arrest as obstacles may require an accumulation of damage great enough to propagate past.

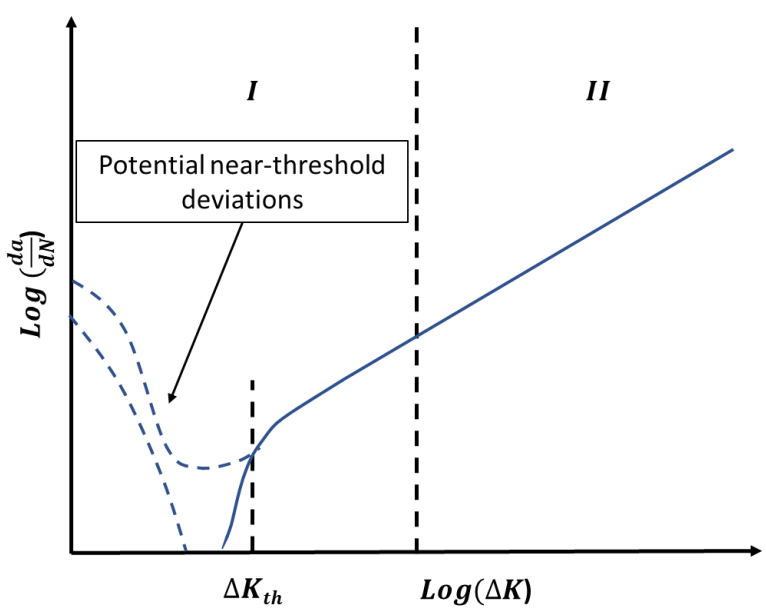

Figure 1.2. Schematic illustration of potential deviations in Short crack growth from the Paris law, showing increased or decreased rates and growth below the ΔK, threshold limit [14].

In order to understand the behavior of short cracks a classification system is required, Table 1.1 contains small crack classifications adopted from several different versions suggested by Suresh, Ritchie and Miller [19], [20], [23].

Table 1.1. Short crack classifications by characteristic length scales [19], [20], [23].

Small crack classification	**Characteristic length (a)**	**Characteristic length property**
Mechanically small	$a \approx r_p$	Comparable to local plastic zone size, r_p (Linear elastic fracture mechanics limitation)
Microstructurally small	$a \approx d_{grain}$	Comparable to grain diameter, d_{grain} (Continuum mechanics limitation)
Physically small	$a < 1\,mm$	Physical property only, large impact from crack closure
Chemically small	$a < 10\,mm$	In reference to local crack tip environmental effects

Major mechanisms that influence the short crack growth variability in the Threshold Regime are generally accepted to be crack closure, local plasticity, crack tip plastic zone, 3d crack propagation, crack driving force and microstructural features [19], [20], [23], [24]. Microstructural features can include grain size, grain boundaries, texture, and the volume fraction, size, and shape of inclusions, defects, particles and porosity. As per Table 1.1 the size classification of a small crack also has to be taken into account when trying to understand which of the afore-mentioned mechanisms for variability is most applicable.

Numerous researchers have shown that microstructurally small cracks are significantly influenced by their microstructural features, starting with Forsyth who showed that initiation and short crack growth can begin within a single slip system [25]. McEvily and Boettner showed there is a relationship between grain orientation and fatigue crack growth [26]. Yoder et al. discusses the variability in Irwin's SIF, finding that the grain size is directly related to threshold value, ΔK_{th} for polycrystalline materials [27]. Navarro and de los Rios's research considers that the microstructurally short crack growth rate is dependent on the confinement of the crack tip plastic zone by grain boundaries or other dislocation impeding obstacles [28]. Allen et al. describes the

direction of crack growth, as the threshold value is approached, as tending to be crystallographic in nature [17].

As the short crack growth path is typically three-dimensional the microstructural impacts from interactions with grain boundaries is different with respect to depth, a, and crack length c. Even if the crack length is impeded by a grain boundary the crack depth, a, may still be growing [29], [30]. Figure 1.3 depicts this phenomena, as the cracks grow beyond the microstructurally small length scale the grain boundary influence is lessened [29]. As short crack growth variation cannot for certain be entirely explained by grain size and orientation, in general researchers conduct probabilistic assessments to assess the impact to growth rates [29], [31]. There is limited recent advancements in the study of short crack growth variability caused by microstructural features. One area of research by Rovinelli et al. looked at cycle by cycle data of short crack growth combined with crystal plasticity simulations and machine learning, the resulting model was shown to accurate predict the direction of short crack growth propagation [32].

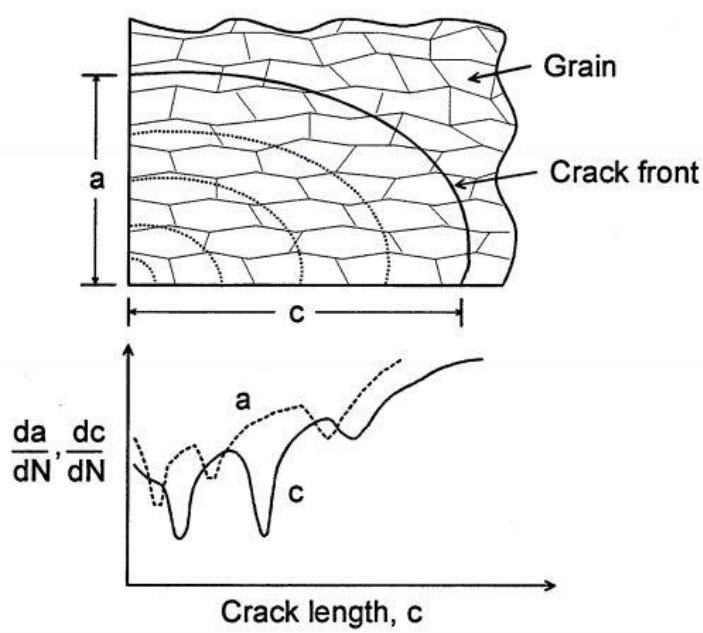

Figure 1.3. Crack growth per cycle in depth, a, and length, c, due to grain boundary interactions [29].

When considering the characteristic length scales of short cracks, highlighted in Table 1.1, we can say that all engineering materials would appear anisotropic and inhomogeneous. This can be due to porosity, voids or inclusions and not only because of the inherent grain structure. The effect of this is a localization of stress which can cause crack initiation, this is primarily a surface or near surface mechanism due to highest local stresses and stress concentrators. Very early on a number of researchers showed inclusion driven crack initiation over slip band mechanisms is commonplace and this impacts the crack growth rates in Regime I [33]–[35]. Again there is limited recent advancement in the understanding and modeling of this phenomenon. In one study reviewed Naragani et al. successfully used absorption contrast computed micro-tomography (μ-CT) and far-field high energy diffraction microscopy (FF-HEDM) to study crack nucleation conditions around inclusions in a Ni-based superalloy [36].

Crack closure is a long established phenomenon with varying agreement between the magnitude of short crack growth rate variability that can be attributed to it. Elber first observed that fracture surfaces contact during positive R ratio tests [37]. Since the discovery of this plasticity induced crack closure other mechanisms such as surface roughness and corrosion of the crack surfaces have been studied. Newman's model for crack closure (or lack of closure within short cracks) has been shown to have the potential to explain some of the short crack behavior [30].

Overall the mechanisms discussed manifest in the results shown in Figure 1.4, Pearson's original anomalous short crack growth are plotted, with Lankford's data for various aluminum alloys as well as the large crack growth data for comparison [21], [31]. From this we can clearly see the link between the deviations of short crack growth rate within Regime I and the total life estimations given by damage tolerant design methods.

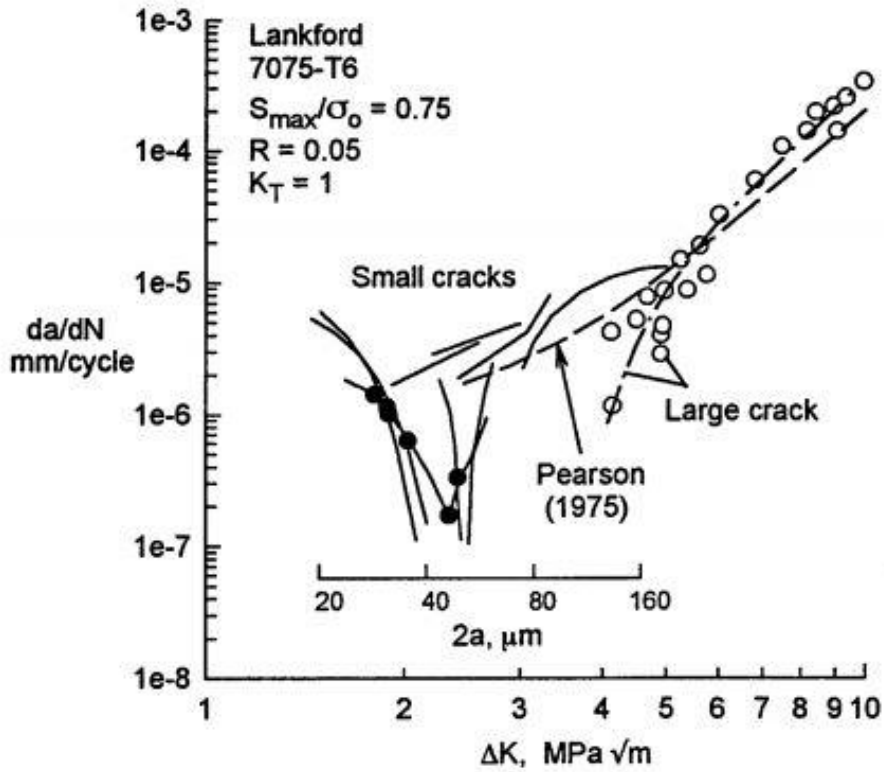

Figure 1.4. Short crack growth rates for various ΔK showing the variability in various aluminum alloys alongside the large crack growth data [21], [29], [31].

The initial flaw size assumed by damage tolerance design methods is relatively large, normally around 1.27 mm [12]. Current methods used to determine damage tolerance crack growth are described in ASTM E647 tests, typically the accuracy of these predictions are related to the $\frac{da}{dN}$ and adjusted ΔK inputs [38]. The current ASTM load reducing approaches have issues that can result in overestimated thresholds and the crack closure corrected methods can produce a curve that doesn't correctly represent the small crack growth seen in experiments. Similarly, to crack closure methods, the compression pre-cracking methods can also not account correctly for all the crack tip shielding mechanisms. These shortcomings along with the considerable cost to conduct the necessary short crack tests has led researchers to look for other methods.

With the recent advancement of higher energy synchrotron source imaging techniques, researchers are now able to more accurately assess the mechanisms for short crack variability. By conducting in-situ loading experiments on aerospace engineering materials, short cracks can be imaged in

three-dimensions. These tomography scans can be taken at intervals of loading steps in order to study crack evolution. Energy dispersive diffraction techniques can be used to study residual strain, crack tip strain and strain evolution during fatigue cycling. Potentially the greater the understanding gleaned using these techniques the greater the chance we have to improve the accuracy of life predictions by damage tolerant design.

1.2 Aim and Research Questions

The aim of this research is to investigate the short fatigue crack growth and damage tolerance properties of AM Ti-6Al-4V. A particular focus is on these behaviors, when the associated AM defects such as lack of fusion (LOF) bonding, pores and anisotropies due to build direction and microstructure are present. To investigate, two high energy synchrotron characterization methods are employed, Energy dispersive x-ray diffraction (EDD) and high-resolution synchrotron-based computed micro-tomography (μXSCT). The following questions are considered: What is the mechanisms that impact the damage tolerance properties of AM materials? Can EDD be utilized to explain and further our understanding of the differences in short crack growth between AM samples of varying build conditions?

1.3 Thesis Overview

This thesis contains 10 sections. Section 2 is used to review the current literature related to additive manufacturing of Ti-6Al-4V, explain and review the relevant synchrotron techniques and give an overview of previous work on the studied material. Section 3 is used to detail the material used including sample production, composition, geometry and pre-cracking procedure. Two separate synchrotron techniques were used, Sections 4 and 5 discuss the μXSCT experiment and post processing steps taken for reconstructions and image processing of the acquired data. The EDD experimental method is covered in Section 8. The results are discussed separately through Sections 6, 7, and 9. Section 6 contains the short FCG results including crack deflection and porosity interactions. Section 7 covers the porosity analysis and Section 9 the EDD results. Section 10 concludes this work with a summary and recommendations.

Throughout this work a number of equations are used and stated explicitly, the symbols within these equations are defined within the work immediate prior or post. This was required as a number of the equations have different conventions for the same variable. Therefore, there is no standard list of symbols.

2. LITERATURE REVIEW

2.1 Additive Manufacturing

2.1.1 Background

Of the many additive manufacturing processes, Selective Laser Melting (SLM) is one of the most commonly used and is deemed most promising for Ti-6Al-4V aerospace engineering products [2], [3], [39]–[41]. SLM manufactured Ti-6Al-4V is the chosen material and method of manufacturing for this research as these are an area of significant recent advancements, highlighted in literature. The previous research reviewed has considered fatigue properties, mechanical properties, surface attributes such as roughness, the impact of post processing on inherent density and porosity, microstructural characterization and the overall fit for purpose of SLM manufactured Ti-6AL-4V. Understanding the fatigue properties of SLM manufactured Ti-6Al-4V requires characterization methods, this research focused on the use of μXSCT and EDD.

2.1.2 Additive Manufacturing

Rapid prototyping, rapid manufacturing, additive fabrication, additive processes, freeform fabrication and direct digital manufacturing are an example of the series of synonyms used within literature to describe the same manufacturing process [7]. The term “additive manufacturing” was chosen as the standard by the associated ASTM committee, the premise being that other manufacturing methods employ some form of “subtractive” processes such as cutting, milling or grinding [42]. The basic principle of all AM processes is the fabrication of products by adding material in cross-sectional layer by layer steps. Generally, a three-dimensional model of the required product is created using design software and then broken into layer by layer slices (at a resolution as required by the AM layer thickness). Each layer of material is deposited as per the model and if required an energy source is used to fuse the subsequent layers. There is research into non-layer by layer AM which may revolutionize these manufacturing methods, this area of research is not covered within this work [43].

AM as a manufacturing means has been around for nearly three decades, a typical early 1990s breakdown of AM processes classifies them as liquid based, solid based and powder based [39],

[44], [45]. To further detail the classifications, ASTM has produced its own classification including naming convention of technologies, power sources and pros/cons; Table 2.1 states the seven ASTM committee agreed categories and associated information adopted from ASTM international [7], [8], [42]. The processes differ in terms of the technique used to deposit layers and the intra layer bonding mechanism.

Table 2.1. ASTM classification and naming conventions of AM methods [7], [8], [42].

Categories	**Technologies**	**Materials**	**Energy Source**	**Pros**	**Cons**
Material Extrusion	Fused Deposition Modeling (FDM)	Thermoplastics, Ceramic slurries, Metal pastes	Thermal Energy	Inexpensive extrusion machine	Limited quality of parts
	Contour Crafting				
Powder Bed Fusion	Selective Laser Sintering (SLS)	Polyamides / Polymer	High-powered laser beam	High accuracy, fully dense parts, high material properties	Powder handling, support and/or substrate complexities
	Direct Metal Laser Sintering (DMLS)	Atomized metal powder (Stainless Steel, Cobalt Chromium, Titanium) and Ceramic powder			
	Selective Laser Melting (SLM)				
	Electron Beam Melting (EBM)		Electron beam		
Vat Photo-polymerization	Stereolithography (SLA)	UV curable resin, Ceramics, Wax	Ultraviolet laser	Build speed, resolution	Over curing, scanlines within product, high cost
Material Jetting	Polyjet / Inkjet Printing	UV curable resin, Wax	Thermal energy / Photocuring	Multi-material printing, surface attributes	Low strength materials
Binder Jetting	Indirect Inkjet Printing (Binder 3DP)	Polymer powder (plaster, resin), Ceramic powder, Metal powder	Thermal Energy	Color range of material, wide material selection	High level of porosity
Sheet Lamination	Laminated Object Manufacturing (LOM)	Plastic film, Metallic sheet, Ceramic tape	Laser beam	Surface attributes	Low cost
Directed Energy Deposition	Laser Engineered Net Shaping (LENS), Electronic Beam Welding (EBW)	Molten metal powder	Laser beam	Can repair parts, functional gradients possible	Post processing required

There is a series of generic characteristics to all (or most) of the AM categories which highlight the improvements over conventional manufacturing. Design flexibility is arguably the most important feature of AM, the ability to create complex geometries with little added cost has led to numerous potential uses, especially within the bio-medical, aerospace and high-end automotive industries. Generally adding geometric complexities to a design would result in costly tooling, time considerations and other increases to conventional manufacturing costs. Dimensional accuracy is another positive feature of AM, with accuracies that can be on the order of microns. Despite this, work is required to standardize the acceptable and expected tolerances of the various commercial systems; early attempts at benchmark testing have been completed [8].

Time and cost for a production run has meant that AM is better suited to low quantity and one time products, which is why bio-medical, aerospace and high-end automotive applications are favored. In terms of aerospace the buy to fly ratio is very low for AM aeronautical product, due to the near-net shape production, meaning very little waste. The majority of research into AM for metals has concentrated on Ti-6Al-4V, along with other materials commonly used for high strength and/or lightweight applications such as stainless steel, nickel based and aluminum alloys. Future use could be for on demand or on location production of these materials as aeronautical products with the extra benefit of lower supply chain costs.

Current challenges are centered around the limited materials available, inconsistency or repeatability of products produced, scalability due to layer resolution, material heterogeneity and standardization and certification [7], [8]. Herderick commented on all these issues during his 2011 AM manufacturing review, with emphasis on the complex thermal processing cycles linking to microstructure and material properties of AM Ti-6Al-4V alloys [46].

2.1.3 Selective Laser Melting – Ti-6Al-4V

The most promising AM methods for use with metals in aerospace applications is within the Powder Bed Fusion category, with the advantage of producing high resolution features, internal passages (complex geometries) and accurate dimensions [9], [39]. Figure 2.1 is a schematic representation of AM powder bed fusion techniques showing inputs of powder, CAD model and energy source resulting in an end use aeronautical product. The two highlighted methods, SLM

and electron beam melting (EBM) were developed in 1995 and commercial machines were readily available from 2005 [8], [11].

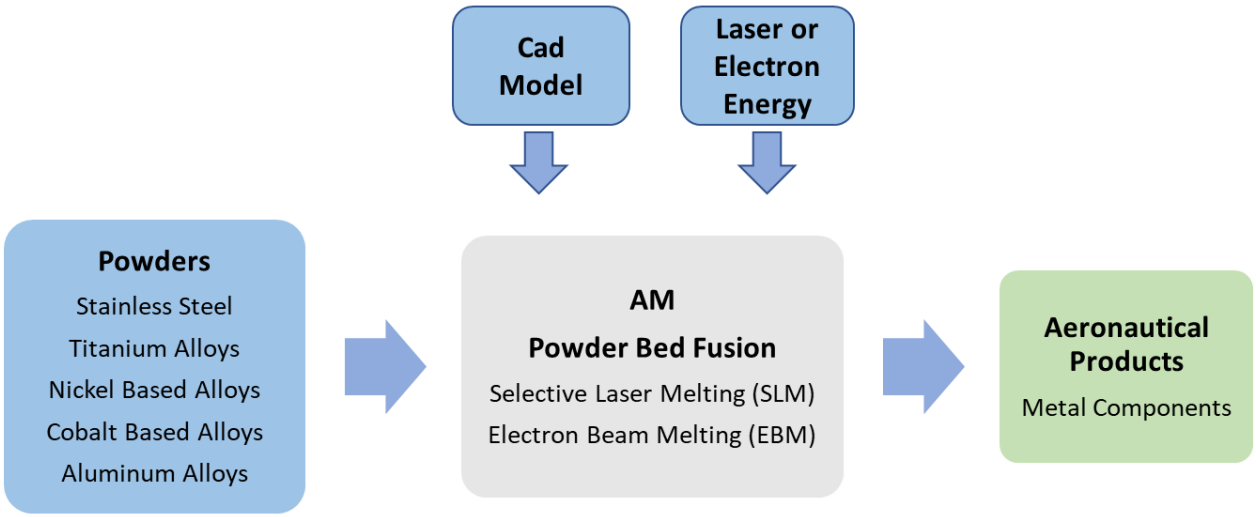

Figure 2.1. Schematic representation of AM powder bed fusion techniques, adopted from Santos [9].

Both methods use an energy source to selectively melt a powder, Figure 2.2 is a generalized schematic of the powder bed process [39]. The roller or rake is used to create a layer of powder within the working area of the beam. The energy source of either an electron beam for EBM, or laser beam for SLM is used to heat and melt the powder selectively in accordance with the CAD model input. The powder bed is then lowered by a preset layer thickness and successive layers of the pre alloyed powders are raked across the work area, the described process is repeated to create the component. This process is carried out within a controlled vacuum for EBM or inert environment for SLM (typically argon), aimed at preventing oxidization.

As SLM manufactured Ti-6Al-4V is by far the most commonly used and extensively investigated AM aerospace application, it will be the focus for the remainder of this literature review [1]–[3], [6], [39]–[41], [45]. The goal for SLM manufactured Ti-6Al-4V is to produce aeronautical products with the highest relative density possible, and a homogenous microstructure; this has proven very difficult, in part due to lack of any mechanical pressure during fabrication [6], [47].

Various researchers have described the inherent defects from SLM processes and their influence on the mechanical properties of AM Ti-6Al-4V [2], [3], [6], [40], [41], [46], [48]–[54]. Broadly the lack of fusion (LOF), un-molten powder and porosity defects are linked to the SLM process parameters and the residual stresses and as fabricated out-of-equilibrium microstructures to the high laser energy, short interaction time and steep temperature gradient [2]–[4], [6].

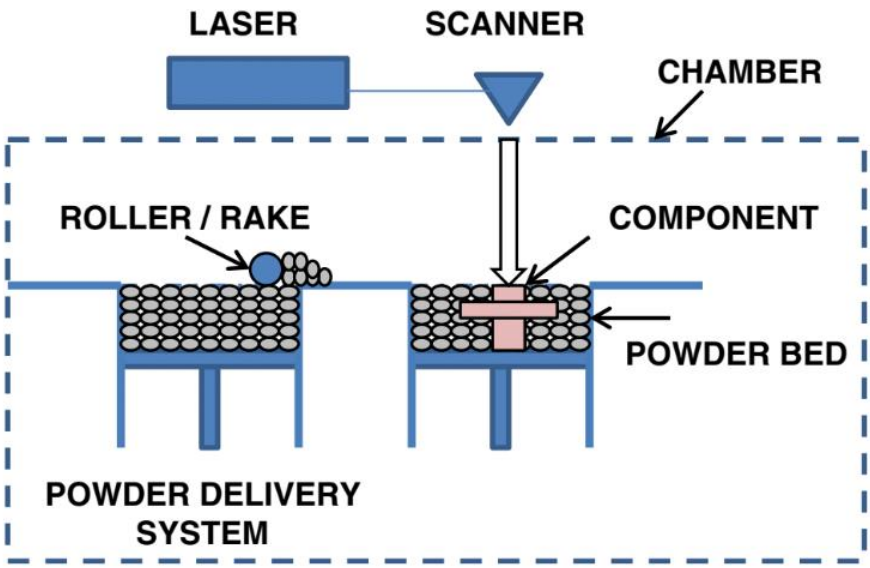

Figure 2.2. Generalized schematic of a powder bed AM process [39].

Considerable effort has gone into optimizing the SLM process to mitigate against the inherent defects and improve material properties. Most researchers agree that there is a direct correlation between the number of defects and the average energy input per volume of material, which is a function of the basic SLM parameters [48], [51], [55]. Equation 2.1 gives the energy density, E_V, and its relation to laser power, P, scanning velocity, v, hatch spacing, h, and powder layer thickness, δ. One obvious failing with this relationship is that the energy introduced by the successive layers is not accounted for [55].

$$E_v = \frac{P}{v\delta h} \qquad \left(\frac{J}{mm^3}\right) \tag{2.1}$$

Kaspervich et al. completed a series of experiments on SLM AM Ti-6Al-4V samples with variations of the scanning parameters, concluding a clear result of scanning velocity being the dominant factor for defect volume fractions [55]. Thijs et al. discussed in detail the influence that the scanning velocity, spot size, and scanning strategy has on the types of defects occurring, although there was no mention of the optimal process parameters required and quantitative mechanical properties were not considered [48]. Gong et al. systematically studied the influence of scanning velocity and laser power on SLM AM Ti-6Al-4V, concluding that there is a significant relation between defect generation and energy density, although it is not linearly correlated [51]. Gong et al. have also proposed a classification system that describes an optimal SLM process window, with hatch spacing and layer thickness constant. Figure 2.3 shows the various classifications, Zone I is fully dense (limited porosity), Zone II is the over melted region, Zone III is the incomplete melting region and Zone OH is the overheated zone.

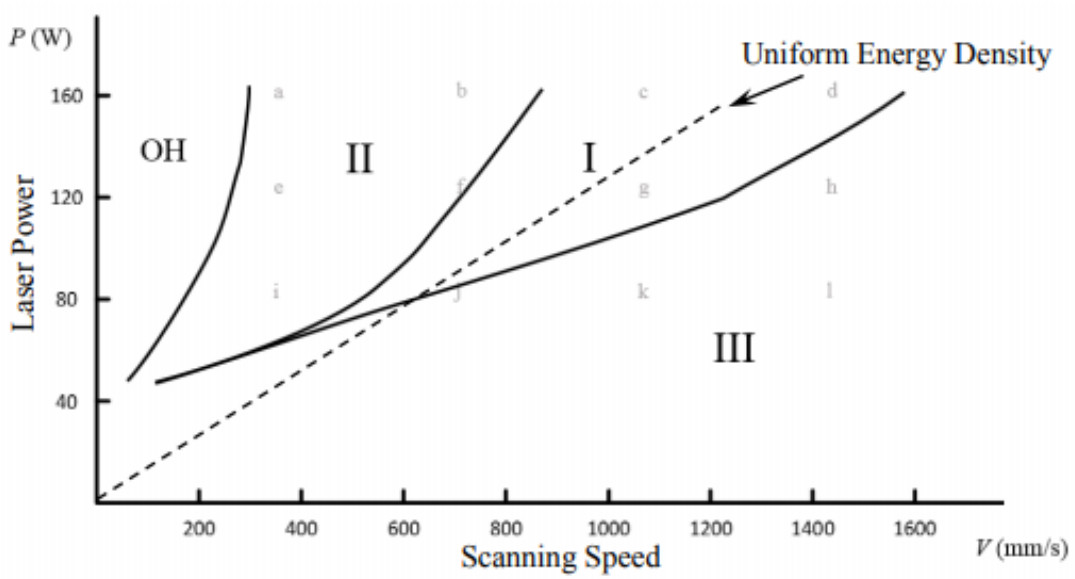

Figure 2.3. Gong et al. proposed SLM process window for Ti-6Al-4V, with hatch spacing and layer thickness constant (Raymor powder) [51].

Kruth discusses the various SLM scanning strategies (such as unidirectional, zigzag, alternating etc), in terms of relative density attainable and number of defects in SLM AM Ti-6Al-4V, with the alternating bi-directional with 90° rotation each layer resulting in the highest relative density [6].

A significant amount of early research concentrated on the influence of process parameters on defects, although a link was also quickly established between process conditions and microstructural properties. It was found that as built SLM AM Ti6Al-4V exhibited a very fine, very textured, non-equilibrium structure, in particular an acicular martensitic phase [4], [6], [47], [48]. Murr et al. demonstrated that the martensitic phase was either an α' or α/α' microstructure and hexagonal close packed, it was also observed that for small build components with a high scanning velocity and therefore cooling rate the $\beta \rightarrow \alpha'$ transformation was dominant [11]. The elongated grains are primarily a function of the partial re-melting during subsequent laser passes [47]. Figure 2.4 shows an example of the fine microstructure of martensitic α' plates typical of AM Ti-6Al-4V [3].

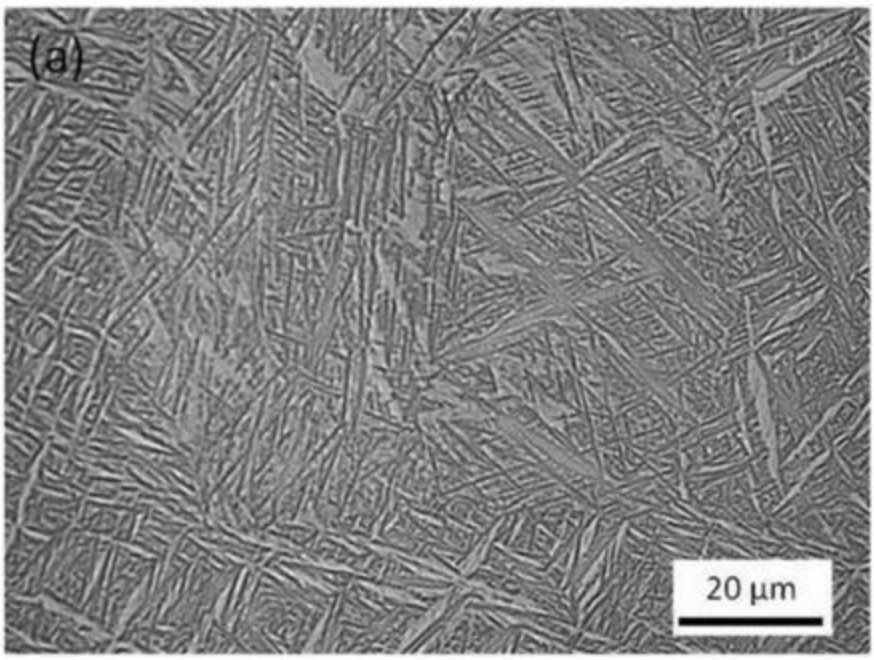

Figure 2.4. As built SLM AM Ti-6Al-4V exhibiting a martensitic morphology consisting of fine α'plates, adopted from Cain et al [3].

Todd and Sangid investigated strain localization, and the role of the former β phase boundaries that enclose regions of highly textured microstructures in AM Ti-6Al-4V [56]. Localization of strain is critical with respect to crack initiation. This study showed that optimizing process parameters to decrease the size of the former β grains and subsequently the textured regions helped resist slip and increase fatigue properties [56]. Figure 2.5 shows an Electron Backscatter

Diffraction (EBSD) characterization result from Todd and Sangid, the fine α' microstructure depicted is common for AM Ti-6Al-4V, the white dotted lines are suspected former β boundaries [56].

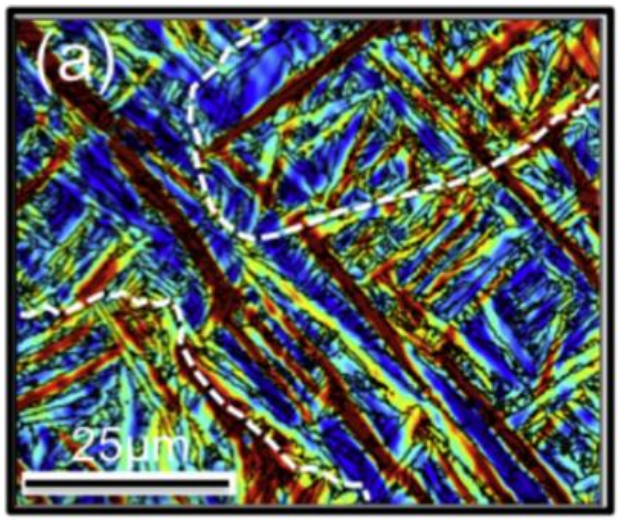

Figure 2.5. Fine α' microstructure common to AM Ti-6Al-4V, the white dotted lines are suspected former β boundaries, sample was stress relieved with a horizontal build orientation [56].

Similar to the optimization of process parameters to limit defects, Thijs et al. demonstrated that different scanning strategies and process parameters can account for variations in grain growth, average grain length and can also cause the precipitation of an intermetallic Ti_3Al phase [48]. A number of studies have also used heat treatments to transform the fine martensitic structure to other preferable microstructures. Improved ductility without severely decreasing the yield strength can be achieved via a lamellar α and β structure [1]. A mixture of fine α and β occurs at around $700\,°C$ and the use of higher temps and added pressure has resulted in a microstructure similar to wrought Ti-6Al-4V, although with elongated grains still evident [47]. Vilaro et al. conducted a series of conventional and optimized heat treatments, the study shows that is possible to choose the morphology of the grains in order to match the in-service loading regime, also highlighted is the strong anisotropy of the mechanical properties due to build direction regardless of any heat treatment [4]. Heat treatment is also beneficial for the reduction of internal stress and when combined with pressure we also see a reduction in the inherent SLM defects. Hot Isostatic Pressing

(HIP) has been shown repeatedly to decrease defect number and size, increase mechanical properties and fatigue resistance [57], [58].

Other than the efforts to optimize the process parameters and the microstructure (mechanical properties) of SLM AM Ti-6Al-4V the other significant theme within open literature is the fatigue resistance. This literature review has found the orientation and types of porosity/defects, residual stresses, build directions and surface properties to be widely covered, although with a number conflicting observations.

Cain et al. and Vilaro et al. report significant anisotropy in FCG for different build orientation and Lueduer et al. shows improved fatigue properties for cracks parallel to the build direction whereas Edwards and Ramulu present similar FCG behavior for three different build directions [2]–[5]. Kruth et al. concludes that for optimized build parameters without any (detectable) pores, the building direction does not play a significant role in the fracture toughness results [6]. Cain et al. explains the anisotropic behaviors as likely to be a function of residual stress [3]. Edward and Ramulu show that residual stress is the dominant variable in the fatigue growth behaviors where Leuders et al. observes that pores and defects are significantly more important than the microstructure for crack initiation [2], [5]. The variability in the number of defects has also lead to contradictory ductility values in relation to build direction comparisons [4], [59]. Wang et al. reported that fatigue cracks initiated at pores close to the surface for wired and arc additive manufactured Ti-6Al-4V [60].

Various fatigue life comparisons to conventionally manufactured Ti-6Al-4V are available in literature, in 2016 Li et al. conducted a thorough assessment of all reported uniaxial fatigue loading results, normalized for differing stress ratios [61]. Of interest to this work is the as built condition, Edwards and Ramulu presented the lower bound set of data for cycles to failure, significantly lower than conventionally cast Ti-6AL-4V, for various build directions and surface conditions [5]. Broadly this was attributed to a relatively large defect volume fraction [5], [61]. Both Xu et al. and Liu et al. report cycles to failure that outperformed reference data for post treated cast Ti-6AL-4V, with improved microstructure being the driving factor [61]. Leuders et al. reported a high monotonic tensile strength and significantly lower fatigue strength in comparison to cast Ti-6AL-

4V [53]. Wang et al. concludes a set of results with a mean fatigue life slightly higher than that of forged Ti-6Al-4V [60]. Van Hooreweder et al. studied near full density SLM AM Ti-6AL-4V and concluded fracture toughness and fatigue crack growth properties similar to that of conventional manufacturing methods [54]. Although there is conflicting comparison for cycles to failure the common theme is that the crack initiation phase and short crack growth behavior provides a lot of the variation and is predominately impacted by material defects such as porosity.

The porosity in AM Ti-6Al-4V comes in three distinct forms, typically these are referred to as trapped gas, LOF and keyhole porosity. Trapped gas induced porosity stems from an initial powder contamination, this gas contamination remains in the material as the melt pool solidifies rapidly resulting in voids/pores [4]. LOF induced porosity is mainly attributed to the lack of melt pool overlap or low energy, this results in un-melted powder which insulates and lowers cooling rates causing surface tension driven voids/pores [50]. Keyhole porosity can be formed at high energy densities which can instigate evaporation of the metal and the formation of plasma [52]. This results in a vapor cavity often deeper into the material than LOF defects, incomplete cavity collapse leaves a trail of relatively deep (to build layer surface) voids/pores [52].

The initiation of the different types of pores are linked back to the processing parameters and process window proposed by Gong et al., in Zone II (over melting / keyhole) the porosity is characterized by being spherical in nature and in Zone III (incomplete melting / LOF) the pores are irregular, elongated and sharp. Low energy density, insufficient reheating of the previous layer and a too fast scan speed are all related conclusions drawn by authors who have confirmed the presence of these irregular pores in Zone III [4], [51], [55], [62]. Morgan et al. discovered that a rough surface can also cause excess gas entrapment between build layers which in turn causes porosity as the trapped gas is heated by subsequent laser pass [63]. Figure 2.6 is from Kasperovich et al.'s study into the correlation of porosity and process parameters of SLM AM Ti-6Al-4V, (a) represents the irregular pores with a low energy density and (c) shows the spherical pores from over melting [55].

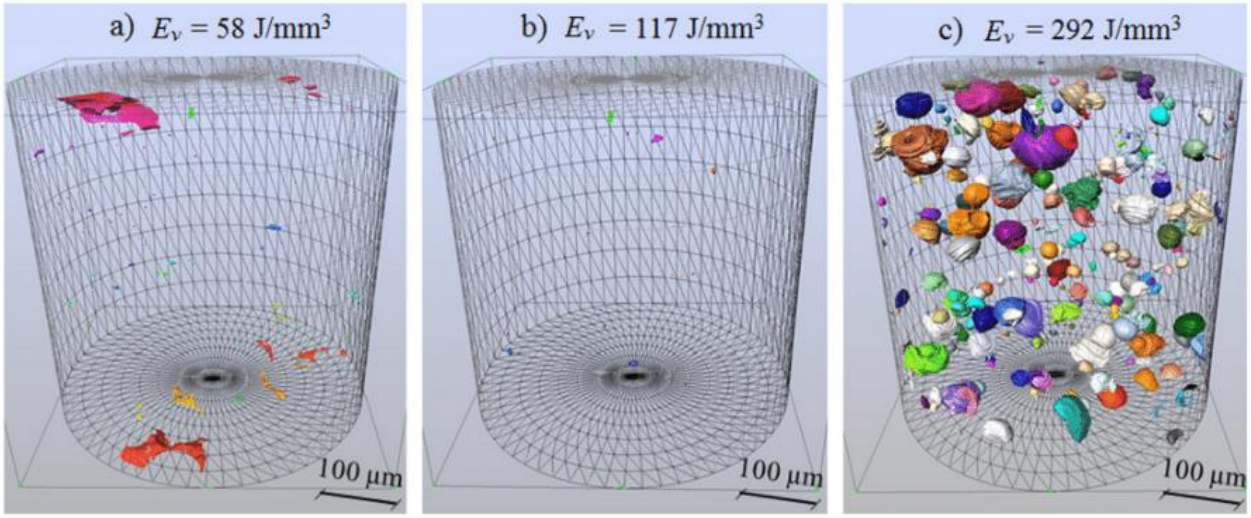

Figure 2.6. Various energy densities and their corresponding pore characteristics of spherical and irregular, for additive manufactured Ti-6Al-4V [55].

The irregular pores have also been shown to relate to the build direction. As they are a primarily a LOF defect present as a discontinuity in the intra-layer, the elongated length is parallel to the boundary and perpendicular to the build direction [49]. The anisotropic variance in ductility for different build directions can be explained by the elongated pores being pulled apart when loaded perpendicular to the elongated length [4]. In terms of fatigue Viet-duc le et al. observes that the critical pores related to the crack initiation are of the LOF defect type [41]. Researchers have also characterized these LOF defects as being separated surfaces with or without the presences of un-melted powder particles. Figure 2.7 shows scanning electron microscope (SEM) images adopted from Liu et al., taken from fractured compact tension samples of SLM AM Ti-6Al-4V, with an $E_v = 34.2\frac{J}{mm^3}$, showing LOF defects with and without powder particles present [64].

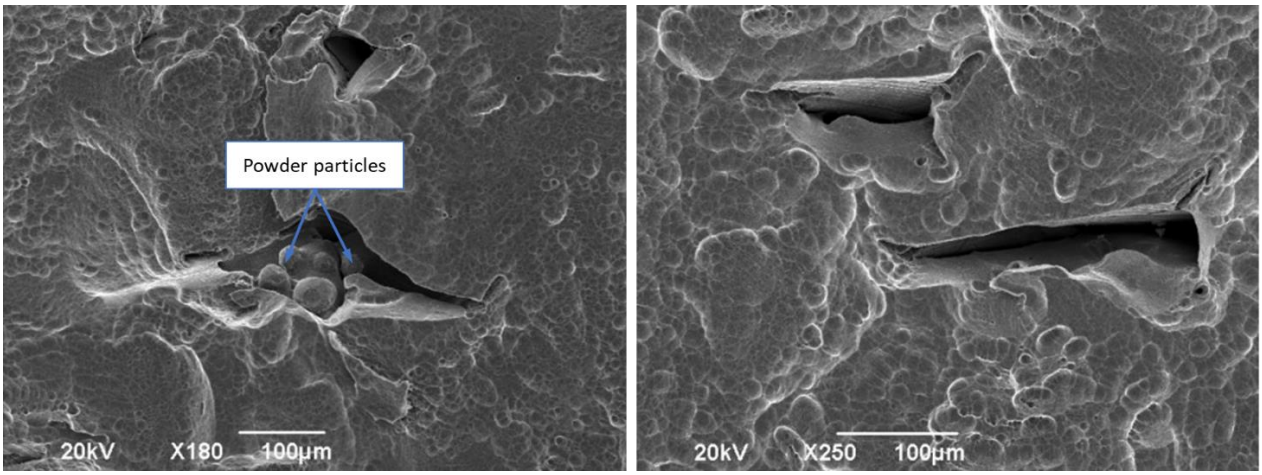

Figure 2.7. Example of LOF defects with or without un-melted powder particles in SLM AM Ti-6Al-4V adopted from Liu et al. [64]

Pore size, shape and volume fraction has been studied with respect to fatigue behavior in literature. Leuders et al. conducted the earliest and most extensive study into porosity, in summary a volume fraction of 0.23% was achieved and pore sizes from 22 – 50 μm studied (21 μm threshold due to tomography resolution), notably this study later removed all pores above 22 μm using HIP [2]. Kasperovich et al. obtained a volume fraction of 0.08% by optimizing process parameters and 0.01% using HIP [55]. Out of the 60 dog bone shaped samples of various build directions tested by Viet-duc le et al., fatigue cracks initiated from a single pore in 59 samples, 4 were in the bulk of the material the remainder classed as surface pores [41]. Pore size was considered and a relation to the fatigue strength was found for two of the three build direction tested [41]. Kasperovich et al. considers the sphericity measurement of pores in order to decide on the criticality for fatigue, any sphericity lower than 0.7 (1.0 being perfectly round) with a large aspect ratio could be considered critical if perpendicular to the fatigue loading [55]. With a large enough volume of these critical pores the effective loaded area is decreased and the sharp pores are then acting as stress concentrators, thereby lowering the fatigue properties.

The residual stresses that occur due to the SLM thermal process cycles have been shown to significantly influence the initiation and crack growth phase. The macro residual strain (Type I) across the SLM product exists of large tensile stresses at the top and bottom and varying gradient of compressive stress through the bulk [65]. In the work by Leuders et al. residual stress was

removed through the use of heat treatments and the results show a substantial influence on the fatigue properties, although this effect is coupled with the improvements to the microstructure [2]. As the literature review showed there is still a significant variation in the reported fatigue properties, a large factor is the cycles to initiation and short crack growth behaviors which have not yet been fully investigated.

2.2 X-ray Synchrotron Computed Micro-tomography

2.2.1 Background

Material characterization, in three dimensions, by high energy µXSCT has become relatively common place within material science literature. Useful data for a number of different applications has been reliably and rapidly obtained with the use of 2nd and 3rd generation (soon to be 4th) synchrotron high energy x-rays. The recent reported resolutions are as low as 100nm and proceed up to 10 μm depending on the material being tested and the synchrotron source experimental abilities [66]. This increase in resolution capability is largely due to the ability of recent advancements, that enable the thousands of images required to be taken at many images per second. Figure 2.8 shows the historical trends for tomography resolution and acquisition times for various facilities, as at 2014 [66].

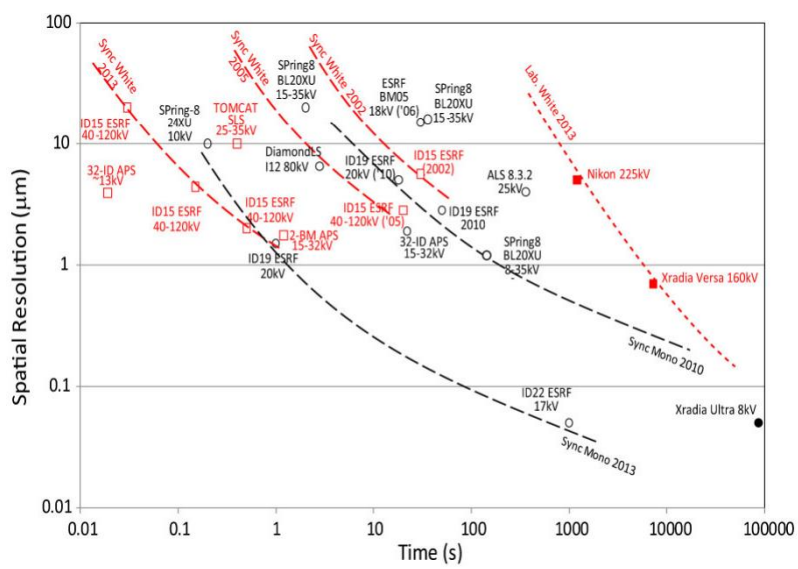

Figure 2.8. Showing established trends for resolution and acquisition times for µXSCT facilities[66].

One limitation of previous iterations of μXSCT facilities was the inability to acquire scans fast enough to allow for time sensitive experiments such as changes in stress or temperature, most experiments were done under quasi-static conditions. This has largely been solved and the 4th generation synchrotrons will enable very fast scans. It is also now possible to produce high resolution images of a particular area of interest well within a volume. Other than the attenuation or absorption imaging, new methods such x-ray diffraction microcopy, contrast based tomography and x-ray absorption at near edge structures amongst many others are continuing to improve and allow for greater applications.

2.2.2 μXSCT Measurement Principles

This review largely focuses on the use of absorption μXSCT systems and techniques as this was used within the following work. μXSCT is based on the attenuation of a transmitted beam as it passes through a sample, the basic setup requires an x-ray beam, sample and detector, Figure 2.9 [67] . The sample is imaged through angular rotations about an axis normal to the incoming beam, typically 180 or 360 degrees, at steps sizes usually of sub degree. These images are then a set of projections (called a tomogram) that can be reconstructed in order to view either a two or three dimensional output. The three dimensional output is created by stacking the two dimensional images (the space between being analogous to the scan resolution). Each three dimensional point in the tomogram is called a voxel.

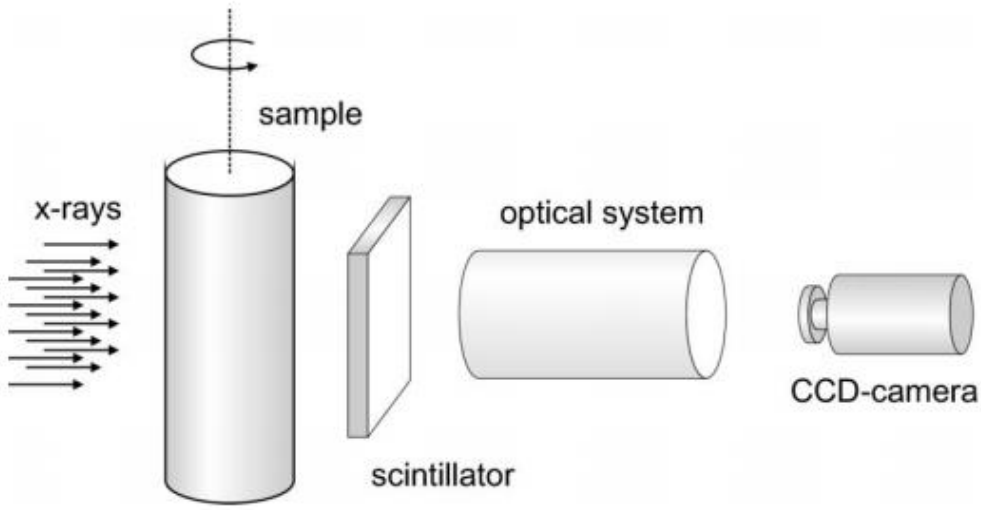

Figure 2.9. Basic μXSCT schematic [67].

The very high intensity of the hard beams used today are able to yield high signal to noise ratios at very short time intervals. Polychromatic and monochromatic beams can be used and the high parallelism of synchrotron source beams is used to limit imaging defects and the beam coherence is important for phase contrast imaging. In simpler terms when Elliot and Dover first discussed their x-ray micro-tomography (1980s) they described needed x-rays that are coming from a well-defined source, traveling in straight lines without scatter and obeying Beer's Law [68].

The fundamental principle of µXSCT is Beer's law of attenuation which is used to relate the attenuation of beam intensity to the beam energy, path length and material attenuation coefficient. Equations 2.2 and 2.3 show beers law for a monochromatic (and homogenous material) and polychromatic beam respectively, with I_o and I the initial and final beam intensity, μ is the materials linear attenuation coefficient and x the length of the x-ray path.

$$I = I_o \exp[-\mu x] \tag{2.2}$$

and

$$I = \int I_o(\mathrm{E}) \exp[\textstyle\sum_i(-\mu_i(E)x_i)]\, dE \tag{2.3}$$

Of note in Equation 2.3, is the attenuation coefficient being a function of the polychromatic beam energy (E), this requires solving the equation over the entire range of x-ray energies used. Beer's law accurately describes the sample attenuation, it is relatively simple to use in its linear form but can be difficult in the nonlinear polychromatic case, introducing beam hardening artifacts [69].

2.2.3 µXSCT Image Reconstructions

Considerable effort is required to be able to report quantitative results from the obtained two dimensional images, this image processing is typically the largest component of any tomography related experiment. The main step in all reconstructions is the use of a reconstruction algorithm, in most reviewed work this is by an algorithm based on the filtered back approach by Kak and Slaney [70]. A set of pre and post image processing steps are required to address the following image quality concerns (mostly artefacts), a number of these are covered within Section 5.

Many of the artefacts can impact the ability for researchers to report reliable data, for example ring artefacts and beam hardening (polychromatic beams) can lead to contrast issues that result in poor segmentation when using simplified thresholding tools. Many processing procedures are available but each material tested often requires its own set of input value.

2.2.4 µXSCT Measurement Applications and Results

A good example of the use of µXSCT is the work of Pyzalla et al. who used in-situ µXSCT combined with in-situ diffraction to look into the creep mechanism of deforming copper sample, tomography provides the pores analysis and diffraction provides crystallographic information [71]. Vagner et al. studied steel powders used additive manufacture as they were sintered, this required a very fast (less than 1 min) scan time [66]. A number of the reviewed studies in Section 2.1 used tomography based experiments, Kasperovich et al. used µXSCT to quantify porosity and Gong et al. used a similar approach [51], [55]. Leuders et al. used µXSCT, with a resolution that allowed for porosity greater than 22 μm to be examined (threshold of 21 μm and below related to tomography resolution) [2].

Overall as we see an increase in the availability of open source tools for tomography reconstruction improvements and quantifications there is likely to be even more use. The current limitations are the use of the filtered back approaches which do not suit noise data or too few projections and there is no easy way to measure the errors associated with the numerous steps required [66].

2.3 High Energy Dispersive Diffraction

2.3.1 Background

Strain characterization by energy dispersive x-ray diffraction (EDD) has grown more prevalent over recent decades with the advent and availability of 2nd and 3rd generation (soon to be 4th), synchrotron high energy x-rays. The high energy and collimation of polychromatic (white) beams has enabled penetration of samples in the order of tens of millimeters, small gauge volumes (often a few grains only), fast acquisition times and significantly improved accuracies [72]–[74]. Overall, recent research has proven the high spatial and strain resolution abilities of EDD, Figure 2.10 illustrates these capabilities in comparison to other methods [72].

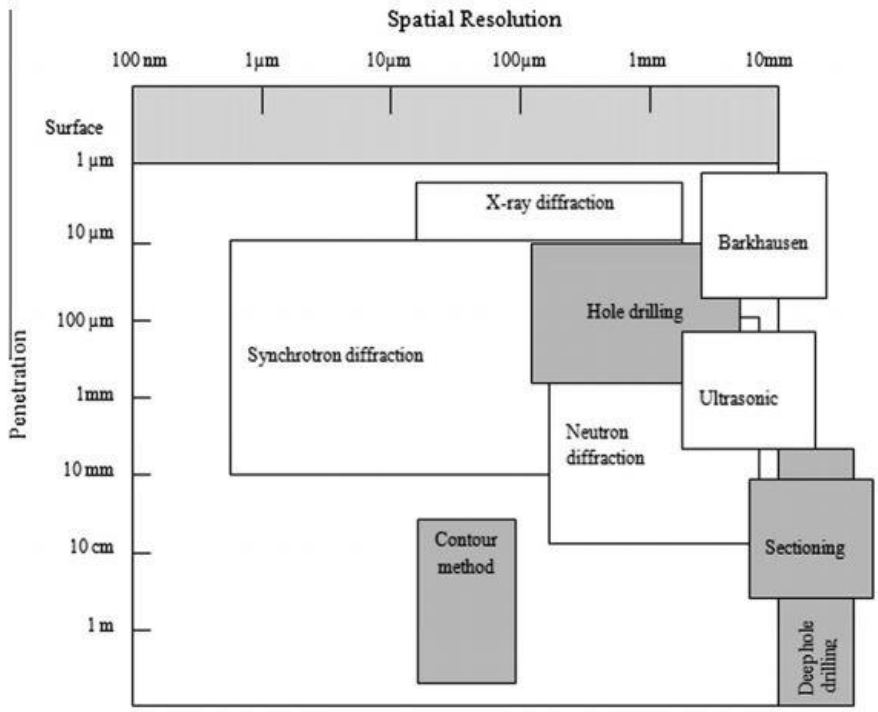

Figure 2.10. Resolution and penetration of various residual strain measuring techniques, as of 2012. Grey represents destructive methods [72].

Notably, fast acquisition times have proved useful for dynamic in-situ experiments previously deemed problematic. Most important, is the vast improvement in the ability to validate theoretical and computational models. This should lead to increases in the accuracy of service life predictions for engineering materials and components. The two main drawbacks of energy dispersive diffraction are related to the low scattering angle. These are the elongated gauge area resulting from spatial variations between the lateral and beam directions, and the difficulties in characterizing complex components.

Table 2.2 describes the different length scales that strains are typically characterized over, ε is the strain value and d_{grain} is the grain diameter [74].

Table 2.2. Strain classifications and associated characteristic lengths, adopted from Withers [74].

Strain classification	Characteristic length (a)	Characteristic length property
Type I	$\varepsilon > d_{grain}$	Macro residual strain that develops in the body of a component on a scale larger than the grain size of the material. Generally varying over large distances that represent a significant portion of the component.
Type II	$\varepsilon \approx d_{grain}$	Micro residual strains varying on the scale of each individual grain. Nearly always present in polycrystalline materials due to elastic and thermal properties of the different orientated grains.
Type III	$\varepsilon < d_{grain}$	Micro residual strains that exist within a grain, essentially as a result of the presence of dislocations and other crystalline defects, including coherency at interfaces.

2.3.2 EDD Strain Measurement Principles

Many components are manufactured from engineering materials consisting of tiny grains randomly oriented with respect to their crystalline structures. When subject to stress, elastic strain occurs within the crystalline structure of each grain. EDD can then measure this inter-atomic strain. EDD utilizes the relation between the lattice spacing d_{hkl} and the associated diffraction line E_{hkl}. This is derived using the energy relation and Bragg's equation given at Equations 2.4 and 2.5 respectively. The variables are h = Planck's Constant, v = wavelengths pre second, c = velocity of light, λ = wavelength of light and θ = the incident angle of light.

$$E = hv = \frac{hc}{\lambda} \tag{2.4}$$

$$d_{hkl} = (\frac{hc}{2sin\theta})(\frac{1}{E_{hkl}}) = const.(\frac{1}{E_{hkl}}) \tag{2.5}$$

The calculation of the lattice strain ε_{hkl} for a given orientation with respect to the sample becomes Equation 2.6. Noting, E_o and d_o represent the energy related to the stain free lattice spacing and the strain free lattice parameter respectively [75].

$$\varepsilon_{hkl} = \left(\frac{d_{hkl}}{d_{o\,(hkl)}}\right) - 1 = \left(\frac{E_{o\,(hkl)}}{E_{hkl}}\right) - 1 \tag{2.6}$$

Therefore, the strain is calculated from the change in lattice spacing with reference to the strain-free lattice parameter.

Because EDD is inherently selective, there is a focus on only a small subset of grains within a sample (gauge volume). The resulting peak shifts will give the strain average across the grains within the given gauge volume [72], [76]. Commonly the use of assumptions such as plain strain or other symmetry arguments are used to obtain the components of strain. For example, Ritwik et al. used these assumptions combined with independent measurements at different angular directions to calculate 5 components of the strain tensor [77].

2.3.3 EDD Strain Measurement Source, Setup and Techniques

The EDD synchrotron source can provide high energy monochromatic or polychromatic (white) beams, which are up to a million times more intense than conventional laboratory x-rays. The basic premise is the higher the energy of the beam, the lower the diffraction angle and greater the penetration. For a monochromatic beam source, at an average intensity of 50 keV, it is possible to achieve depths of 10 millimeters in aluminum down to 0.5 millimeters in iron or nickel [78]. This gave rise to the earlier premise of EDD only being useful for near-surface residual strain measurement.

In contrast, the polychromatic beam (up to 300 keV) provides a significant increase in total flux and penetration (tens of millimeters) [78]. Furthermore, a high-count efficiency is achieved due to the much larger bandwidth allowing for multiple simultaneous diffractions and a reduction in inefficiencies seen by monochromatic optics [78]. A monochromatic beam will provide a single diffraction peak, and polychromatic will provide numerous diffraction peaks across a spectrum.

Figure 2.11 is of the National Synchrotron Light Source, United States (NSLS), which is a typical schematic for a synchrotron source EDD experiment [79]. Main components are the slits, attenuator/s and filter/s which are used to collimate both the incident and diffracted beam and to remove low energy beam components. Also, of note are the solid-state detectors and the detector used to monitor transmitted beam intensity providing precise positioning of the gauge volume.

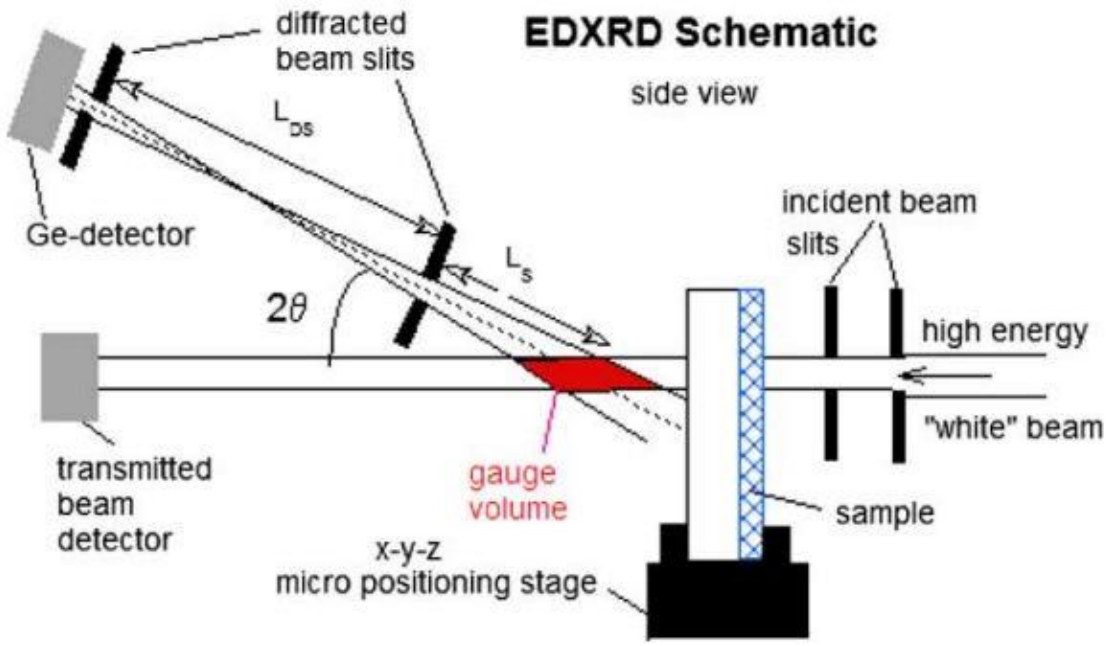

Figure 2.11. A typical schematic for a synchrotron source EDD experiment. (NSLS) [79].

A fundamental adjustable component of EDD is the slit system used to collimate the primary beam; these slits can have a significant impact on the definition of the gauge volume. Numerous slit systems are used depending on the different beam lines. The alignment of these slits along with the natural divergence of the beam is important for eliminating systematic errors in strain values [80]. Figure 2.12 represents recent improvements suggested in slit design, showing these can result in improved resolution, beam spot size, and shape. The use of a conical slit to prevent external reflection and a shielding system on the slit exit to suppress diffuse scattering improved hardening of the beam [80].

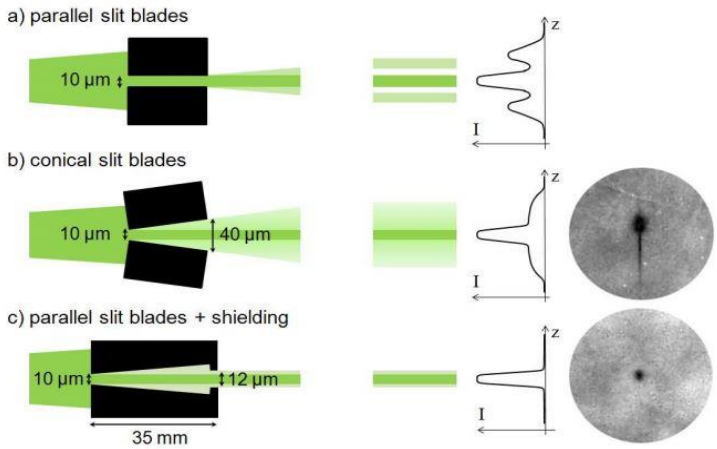

Figure 2.12. Slit configuration experiments are showing the effect on beam spot size and shape, intensity distributions and images of the scattered intensity behind the slit system [80].

Multiple detector systems are used, these are typically liquid cooled single crystal germanium detectors, although scanning by other perfect crystals is possible [81]. In a standard multiple detector system, the vertical and horizontal plane scattering vectors (q) are simultaneously detected, Figure 2.13 shows a schematic of this type of experimental setup, for EDD conducted at Advanced Photon Source (APS), United States.

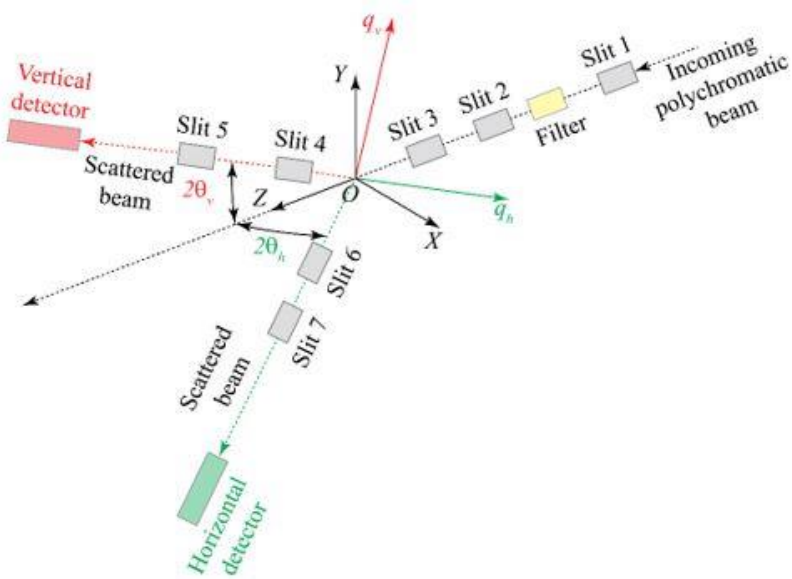

Figure 2.13. Schematic of an APS EDD experimental setup, showing beam direction, slits and detectors [77].

The complete technique sees a prepared sample fitted to a translation and rotation table which is capable of being scanned either across or along the beam (or both). The beam source is activated and the beam hardened via the slits, attenuators, and filters. Sample adjustments are typically conducted using a laser and a CCD camera. The choice of angle (2θ) is a function of the crystalline structure and the beam energy spectrum. The diffracted beam is collected by the multiple germanium detectors, and a multi-channel analyzer typically configured to output 2048 or 4096 channels. Diffraction pattern peak fitting via a number of methods, is used to obtain the lattice strains, finally, the strain tensor can be computed using the different sample angular measurements. Figure 2.14 shows a typical diffraction pattern obtained from a stainless-steel sample under a 5 MPa tensile load, the line fit uses the Rietveld method, the crosses are measured data, tick marks are predicted peaks and lower graph is the difference [82].

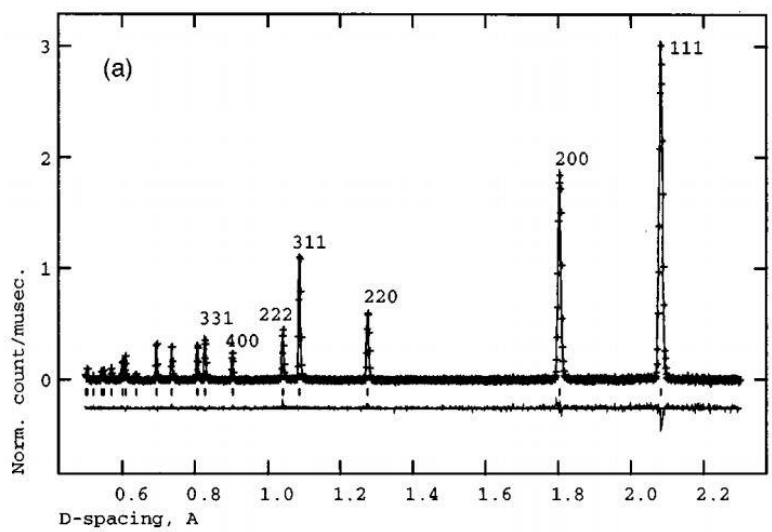

Figure 2.14. Diffraction spectrum from stainless steel under 5MPa load, crosses indicate measured data, line fit via a Rietveld method, ticks indicate expected peaks, and lower graph is the difference [82].

2.3.4 EDD Strain Measurement Applications and Results

Recent applications of EDD which are of particular interest are those that have proven the feasibility of both high spatial and high strain resolution or been used where other methods such as neutron diffraction are unsuitable. An example is the research into short crack growth

uncertainties which have continued to influence life predictions resulting in conservatism in the original design and in-service repair. To study this phenomenon a relatively thick sample is required (to negate near surface effects) and as the characteristic crack tip strain field length scale is tens or hundreds of micrometers neutron diffraction is unsuitable [73].

Using EDD crack tip strain fields have successfully been characterized in a number of fatigue cracked compact tension samples with similar EDD effectiveness [73], [79], [83], [84]. Representative of these is an EDD experiment on a 25 mm thick standard compact tension sample of austenitic steel, type 316H. The experiment was conducted at 300 keV with a diffraction angle of $3 - 3.5°$ (2θ), gauge volume of 400 by 400 μm and a 2 mm long pre-crack [73]. Figure 2.15 shows the geometry of the sample indicating the mapped area of 14 by 10 mm and the refined EDD diffraction spectrum with a Gaussian peak fit (deemed inappropriate by the difference curve in blue) [73].

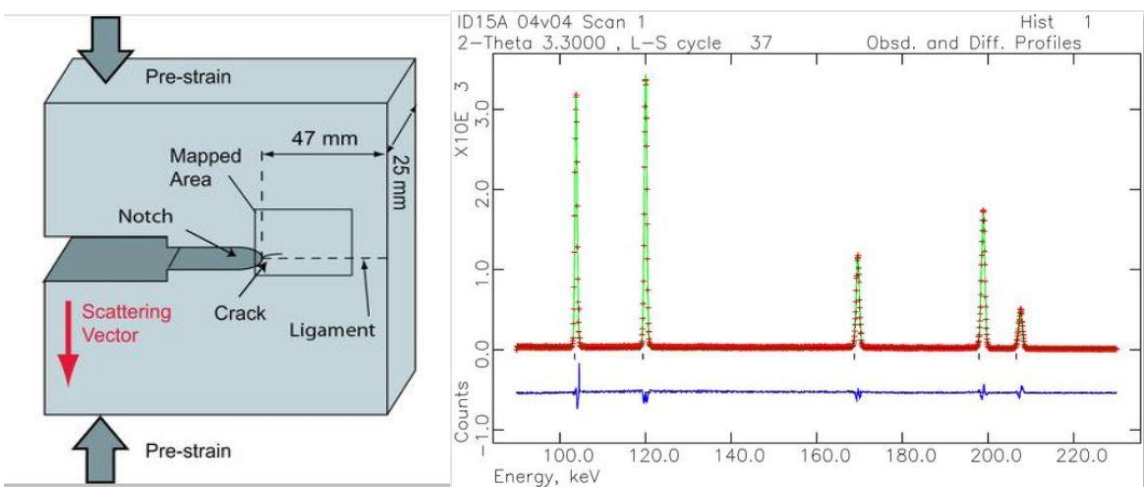

Figure 2.15. 316H austenitic steel compact tension sample geometry showing EDD mapped area and diffraction spectrum with inaccurate Gaussian peak fit [73].

Figure2.16 shows the elastic strain in the loading direction (ε_{22}) map (left) which correlated well with the predicted finite element analysis. Also shown is a comparison of strain results through mid-thickness, (right) indicating that neutron diffraction (black triangles) was unable to resolve the steep strain gradient near the notch. Steuwer et al. (and others reviewed) demonstrated that

synchrotron EDD can accurately characterize residual strain in thick components with spatial resolution of 20 μm and accuracy of ~10^{-5} [73].

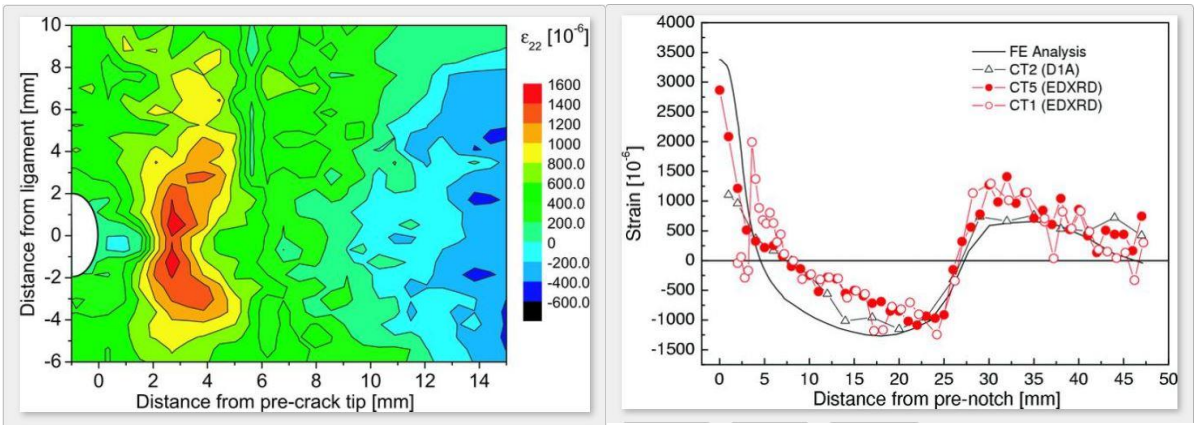

Figure 2.16. 316H austenitic steel compact tension EDD elastic strain (ε_{22}) map and strain measurement comparison for EDD, neutron diffraction and FEA [73].

Another area of research for residual strain measurement is Titanium linear-friction welds, which are utilized in jet aero-engines for the cost-effective joining of turbine blades to disks. The localized heating, microstructural difference and poor thermal conductivity of titanium results in high residual stress within the heat affected zone (HAZ) [85]. Although researchers have used neutron diffraction for strain measurement, the poor scattering properties of titanium have limited the success. Neutron diffraction studies state, penetration of ~5 mm and gauge volumes of ~1.5 by 1.5 mm [86]. Figure 2.17 shows a comparison of EDD (left) and neutron diffraction (right) for two separate Titanium linear-friction weld studies [85], [86]. The disparity in resolution and capabilities of the methods is clearly evident. The EDD was performed at 60-300 keV, the diffraction angle of 5° (2θ) and a gauge height of 200 μm (50 μm was possible).

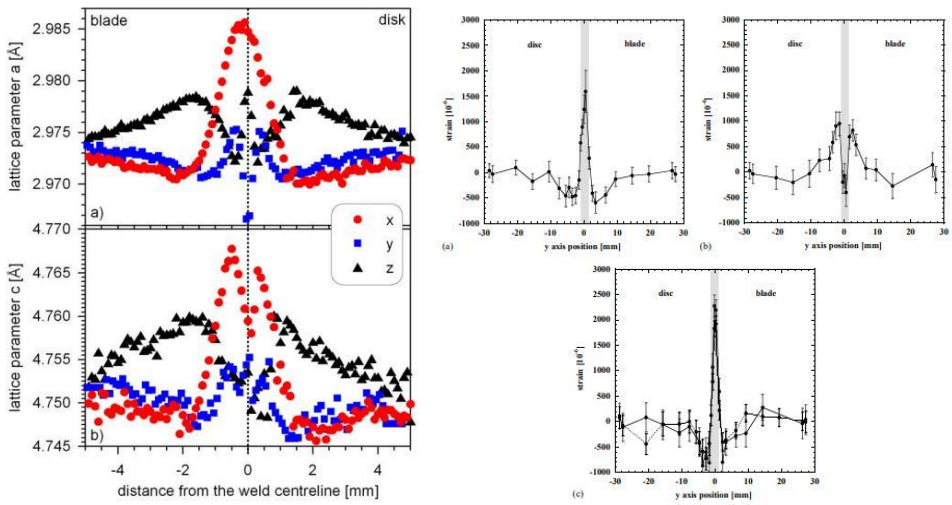

Figure 2.17. Comparison of typical Titanium linear-friction weld residual strain measurements, EDD (left) and Neutron Diffraction (right) [85], [86].

Many researchers highlight the highly efficient fast strain mapping abilities of the 2nd and 3rd generation synchrotron sources as the greatest benefit of EDD. For example, acquisition times reported for 3 mm Al, Ti, Fe and Cu alloys samples were ~30 s per 0.3 mm^3 (accuracy of < 10^{-4}) [78]. 50 mm depths of aluminum have been probed with a 20 μm gauge volume at <1 s acquisition times [76]. A recent paper (2012) on the monitoring of phase transformation stated that neutron diffraction was too slow to be effective [72]. EDD however, at resolutions of 1-100 μm and acquisitions time of 1 ms was proven to acquire data [72]. Finally, dynamic in-situ experiments at high temperatures are generally difficult to characterize due to the complicated setups and limited timescales available to acquire data. Examples that have successfully used EDD are the rapid thermal processing of $CuInS_2$ (solar cell production) and residual stress growth in CrN/Fe structures; both benefited from reported acquisition times of 10 s or less [75].

2.4 Previous Work

2.4.1 Background

The sample material investigated during this thesis had previously been used in a study into the effect of build condition and direction on long fatigue crack growth of SLM AM Ti-6Al-4V [64]. Motivation for this work was the lack of data on long fatigue crack growth for SLM AM Ti-6Al-4V. The variation of mechanical properties and crack growth property data was obtained from

Compact Tension (CT) samples with various build conditions and notch to build direction configurations.

Constant amplitude loading, with a stress ratio of 0.1 and cycling rate of 10 Hz was used in order to conduct the crack growth tests. The two build directions and notch positions tested are the horizontal and vertical builds as represented in Figure 2.18 [64].

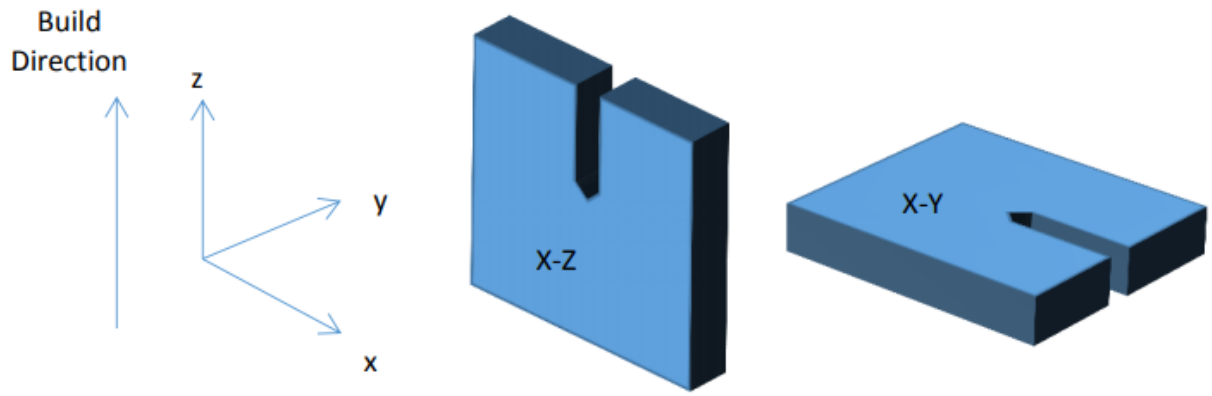

Figure 2.18 Compact tension specimens and build directions. X-Z: Vertical Build and X-Y: Horizontal build [64].

The focus of the research in the study by Liu et al. was on long FCG and the creation of the stress intensity range, ΔK verse crack growth per cycle, $\frac{da}{dN}$ data plots. The experiments closely followed ASTM FCG testing standards and allow for the comparison of the long FCG data to other AM and conventionally manufactured Ti-6Al-4V. In contrast this current work is solely focused on short FCG, specifically looking at behavior of the crack tip with respect to the inherent SLM defects. This study is considered complimentary to the previous work and potentially confirms the conclusions drawn by Lui et al. in regards to the variability seen and reasons therefore.

2.4.2 Results

The crack opening displacement and load were recorded during the cyclic loading and the linear portion of the displacement was used to obtain the crack length [64]. Eight CT samples were tested in total, and for the same build condition the horizontal crack growth rates were more consistent, vertical samples exhibited significant scatter. Figure 2.19 shows the results for three horizontal

and two vertical samples from the same build condition, sample naming convention includes B1 for build condition one, H for horizontal and V for vertical build directions.

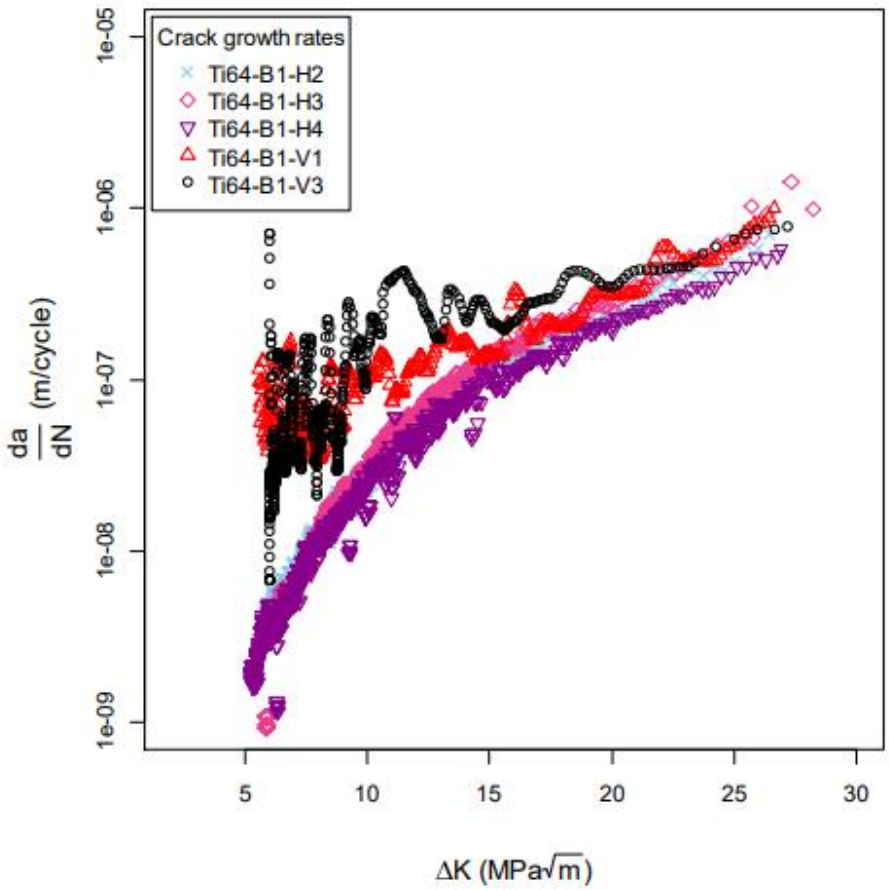

Figure 2.19. Long FCG rates for vertical and horizontal build SLM AM Ti-6Al-4V CT specimens of the same build condition [64].

The conclusions drawn by the authors suggest the scatter in the vertical samples is possibly due to a high number of defects, porosity and lack of fusion (LOF), within the material. Furthermore, as the crack is required to propagate progressively through the build layers the interlayers have considerably more defects and hence a rapid acceleration in growth [64].

3. SAMPLE MATERIAL AND PRE-CRACKING

3.1 Material Properties and Sample Details

The material of interest is Ti-6Al-4V additively manufactured by the SLM manufacturing method. The powder was manufactured by TLS Technik GmbH & Co in Germany, formed through gas atomization and conforms with ASTM Grade 23 [64]. The percentage weight of each alloying element is included in Table 3.1, the powder particles ranged from 25-45μm in diameter.

Table 3.1. Chemical composition of Ti-6Al-4V powder used in SLM applications, manufactured by TLS Technik GmbH & Co in Germany [64].

Powder: ASTM Grade 23, ELI (wt%)	
Ti	Balance
O	0.1
N	0.0009
C	0.008
Fe	0.17
H	<0.002

*Size range: 25-45 micron

The production of the specimens was in a SLM Solutions GmbH, SLH 250HL system, as depicted in Figure3.1, with a build chamber of 250 x 250 x 250 mm^3 and a maximum laser power of 400W. The chamber was purged with argon resulting in an oxygen level of 100 ppm and the powder was preheated to 200 $°C$.

Figure 3.1. SLM Solutions GmbH, SLM 250HL system similar to the one used to manufacture Ti-6Al-4V samples used within this work [87].

As per the discussion within the literature review, the properties and hence quality of the specimens can be related to the energy density, E as a function of build parameters, Equation 3.1. For these samples there was no attempt at optimization of the laser power, P, scan speed, v, layer thickness, δ, or hatch distance, h, parameters. In general if the energy density is below a critical window for optimization we expect to see incomplete melting, LOF and porosity, above the critical window we have over melting and keyhole porosity [64]. For this study the material is in the as-built configuration with two build conditions, trial and optimized as described in Table 3.1.

Table 3.2. SLM build parameters used to manufacture Ti-6Al-4V samples, the difference in energy density is used to differentiate the build conditions as trial or optimized.

Building Condition	Sample Build Designation	Laser Power (W)	Scan Speed (mm/s)	Layer Thickness (µm)	Hatch Distance (mm)	Energy Density (J/mm^3)
Trial	B1	175	710	60	0.12	34.2
Optimized	B2	100	375	30	0.13	68.4

The only conclusion drawn from the different build conditions is that that the lower energy density was clearly below the optimized window which resulted in a significant number of defects (LOF and porosity). Therefore, the terms, trial and optimized are henceforth used as a qualitative reference to sample quality.

$$E_v = \frac{P}{v\delta h} \qquad \left(\frac{J}{mm^3}\right) \tag{3.1}$$

The original samples were manufactured as standard sized CT samples in line with relevant ASTM guidelines. The scanning pattern used for all samples was alternating between each layer, as per Figure 3.2.

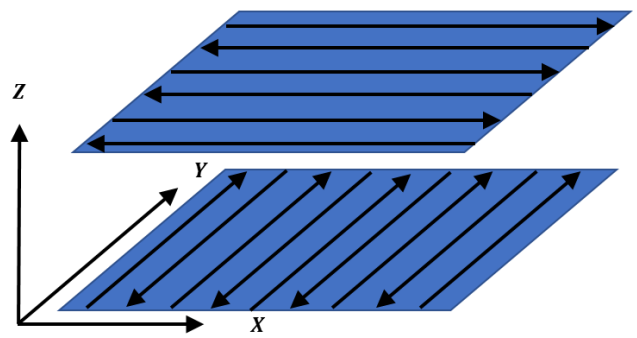

Figure 3.2. Scanning strategy used to manufacture Ti-6Al-4V samples is the alternating bi-directional with 90° rotation each layer.

The vertical and horizontal built CT samples with build directions illustrated were previously shown in Figure 2.18. Specimens for the current work were machined from the CT sample halves that had completely fractured during fatigue testing. ASTM E647 gives guidance for samples excised from bulk material for which complete stress relief is impractical. Specifically, limiting the sample dimensions and a careful location and orientation choice to minimize the effect of residual stress acting perpendicular to the crack growth direction [38]. The location chosen for the samples was as far away from the fracture surface as possible so as to be deemed unaffected by the propagating crack and associated plastic deformation. Figure 3.3 shows a schematic representation of the CT samples, build layers and approximate location chosen for machining samples.

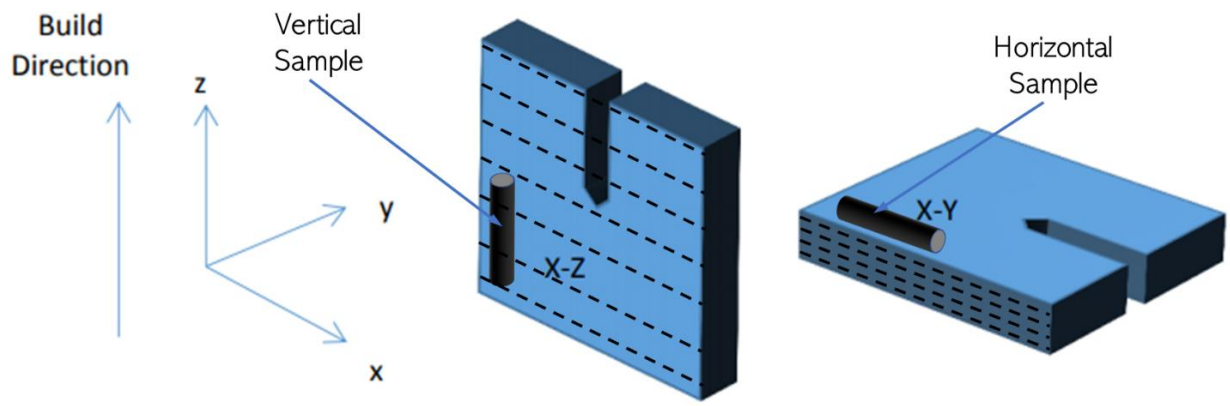

Figure 3.3. Schematic representation of the applicable locations and build directions for the vertical and horizontal samples.

In total six samples were manufactured from the fractured CT sample halves. Table 3.3 is a matrix showing the CT naming conventions, build conditions and characterization methods that were undertaken. The sample numbers 1 through 6 are henceforth used to designate the different samples throughout this thesis.

Table 3.3. Matrix showing the correlated sample number, specimen designation and original CT sample naming conventions, build condition and characterization methods employed.

Sample Number	Specimen Designation	Compact Tension Sample	Build Condition	µXSCT	EDD
1	CT5-60-V1	Ti64-B2-V1	Optimized	Tested	Tested
2	B1-H4	Ti64-B1-H4	Trial	Tested	Not tested
3	CT1-H3	Ti64-B1-H3	Trial	Tested	Not tested
4	CT3-V02	Ti64-B2-V2	Optimized	Not tested	Not tested
5	CT1-V1	Ti64-B1-V1	Trial	Not tested	Not tested
6	B1-V3	Ti64-B1-V3	Trial	Not tested	Not tested

3.2 Sample Geometry

The sample design was used in previous FCG studies within the ACME[2] laboratory at Purdue, the premise of the overall dimensions are to align them with ASTM requirements for small crack growth tests [38]. Figure 3.4 shows the sample dimensions, all in mm, including the gauge cross-section and corner notch position. The 1.5 x 1.5 mm gauge volume was small by necessity to ensure the x-ray tomography data could be obtained with a reasonable resolution. The samples were machined using conventional methods and the corner notch was completed using wire electrical discharge machining, as specified in ASTM E647 [38]. The ends of the sample, the grip section, were machined with a tight tolerance of 0.01 mm and a cylindrical shape to ensure an optimal fit within the collets used to hold the specimen when under cyclic loading.

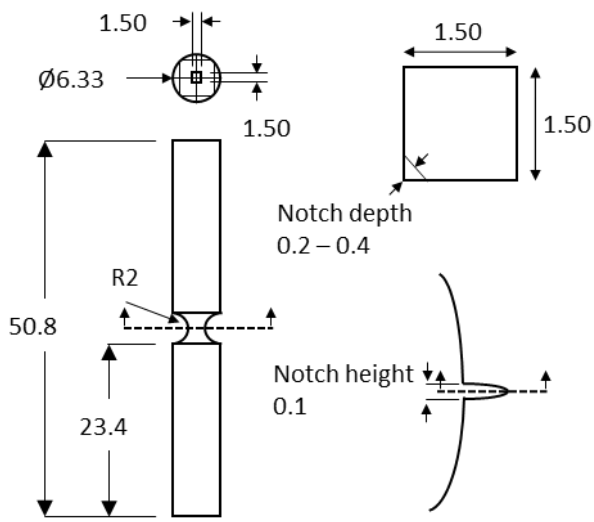

Figure 3.4. Diagram schematic of sample geometry in mm, gauge cross section and corner notch positon and dimensions.

The corner notch was chosen over a through thickness notch as the fan shaped crack would have a significant crack front width to crack length ratio, with the crack front being of particular interest in this study. A corner notch will also likely create an early crack front that exhibits significant tortuosity as the microstructure will be dominant over this length and area scale, any early crack path deflections will be evident in the high resolution tomography data.

The placement of the notch with relation to the build direction is of importance for any crack growth data analysis. Figure 3.5 shows that for the vertical build samples the notch and gauge volume placement will always have the crack growing parallel to the build layer. The horizontal build samples have an infinite number of crack growth direction to build layer orientations; two examples are depicted. As maintaining an account of the orientation of the cylindrical sample with respect to the original CT sample was difficult, porosity orientations and further characterization of the microstructure post fracture was used to gather evidence of the orientation.

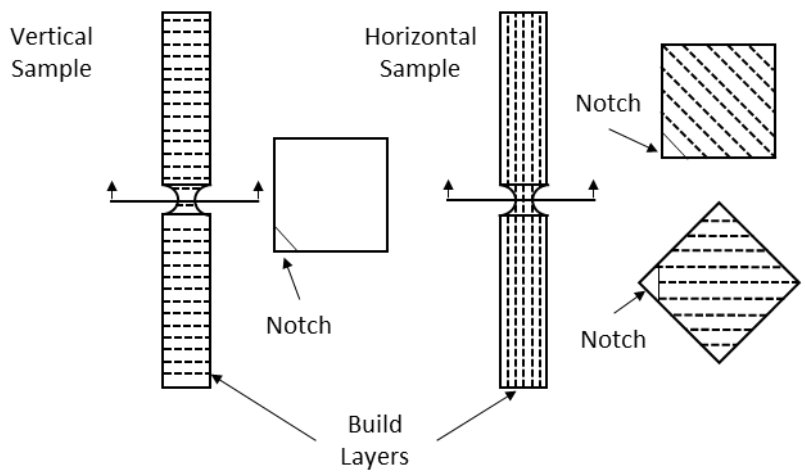

Figure 3.5. Diagram schematic of samples showing build layers, a vertical sample will always have crack propagation parallel to build layer, horizontal sample has infinite crack propagation direction to build layer orientations.

3.3 Elastic Notch Stress Concentration Factor

In order to determine the applied stress required for pre-cracking from standard Military Handbook stress-life data, an estimate of the elastic stress concentration factor, K_t is required. As the geometry for this the corner notch is complex, standard analytical methods are unable to accurately determine K_t [88]. Previous work by the AMCE^2 laboratory, on the same geometry samples, used AUTODESK Fusion 360^{TM} finite element analysis software to model the samples and provide an estimate for K_t [89].

Carter et al. used quadratic ten-node tetrahedral elements (3D elements), to account for the mixed mode stress state at the notch (plane strain or plane stress assumptions are invalid) [89]. Figure 3.6 shows the stressed mesh and the results indicated a K_t of approximately 3.0 at the notch root [89].

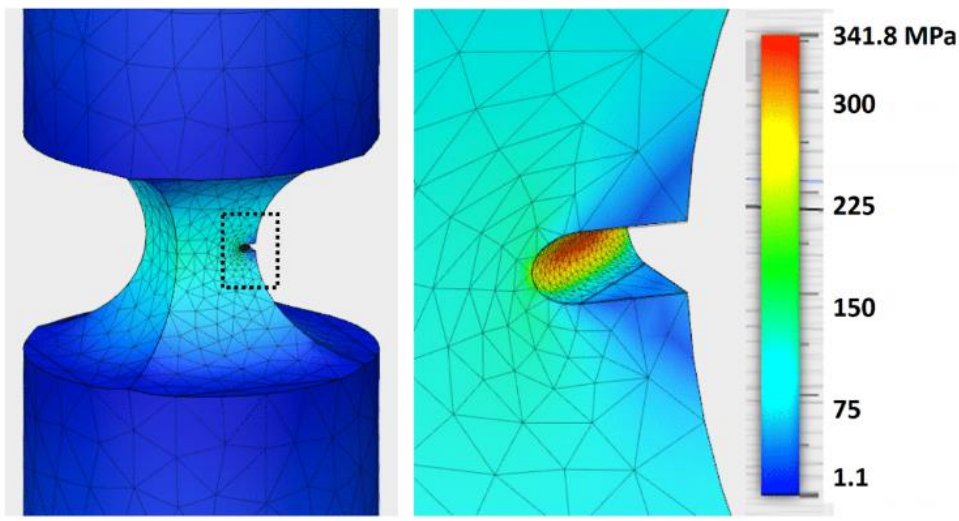

Figure 3.6. Finite element analysis, showing ten–node tetrahedral elements, stressed mesh and local notch yield stress [89].

3.4 Pre-cracking

Similar to the sample geometry considerations, the pre-cracking method took into account the ASTM standards for small crack growth tests [38]. ASTM E647 gives small crack fatigue testing guidance for the use of corner notches for crack initiation with respect to the R ratio, Equation 3.2, applied stress, crack measurement, crack symmetry, off axis loading and plastic zone effects [38]. Initial consideration was for the R ratio used, as the use of any compression component of the loading regime was difficult with the given small gauge volume. The pre-cracked samples were also to be fitted to a small load frame for in-situ loading experiments which utilizes a gripping mechanism unable to take such load regimes. Consequently, a tension-tension test using a R ratio of 0.05 was deemed sufficient.

$$R = \frac{\sigma_{min}}{\sigma_{max}} \tag{3.2}$$

In prior studies and also mentioned within ASTM guidance, a typical approach for tomography characterization of small cracks is to initiate a crack within a larger sample then machine out a small gauge volume that includes the crack tip [38], [89]. This approach can result in significant crack tip plastic zones as the load reduction techniques employed, start at a higher applied stress in order to initiate a crack within a reasonable cycle count. Other studies have used compression-compression testing to mitigate the plastic zone, this method can impact the fracture surface and is difficult to control due to the gripping mechanism chosen [90]. As the end use of the pre-cracked samples is to conduct in-situ fatigue crack growth the simplest approach is to choose a constant applied stress that will initiate a crack within a reasonable cycle count, have a limited plastic zone, and produce a crack growth rate that is sufficient for the limited beam time available for tomography scans.

First estimations for the applied stress comes from the ASTM small crack guidance section with the suggested use of 0.6 times the material yield strength, σ_{ys}. As an estimate, Leuders et al. and Kasperovich et al. give a yield stress for AM Ti-6Al-4V in the range of 950-1000 MPa, meaning an applied stress range of 570-600 MPa [6]. This is high when considering the small gauge volume, expected variability and trial nature of the build conditions. To further estimate an applied stress the calculated elastic stress concentrator, K_t of 3.0 can be used with Military Handbook stress-life data. Figure 3.7, shows the closest data fit available, predicting a life of around $10^5 - 10^6$, results in 55 Ksi or 379 MPa [91]. Taking into account the cross sectional area and subtracting the notch, the applied force for the net cross sectional area for all pre-cracking was 825 N.

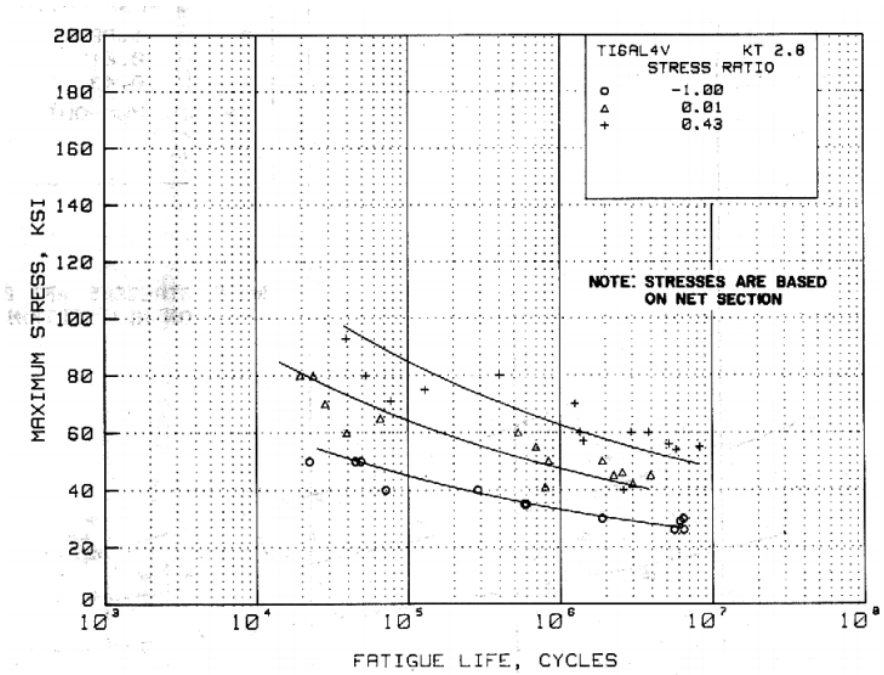

Figure 3.7. Extract from the Military Handbook (MIL-HDBK-5J), showing S/N curves for annealed room temperature extruded Ti-6AL-4V, with K_t = 2.8, used as an initial estimate for pre-cracking load [91].

All pre-cracking was conducted via force control, on a hydraulic MTS™ fatigue testing apparatus. A Manta Allied digital camera fitted with a Mitutoyo 10x or 20x lenses was used to inspect the notch area for evidence of cracking. Figure 3.8 shows the fatigue test apparatus and an 20x image captured from the digital camera depicting a crack initiating from the notch root. Previous work on similar specimen geometries had used specially designed steel adaptors along with ER-11 collets to hold the samples and mount to wedge type MTS grips. Axial and rotation alignment was difficult, so the use of v-type MTS grips was selected for this work. The benefits of these grips is there is no requirement for the use of the ER-11 collets, there is an inherent axial self-aligning tendency and negligible rotational alignment concerns. Although the v-type grips were largely successful the comparative size of the sample to the fatigue testing apparatus still presents a challenge for off axis loading and symmetry of the crack. Some evidence of off axis bending forces was evident in the digital camera images, with the machining surface lines showing misalignment whilst under load. Figure 3.9 shows this misalignment in sample 6, at 50,000 cycles, crack length is approximately 200 μm and load was 825 N this sample was not characterized further within this work.

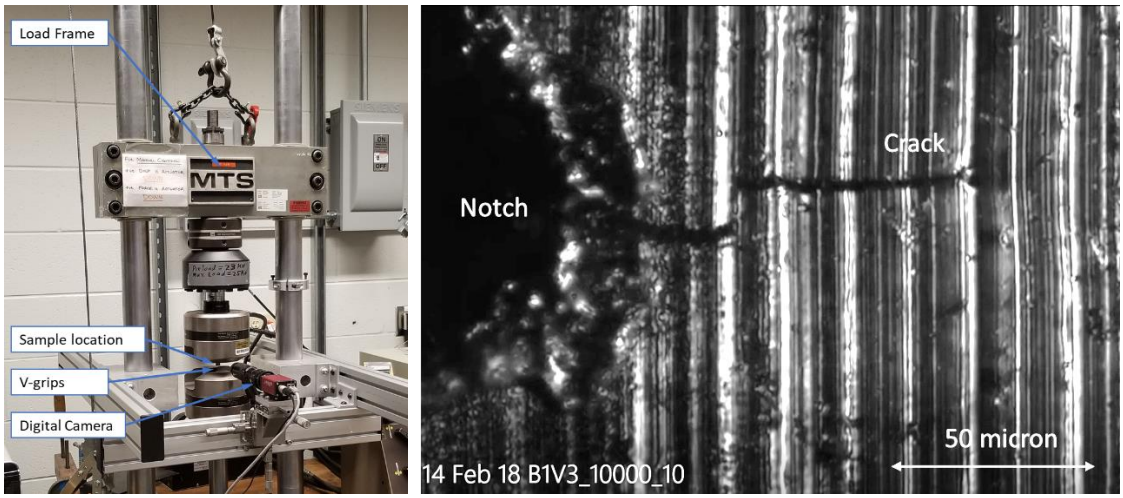

Figure 3.8. MTS fatigue test apparatus setup used for all pre-cracking, example of a 20x image showing a crack initiating from notch root on sample 6.

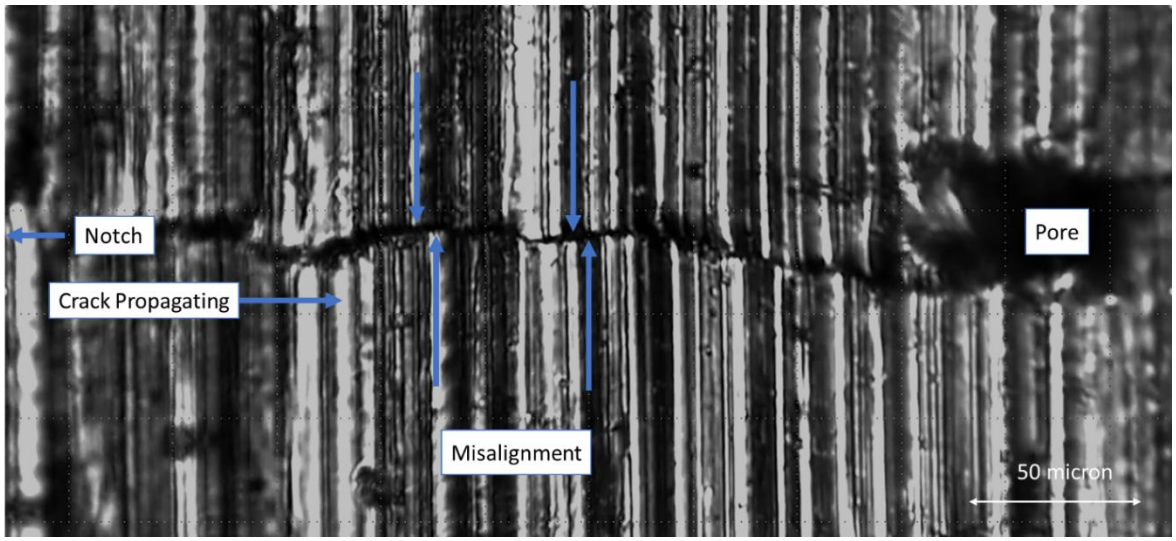

Figure 3.9. Indicates axial misalignment when mounting a sample in to the MTS fatigue test apparatus. Sample 6, at 50,000 cycles, crack length is approximately 200 μm and load was 825 N for this image.

As the Military Handbook estimate of applied stress and life was only a guide, blocks of 5-10,000 cycles were conducted at 3Hz, before a reduction of frequency to 0.5Hz, for 100 cycles in order to inspect for crack initiation via the digital camera. Cracks tended to initiate at the base of the notch root closest to one of the two corner surfaces, as this could occur on either side of the notch the

sample had to be rotated to visually inspect as the camera was fixed in location. Figure 3.10. shows 20x image of a very early, visually recognizable crack initiation at the notch root of sample 4. These images indicate the difficulty in confirming the presence of a crack, the images correspond to unloaded 50 N (left) and loaded 825 N (right).

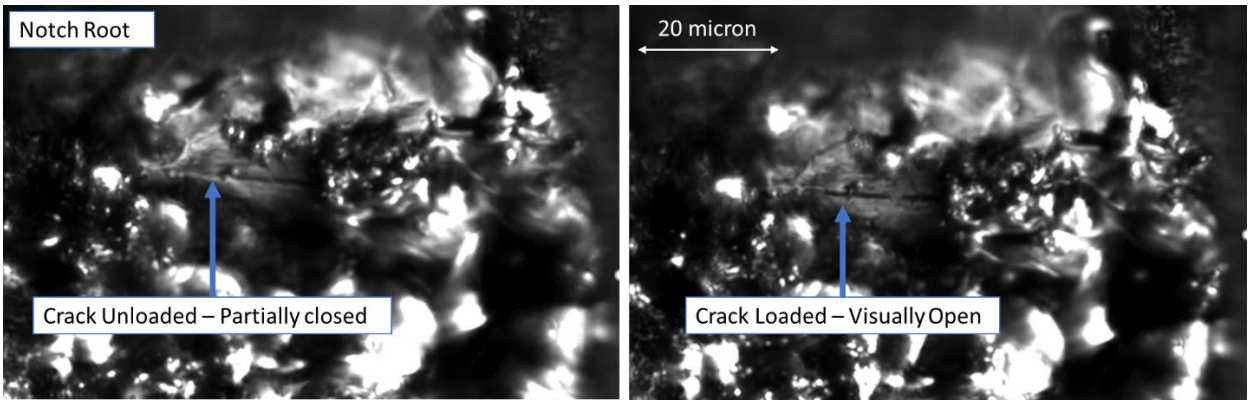

Figure 3.10. Notch root of sample 4 at 58,000 cycles, unloaded 50 N (left) and loaded 850 N (right) showing confirmation of a crack.

Once a crack was visually evident with confidence, it was grown until visible on both faces of the sample adjacent to the notch. The approach was to grow the crack until it had propagated to an average length of 150 to 200 μm on each side of the notch. Table 3.4 contains all of the fatigue cycle testing data for the six samples, pre-crack cycles are for a crack of 150-200 μm.

Table 3.4. Non-cumulative fatigue cycle data, per sample, for pre-cracking, in-situ μXSCT, in-situ EDD and fracture as applicable.

Sample Name	Experiment	Max Load Cycles (N)	Cycles	Hz	R
1	Pre-crack	825	100,000	3	0.05
	2-BM Tomo	800-830	20,550	1	0.05
	6-BM EDD	800-830	4,000	0.5	0.05
	Fracture	825	23,719	3	0.05
		Total	148,269		
2	Pre-crack	825	78,000	3	0.05
	2-BM Tomo	800-830	32,600	1	0.05
	Fracture	825	12,948	3	0.05
		Total	123,548		
3	Pre-crack	825	73,000	3	0.05
	2-BM Tomo	800-830	30,150	1	0.05
	Fracture	825	37,283	3	0.05
		Total	140,433		
4	Pre-crack	825	67,000	3	0.05
		Total	67,000		
5	Fracture	825	24,200	3	0.05
		Total	24,200		
6	Pre-crack	825	50,000	3	0.05
		Total	50,000		

A primary concern when conducting fatigue crack initiation on small samples is the ability to maintain the stress ratio, R and accurately hit the σ_{min} and σ_{max} values. This is whilst completing the required cycles within a reasonable timeframe and not inducing any temperature related effects. For all pre-cracking the frequency used was 3 Hz, with a cyclic periodic force which very accurately maintained the preset stress values. Figure 3.11 shows a representative example of this minimal variation over time obtained during the machine exploratory phase used to test the sensitivity to cycle frequency. The image shows cycling at 3 Hz, $\sigma_{min} = 50$, $\sigma_{max} = 780$ and $R = 0.06$.

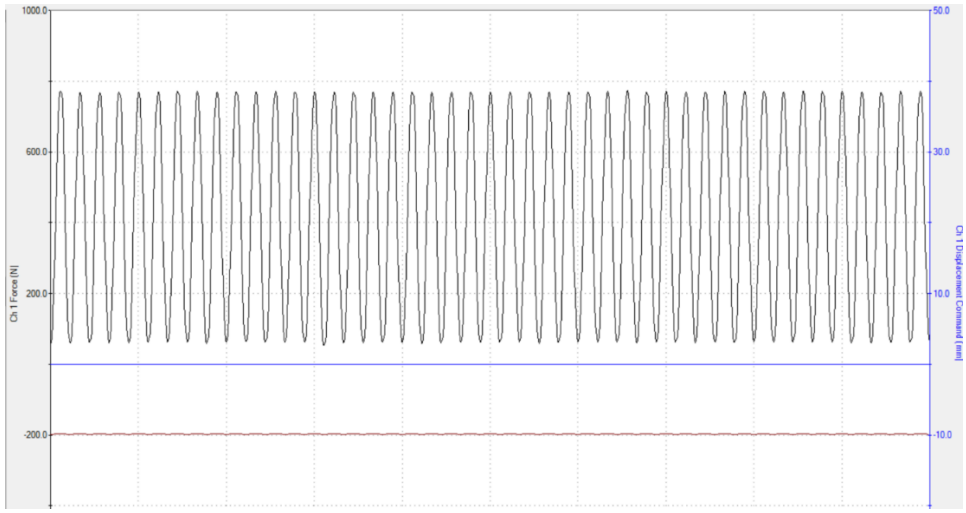

Figure 3.11. Data log printout of fatigue cycle testing, showing minimal variation in output variables at 3 Hz, $\sigma_{min} = 50$, $\sigma_{max} = 780$ and $R = 0.06$. Note, these value are close to the stress values tested in this work, data log taken during testing of machine capabilities.

4. X-RAY SYNCHROTRON COMPUTED MICRO-TOMOGRAPGHY EXPERIMENTAL METHOD

4.1 Background and Overview

In-situ crack growth experiments were conducted at the Argonne National Laboratory, Advanced Photon Source (APS), beamline 2-BM between June 11th and 15th, 2018. Tomography scans with intervals of cyclic loading were carried out on samples 1, 2 and 3, for a total of 79 separate scans comprising approximately 0.5 TB of raw data. Each sample was cycled and scanned repeatedly until the crack had propagated a sufficient amount for the purpose of this study, approximately 200-400 μm. FCG data for all three samples was successfully collected, within the timeframe allotted and without any major issues.

4.2 In-situ Loading

In order to conduct in-situ loading experiments the ACME[2] laboratory has built a portable load frame capable of being fitted to the rotational stages used at APS beamlines. The load frame uses a displacement controlled high tolerance screw-drive motor to apply an axial load. The motor to frame connection is via a machined, slotted plate which allows for a very accurate axial alignment of samples. Figure 4.1 shows the portable load frame mounted to the 2-BM stage and a close up view of the sample mounting mechanism and load cell.

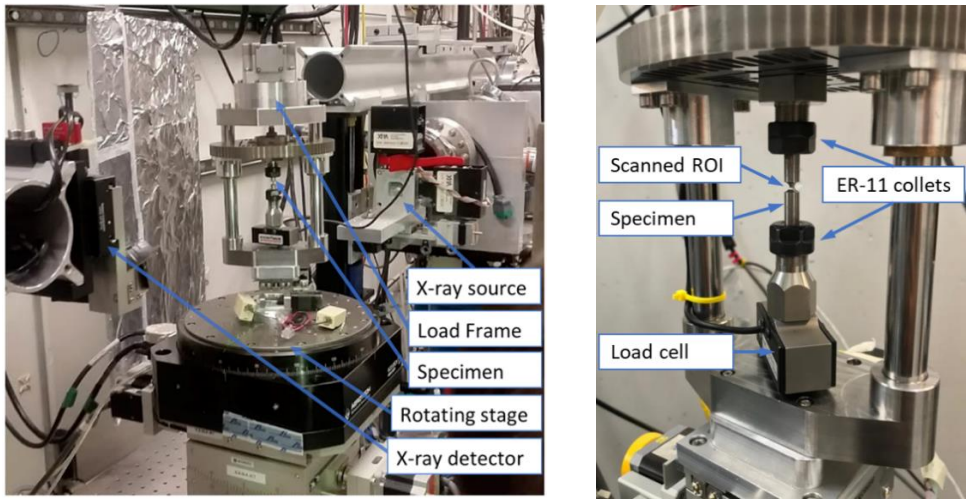

Figure 4.1. Experimental setup used for tomography at 2-BM, APS.

The ER-11 model collets use a conical shaped sleeve which is tightened against the sample by the hexagonal nut and threaded receiver which provides a clamping force. The load applied to the sample is measured via the SML-1000-16 load cell transducer which provides a voltage through to an amplifier. Prior experimental work has calibrated this voltage, in mV to its corresponding applied load, P (N), Equation 4.1 represents this relationship [89]. This voltage can be read by the APS native control systems to provide a real time applied stress value, this is captured in the file name for each scan whilst under constant load and manually recorded for all cyclic loading applications.

$$P(N) = 1.626(mV) + 93.228 \tag{4.1}$$

In order to control the load frame motor displacement, the proprietary Copley Motion Explorer 2 V7.0 (CME2) control software (manufacturer of the screw drive load frame motor) is used in conjunction with an amplifier and USB interface to a generic laptop [92]. A basic Python script is used alongside the CME2 software to cyclically drive the screw motor, using a triangular periodic form. At a frequency of 1 Hz the system was able to maintain a high level of stress value repeatability, any further frequency increases caused instability in the σ_{min} and σ_{max} values.

4.3 Sample Mounting

The installation of samples was a tedious task with the very real risk of applying a torsional load or excessive axial load great enough to either plastically deform or fracture the small gauge volume. By using a tightening procedure that first tightened the freely rotating end (load cell end) followed by carefully tightening the fixed end (motor end) the torsional load risk was mitigated. As the fixed end collet is tightened a progressive axial load is applied to the sample, monitoring this load and compensating by manually driving the screw motor meant the maximum load applied was minimal.

The collet grip design is prone to slippage whilst under high axial loads, previous experiments with this load frame have had difficulties in maintaining the frictional force required. Fortunately, the tight manufacturing tolerance for the grip section was strictly adhered to and with the use of a cleaning process and diamond paste to improve the frictional force, little issues were encountered.

Other than some minimal initial stress relaxation seen during tomography scans the applied load remained steady throughout, samples were subject to full load prior to commencement of scans.

4.4 Beam Settings

The beam line scientists calibrated the beam parameters to suit the material and volume to be scanned. By using the real time radiograph the notch and pre-crack locations are noted, the region of interest is fixed using these locations and the scan macro adjusted accordingly. The 1.5 x 1.5 mm gauge volume with a height of 1 mm was scanned using an x-ray energy of 24.9 keV. X-ray radiographs were obtained using a 200 millisecond exposure time per scan and the sample was rotated through 360 degrees with a velocity of 0.5 degrees per second. The sample was located 9 cms from the detector resulting in a resolution obtained of 1.3 μm. Taking into account the ability to distinguish between two separate pixels via Nyquist sampling, the smallest feature that can be resolved must be 2.6 μm or larger in size.

4.5 In-situ Fatigue Crack Growth Experimental Procedure

With the region of interest and beam parameters calibrated an initial tomography scan was taken to ensure the output was useful and capturing the required data. By using the native APS TomoPy code a non-optimized reconstruction was performed which enabled an accurate estimate of the crack length obtained from pre-cracking [93]. Although these reconstructions were 'rough', the runtime of a few minutes meant they provided the ability to check on crack propagation progress, between each cycle block in real time.

For each of the three tested samples, after the first tomography scan the sample was cycled for 50-100 cycles. Afterwards, a tomography scan was performed, this small number of cycles was in order to check for any abnormally large crack growth which would indicate an issue with the testing procedure or material. The cycling was progressively increased to 1000 cycles at 1 Hz with an approximate run time of 20 minutes, each tomography scan took approximately 15 minutes. Table 3.4 contains the total cycles completed for each sample during the tomography experiment, further detail for each cyclic block is provided at Appendix A.

For each block of cycling the motor position was recorded by taking the counts (equates to motor rotation) away from a fixed zero position, this fixed the motor position for the σ_{min} and σ_{max} values. As the cycling is displacement controlled any relaxation in the sample, or extra displacement due to the crack opening was adjusted for between each block by editing the Python script used, driving the motor (counts) further. These changes were confirmed with a single load to 825 N prior to each cycle block, in this way the σ_{max} values were maintained in the range of 800-830 N, and stress ratio maintained at $R = 0.05$ on average, Appendix xx contains the relevant details.

The constant load for the tomography scans was recorded, and the range was similar to the cyclic loading, 800-830 N. As the estimates for the crack length were recorded between each cycle loading, if the crack was deemed to have not grown, the cycles were increased to 2000 or even 4000 cycles. Sample 2 and 3 exhibited much lower crack propagation rates and as such the cycle blocks were on average larger for these samples. This process was repeated until sufficient crack growth was seen, consideration for the limited beam time available was also taken into account.

5. X-RAY SYNCHROTRON COMPUTED MICRO-TOMOGRAPGHY RECONSTRUCTIONS

5.1 Background and Overview

One of the largest tasks undertaken was the optimization of the reconstruction methods used for the 79 individual tomography scans obtained. The primary goal was to enable visualization of the crack surface evolution and any material defects such as LOF or porosity, as three dimensional volumes. The process is iterative and requires a systematic approach in order to optimize the pre and post processing, thresholding and visualization. The reconstruction output is a stack of 32-bit greyscale intensity images of 2560 x 2560 pixels with the resolution per the tomography scans, of 1.3 μm. The stacked images are also spaced 1.3 μm apart so the voxel size is 1.3 x 1.3 x 1.3 μm^3 for the three dimensional renderings.

5.2 TomoPy Reconstructions

TomoPy is a parallelizable high performance reconstruction code created by APS beamline scientists. The code provides a way to automate a number of image corrections and reconstruction methods in order cope with the increase in data acquisition capabilities at synchrotron sources [93]. The code is completely open source and largely written in Python, with some C++ and C components. Figure 5.1 is an overview of the process steps TomoPy is capable of performing, most with some level of automation [93]. The process starts with raw x-ray radiographs (import data), then corrects these radiographs, reconstructs into a sliced volume and performs image corrections on these reconstructions. Various input parameters are able to be configured by the user, with a number of these interrelated. In the case of this research some process steps were conducted using TomoPy and others with methods discussed further in this section.

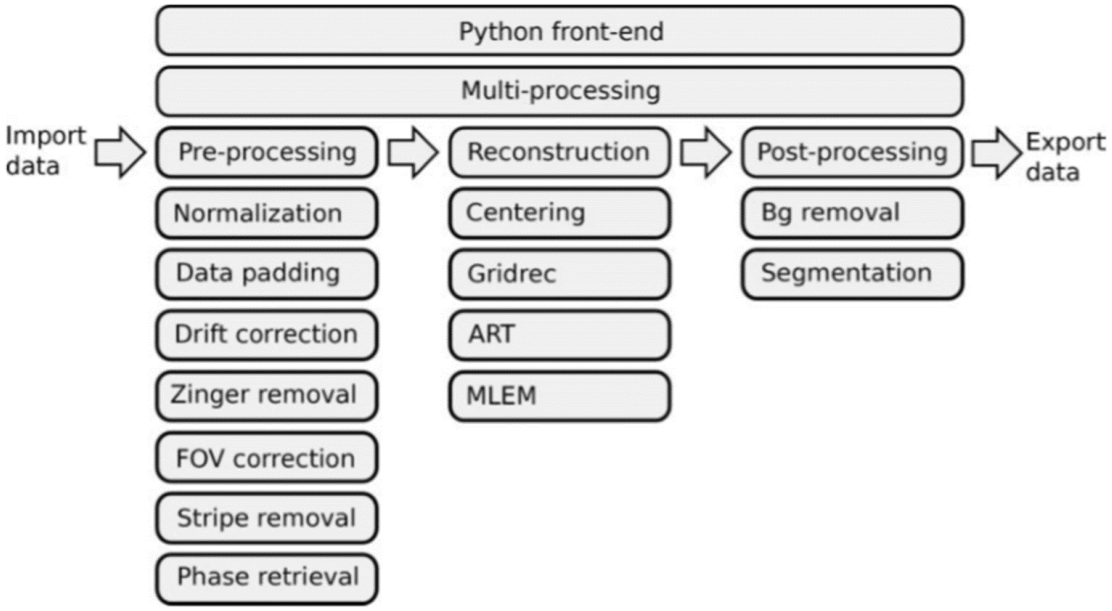

Figure 5.1. Overview of the TomoPy process steps available for reconstruction and correction of images from raw synchrotron radiographs [93]

5.3 Pre-processing

In terms of normalization, the standard method of using the white images (taken with the beam only, in the absence of the sample) and dark images (taken without the beam) to correct the raw data intensities was used. As with most datasets this basic subtraction normalization does not correct for the other reconstruction artifacts caused by x-ray beam drift or imperfections within the detector systems. Of particular concern for this dataset was the zinger and stripe removal, zingers are outlier pixels and stripes are the horizontal stripes present in radiographs due to the rotating sample with a fixed beam and detector. Figure 5.2 shows a slice from the image domain (reconstructed domain) with and without these removal tools. As the conservation of image features was the priority a series of iterations resulted in the combined use of the Wavelet-Fourier filtering and Titarenko's approach, parameters used are contained in Table 5.1 [94], [95] .

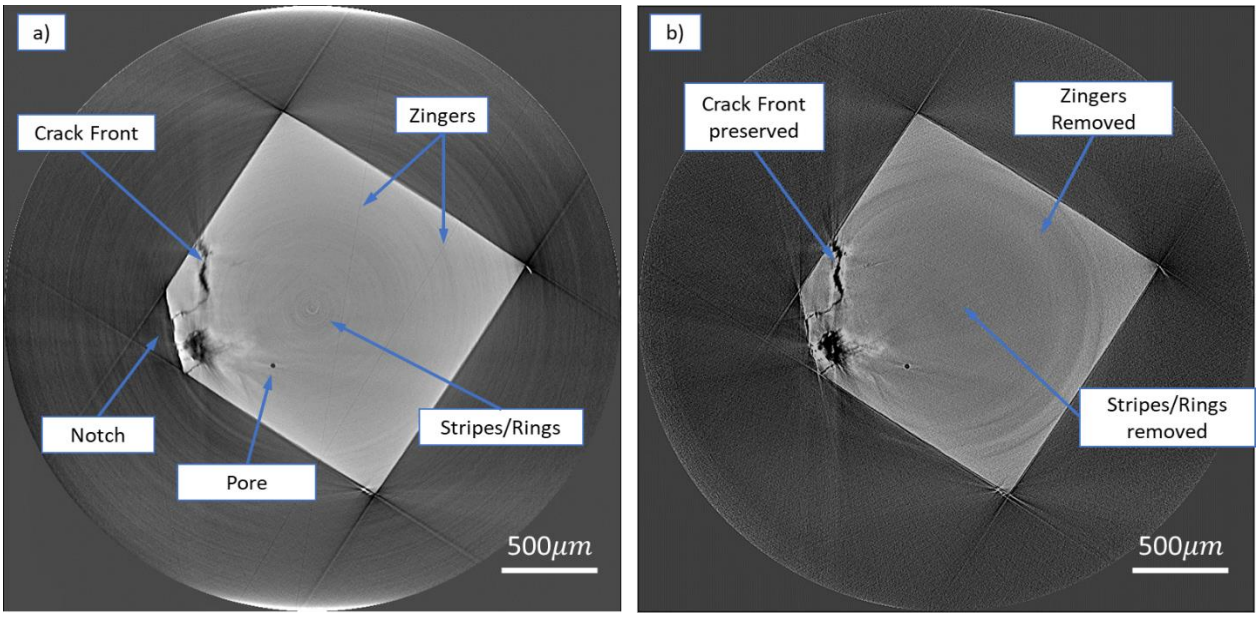

Figure 5.2. Reconstructed slice (image domain) from sample 1, with notch and crack front evident. Slice without the use of TomoPy tools to remove zingers and stripes/rings (a), and slice showing results after removal (b).

5.4 Reconstruction

Of the inbuilt reconstruction methods, the Gridrec or Fourier grid reconstruction algorithm was employed. The raw data domain (radiographs) are mapped to the image domain using a method similar to the back-filtered approach described by Kak and Slaney [70], [95]. The major component of ensuring the reconstructions are correct is having good estimates for the geometrical parameters. The dominant parameter is the rotation center, which is also a function of the fixed beam and detector with rotating sample. Although TomoPy has a number of automated algorithms for the calculation of the rotation center, these were not possible for the obtained data set. A manual process of trial and error was used, a single slice was reconstructed with varying rotation centers until the image aligned and feature were sharp. Figure 5.3 shows a reconstructed slice with rotation center incorrect (a), and optimized (b), visually obvious errors are blurring, streaking and misalignment. Rotation center values used to reconstruct the complete dataset are recorded in Appendix A.

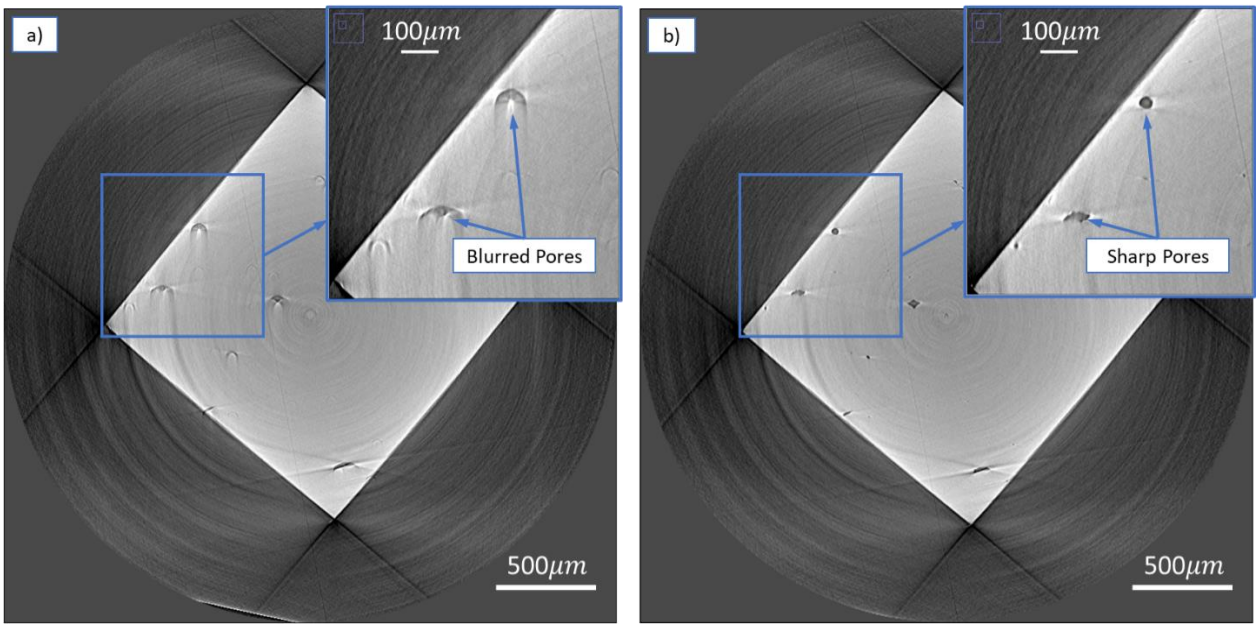

Figure 5.3. Rotation center parameter effects shown as incorrect with evidence of blurring, streaking and misalignment (a) and optimized (b).

As the load frame is rotated through the entire 360 degrees the supporting posts obstruct the x-ray beam for approximately 20 degrees of rotation twice. This obstruction results in dark images only for these scans, this was taken into account during the full reconstructions by adjustments made to the TomoPy script by the beamline scientist. Although largely successful the completed reconstructions required significant post processing due to persistent ring artifacts and the low contrast between crack surface, porosity and the bulk material.

5.5 Post Processing

The TomoPy ring removal tool was only marginally successful in completely removing the ring artifacts, issues with rings at the center and rings overlapping the propagating crack front, resulted in a significant loss of crack front and image features when thresholded. After trying numerous software iterations, a Matlab script was modified from the work of Jha et al. which overall provided much better results [96]. This Matlab script converts the reconstructed data back to polar coordinates, creating lines from rings and uses a similar wavelet-Fourier filtering to TomoPy but combines this with Lyckegaard's algorithm to remove the lines [96]. All 79 reconstructions had the ring removal performed using this adopted Matlab script in combination with TomoPy tools,

the sharpness and contrast remained high and the fracture surface was preserved. Figure 5.4 shows a comparison between the TomoPy native ring removal and the Jha et al. Matlab script; (a) is without any ring removal tools, (b) is via the TomoPy native tool, clearly visible are wide dark rings with a contrast similar to the crack front and (c) is the Matlab script resulting in a largely homogenous contrast throughout the bulk material.

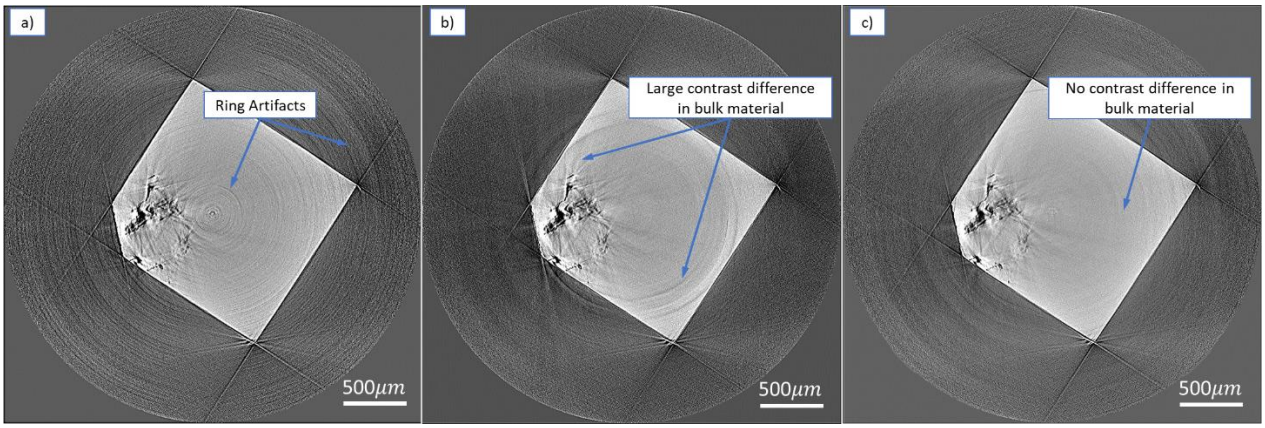

Figure 5.4. Different stages of ring artifact removal are shown, without any ring removal tools (a), Tomopy ring removal showing dark contrast artifacts remaining (b) and reasonably homogenous contrast obtained through the bulk via the Matlab script (c).

The other post processing software used was the open source ImageJ (Fiji plugin version) [97]. A number of filtering, smoothing, de-noising, fast Fourier transforms and even a machine learning segmentation tool (Weka Segmentation) were iteratively trialed over a period of months to ensure the completed reconstructions were capable of being thresholded.

5.6 Thresholding and Visualisation

In the case of the tomography scans the object of thresholding was to obtain the intensities that correspond to the fracture surface, crack front, pores and other material defects. Once obtained the crack evolution or bulk material defects can be studied with clarity, the software used was the previously mentioned ImageJ and also Avizo (version 9.1.1) [97], [98]. The object of the prior steps is to optimize the sharpness, contrast and the reduction of reconstruction artifacts. The success of these steps are not evident until the thresholding is completed with minimal loss in features, this highlights again the iterative nature of image processing. Figure 5.5 shows the

following images of samples 1, an SEM image taken post complete fracture (a) and an Avizo volume rendering of the fracture surface (b), a high correlation of features indicates successful thresholding.

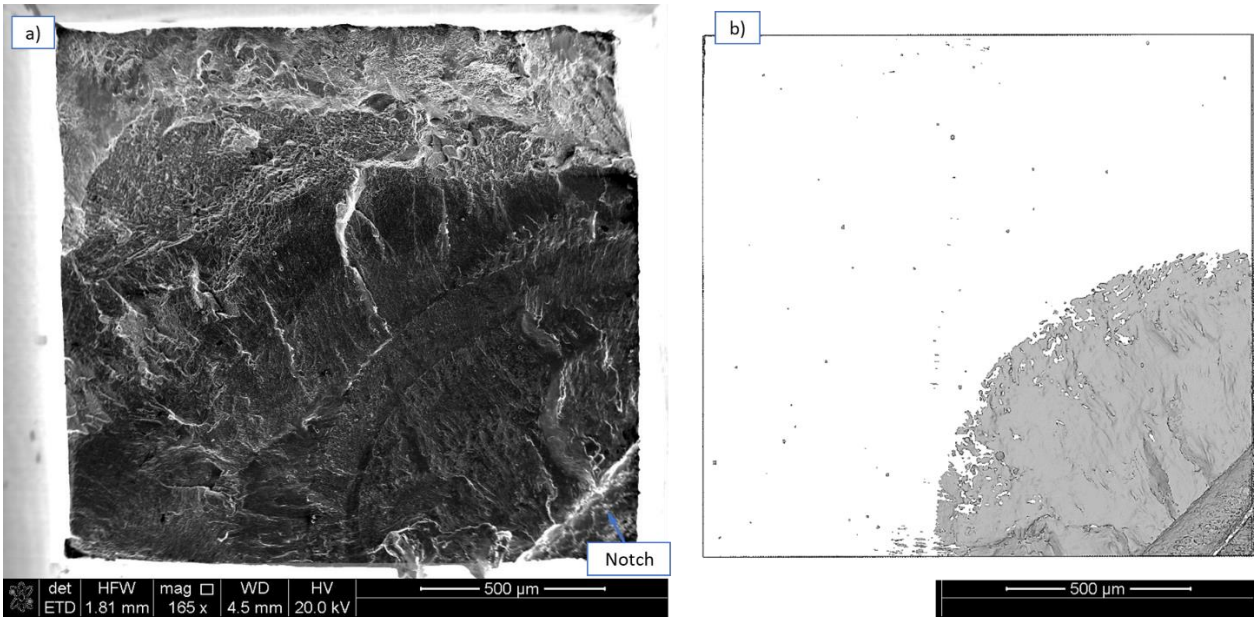

Figure 5.5. Sample 1 images showing a high correlation of fracture surface features for an SEM image, post complete fracture (a) and a reconstructed tomography scan, Avizo rendering (b).

As there are variations in the greyscale intensities for each sample and even within scans of the same sample the threshold values changed for each reconstruction. For the crack growth measurements, the thresholded fracture surface and crack front was compared between the two dimensional orthogonal views (ImageJ) and three dimensional volume renderings (Avizo) to ensure as close as possible to the entire crack was measured.

Table 5.1. List of parameters and the values as inputs for the TomoPy tools used for the reconstructions of raw tomography data.

TomoPy Tool	Use	Parameters	Explanation	Value used
remove_outlier	Zinger removal	dif	Expected difference value between outlier value and the median value	1300
		size	Size of the median filter used	15
		axis	Axis along which to chunk and use median filter	0
remove_ring	Ring artifacts removal	All	All parameters optional	Standard
median_filter	Median filter - smoothing	size	Size of the median filter used	3
normalize	Normalize raw projection data	flat	Normalize projections using white images (no sample)	3D flat field data
		dark	Normalize projections using dark images (no beam)	3D dark field data
remove_stripe_fw	Stripe removal (Fourier Wavelet)	level	Number of discrete wavelet transform levels	6
		wname	Type of the wavelet filter	db5
		sigma	Damping parameter in Fourier space	1
remove_stripe_ti	Stripe removal (Titarenko's)	nblock	Number of blocks	0
		alpha	Damping factor	5
retrieve_phase		pixel	Resolution	1.3
		dist	Sample to detector distance	9
		energy	Beam energy	2.9
		alpha	Balance sharpness and contrast	5.E-03
gridrec_recon	Fourier grid reconstruction algorithm	theta	Projection angles in radian	0.5
		center	Location of rotation axis	As per Appendix A
		algorithm	Reconstruct object from projection data	Gridrec
		filter_name	Filter for analytic reconstruction	No filter

6. FATIGUE CRACK GROWTH ANALYSIS AND RESULTS

6.1 Background and Overview

In Section 2, the literature review showed various researchers have reported conflicting data on the fatigue crack growth of AM Ti-6Al-4V, especially when defects are present. In order to measure the crack growth for the comparisons between samples 1, 2 and 3 a rigorous experimental technique was required. Whilst considering a suitable characteristic crack length, the tortuosity and morphology of the crack along with any significant crack deflections must be observed. Examining reasons for any crack deflections and defect interaction are also investigated. The results for this section are considered in line with previous work on CT samples and any relevant literature results.

The build directions and conditions are summarized again in Table 6.1, reiterating the three separate cases discussed within this section. Furthermore, for all three samples the notch to build layers are schematically shown in Figure 6.1, for sample 2 and 3 orientations are determined from the porosity defects, this is discussed in Section 7.4.

Table 6.1. Summary of the build direction and build condition for samples 1, 2 and 3.

Sample Number	CT Specimen Build Direction	Build Condition
1	Vertical	Optimized
2	Horizontal	Trial
3	Horizontal	Trial

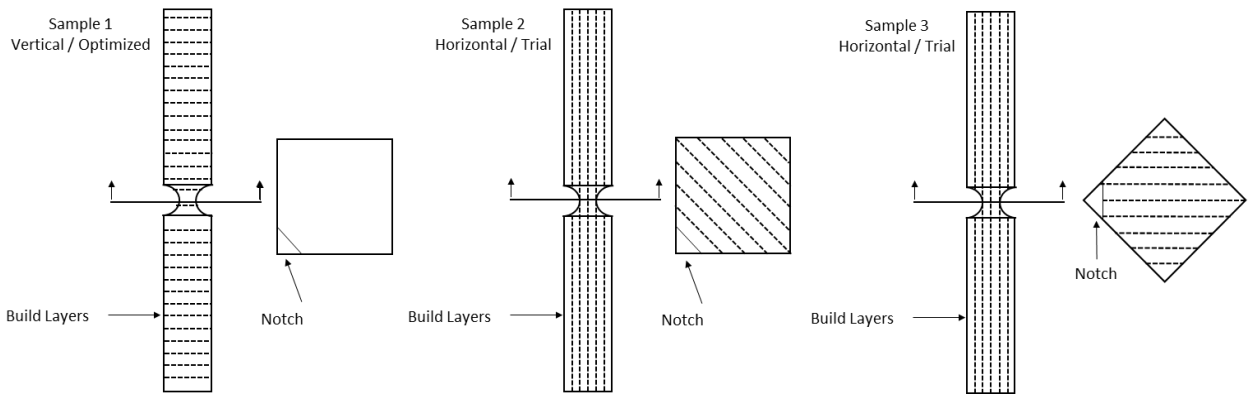

Figure 6.1. Summary of the notch to build layer orientations for samples 1, 2 and 3.

6.2 Measurement Methods

For each of the in-situ FCG experiments conducted as per Section 4 and reconstructed with methods described in Section 5, a series of tomography reconstructions were produced. Figure 6.2 shows an example of three dimensional renderings created using the Avizo software, sample 1 is shown at 120,550 cycles with a measured crack length of 632 μm.

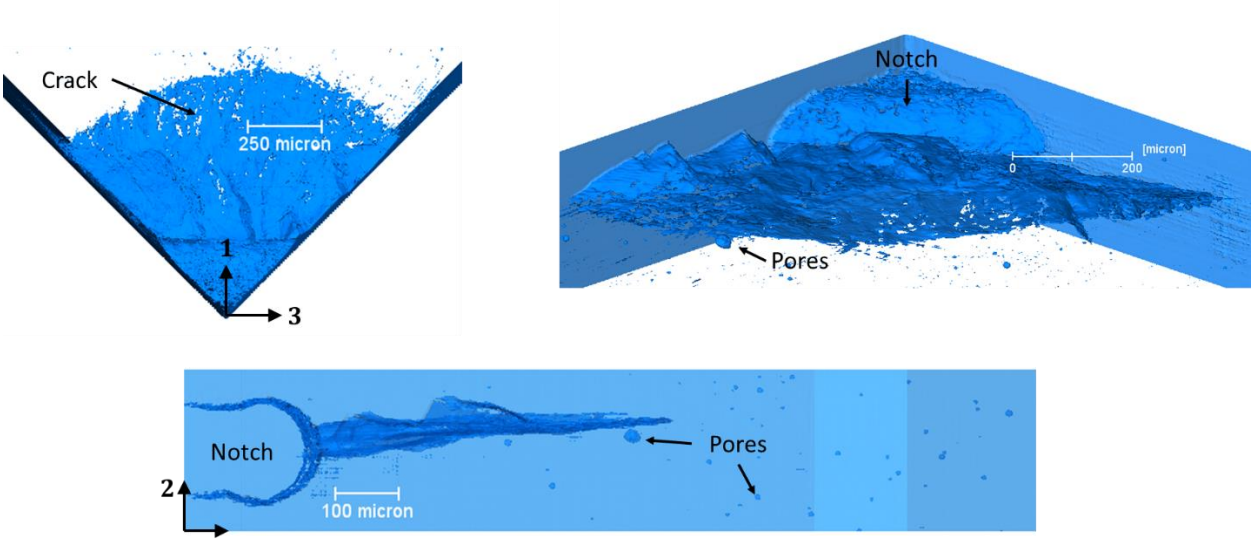

Figure 6.2. Example of Avizo three dimensional renderings of the FCG tomography reconstructions, sample 1 is shown at 120,550 cycles with a crack length of 632 μm.

The analysis and measurement of the FCG behavior was conducted using the measurements tools in Avizo and ImageJ. For every tomography scan taken three dimensional measurements using a snap to feature function was taken in Avizo and a two dimensional measurement taken on the

orthogonal views using ImageJ or Avizo. Both these measurements were taken on the largest length of the propagating crack, starting at the notch root and measuring perpendicular, if the error was minimal, as per Equation 6.1, the three dimensional length was taken (typically larger). Figure 6.3 depicts sample 1 with the two different techniques used to confirm FCG lengths, two dimensional orthogonal view measurement, (a), and the three dimensional Avizo measurement, (b). To note, the line measurements are in pixels and the resolution for these tomography scans was 1.3 μm, the result of this measurement pair was a 632 μm crack length at 120,550 cycles.

$$\frac{3D\ length - 2D\ length}{3D\ length} < \pm 5\% \tag{6.1}$$

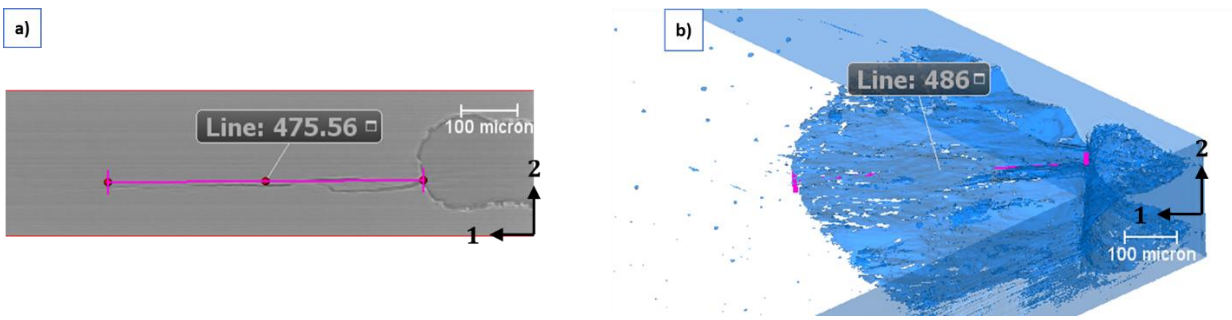

Figure 6.3. Example of the two measurement methods used to obtain the short FCG data, orthogonal measurement, (a), and three dimensional measurement, (b).

By using an arc drawn on the Avizo renderings the longest length was also confirmed where possible, this extra care was taken during the measuring process as the crack growth rates were minimal so any error would be deemed to affect the results significantly.

6.3 Crack Growth and Path Evolution

Crack growth evolution and the tortuosity and morphology of the crack is depicted for each sample in Figures 6.4, 6.5 and 6.6. Each set of figures show a series of tomography scans (a–d) for increasing cycle counts and a set of orthogonal views from relevant two dimensional sectional slices, as described by ‘aa’ and ‘bb’ sectioning planes. These two dimensional orthogonal slices are used to show the evolution (same slice shown each time) of the largest movements away from

the more dominant parallel crack path, they are not a projected view of the tomography volume, detailed three dimensional images are included in Section 6.5.1.

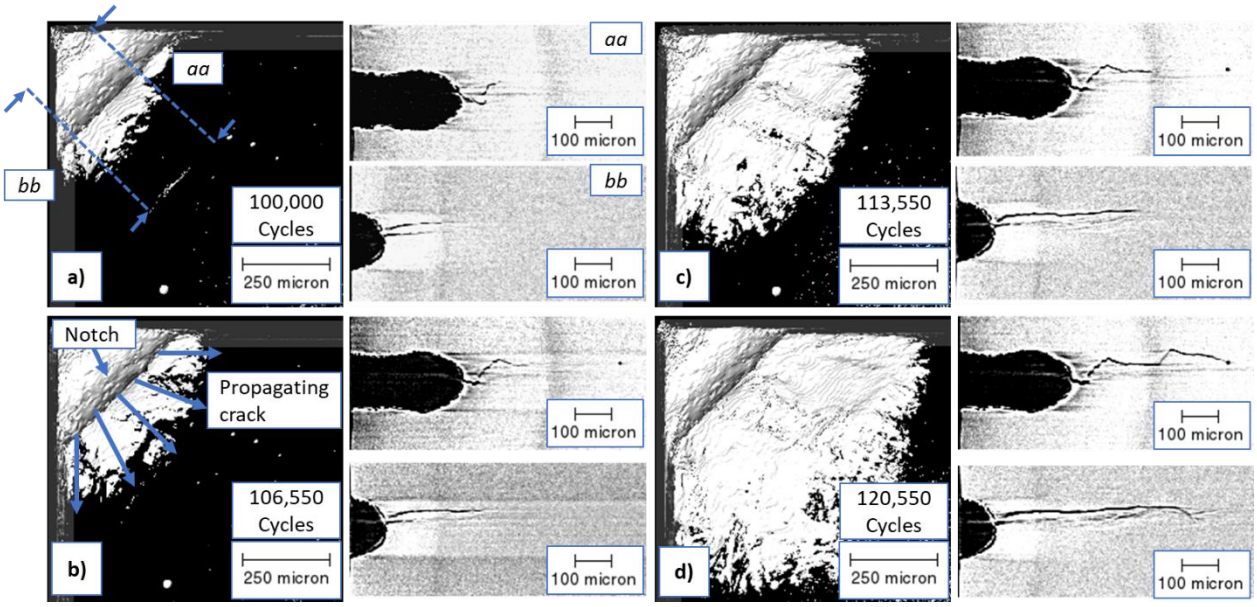

Figure 6.4. Sample 1 crack evolution, (a-d), and orthogonal views described by the sectioning planes 'aa' and 'bb'.

Sample 1 displayed a uniform crack growth pattern as the crack front propagated in a fan like structure, the crack initiated at the notch root, in multiple locations. There was early evidence of an abrupt crack path directional change with 'steps' seen in orthogonal view 'aa' and Figure 6.2. As the crack length grew the morphology became flat with little movement away from a parallel crack path. Bifurcations occur and the crack front encountered or came in close proximity to a small number of the spherical porosity defects, detailed images are included in Section 6.5.1.

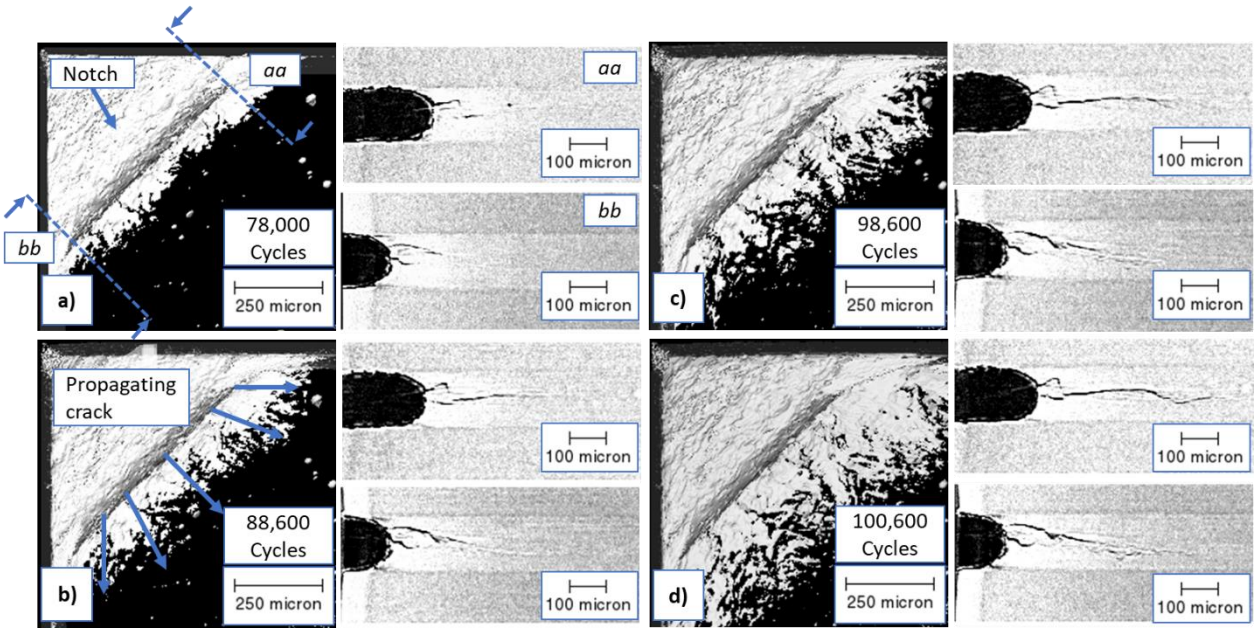

Figure 6.5. Sample 2 crack evolution, (a-d), and orthogonal views described by the sectioning planes 'aa' and 'bb'.

Sample 2 had a similar number of applied fatigue cycles to sample 1 during the in-situ tomography experiment, despite this it is visually obvious there was less crack growth. The crack initiated at multiple locations towards the top of the notch root and tended to grow with a bias towards this side of the notch, as per images (a-d). Although this sample had significant spherical porosity little evidence of crack and porosity interaction was seen. There is evidence of multiple bifurcations and multiple cracks at the notch root and 'steps'. These are limited to first half of the crack growth measured, before the morphology becomes relatively flat. This notch root crack behavior is likely to have produced the variability in the short FCG. To note, the notch was significantly larger (approximately 200 μm deeper than sample 1 and 3) for this sample.

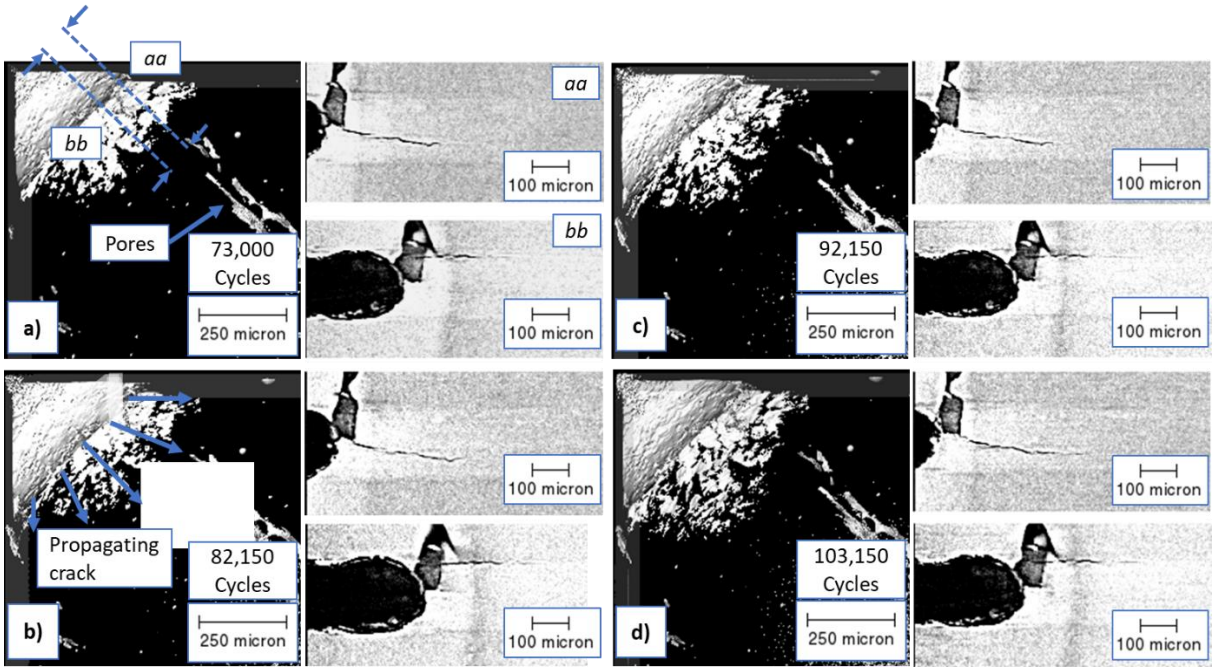

Figure 6.6. Sample 3 crack evolution, (a-d), and orthogonal views described by the sectioning planes 'aa' and 'bb'.

Sample 3 had the most fatigue cycles during the in-situ tomography experiment (30,150 cycles) and also the least visual crack growth. Similar to sample 2 the crack initiated at the top of the notch as per images (a-d). Sample 2 and 3 were mounted in different orientations (vertically 180 degrees different) in the pre-cracking load frame, so any bias to this side of the notch was deemed most likely not due to any off axis loading. Later it was evident that there was a large void/porosity defect at the notch root (shown in 'aa' and 'bb' from either side of the void), the crack probably initiated from two locations on this void. The short crack growth remained relatively flat with no significant 'steps'.

6.4 Scanning Electron Microscope Images

After µXSCT and EDD characterizations samples 1, 2 and 3 were fatigued to fracture under the same loading regime as pre-cracking (Section 3), cycles to fracture are included in Table 3.4. The fracture surfaces were examined using a SEM with the results depicted in Figures 6.7, 6.8 and 6.9. Further details of interest from the SEM fracture surface images are discussed in Section 7. From these images it was possible to gain another data point for the crack growth to cycles measurements taken from the tomography scans. This was computed by overlaying the last tomography crack

surface reconstruction onto the applicable SEM image and measuring from the longest crack length to the beginning of the fast fracture surface. Figure 6.7 shows the sample 1 fracture surface, (a), and an example of this measurement technique, (b), with (c) and (d) being close up images. Of note, the two distinct crescent shaped lines in Figure 6.7 (c), represent the two EDD experiment cycle numbers (122,550 and 124,550). As the scans took 18 hours we see the result of this as a marker bands that required the following fatigue cycles to progress through large plastic zones before continuing. Although striations are not clearly visible we see a relatively flat fracture surface with three distinct steps shown ((c) and (d)).

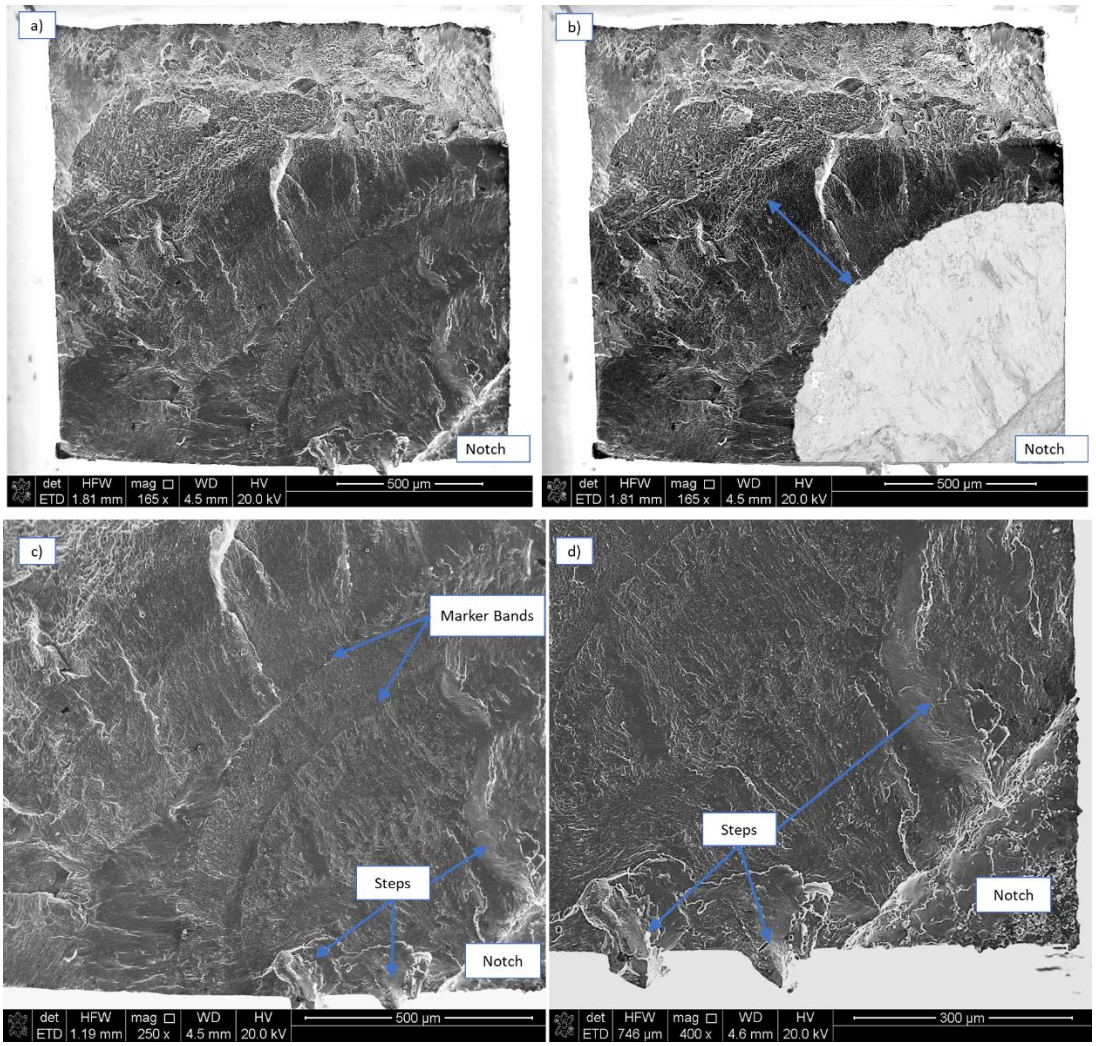

Figure 6.7. Sample 1 post fracture SEM image (148,269 cycles), (a), and measurement technique for crack growth to final failure (tomography scan at 124,550 cycles), (b). Images (c) and (d) are close up fracture surface views.

Figure 6.8 (a), shows the sample 2 complete fracture surface, of note is the visually larger fast fracture surface, a number of pores are also evident and discussed in Section 7, (b) and (c) show close up images. The close up images show a distinctly different fracture surface from sample 2 (trial/horizontal) to sample 1 (optimized/vertical), the fracture surface is less smooth and shows the material being 'pulled' apart as opposed to a clean fatigue crack. There are elongated pores visible in the fast fracture region, (c), which are perpendicular to the propagating crack direction.

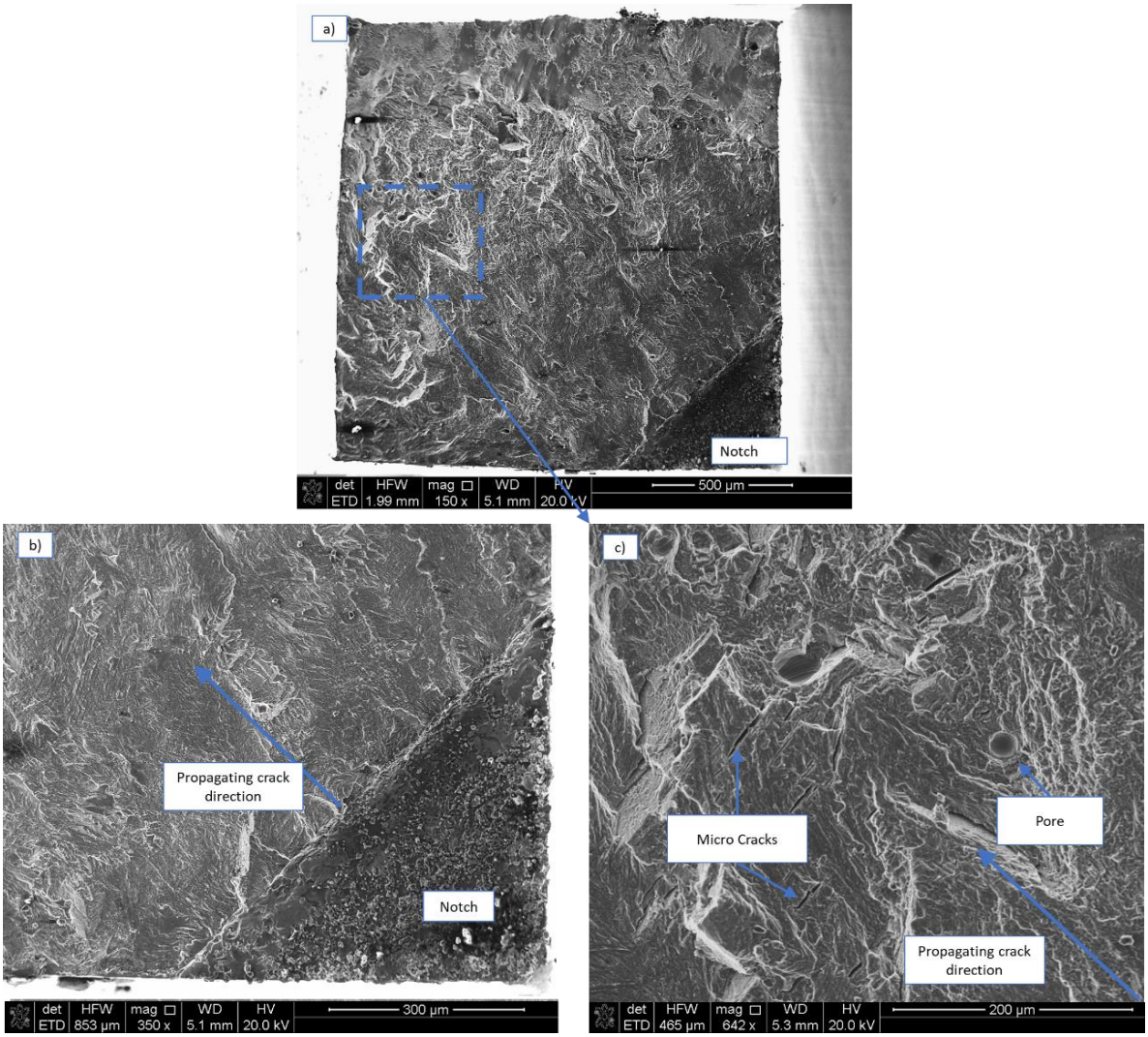

Figure 6.8. Sample 2 post fracture SEM image (123,548 cycles), (a), with (b) and (c) close up images of the fracture surface.

Figure 6.9 (a), shows sample 3 complete fracture surface, (b) and (c) show close up images. Although this sample had significantly less crack growth up to the final tomography scan taken (in

comparison to sample 1), there is evidence of a much larger fatigue crack prior to the fast fracture surface, similar to sample 1. A significant number of pores are evident as well as a long vertical step in the crack surface which was not there until after the scanned tomography crack length. The step is seen running at an approximate 45 degrees, top left to bottom right, this started near the large pore at the notch root and indicates the build layer to notch orientation and potentially the crack preference to the layer interface. The fracture surface of sample 3 (trial/horizontal) and sample 2 (trial/horizontal) exhibit the same behavior of the material being 'pulled' apart despite different notch to build layer orientations.

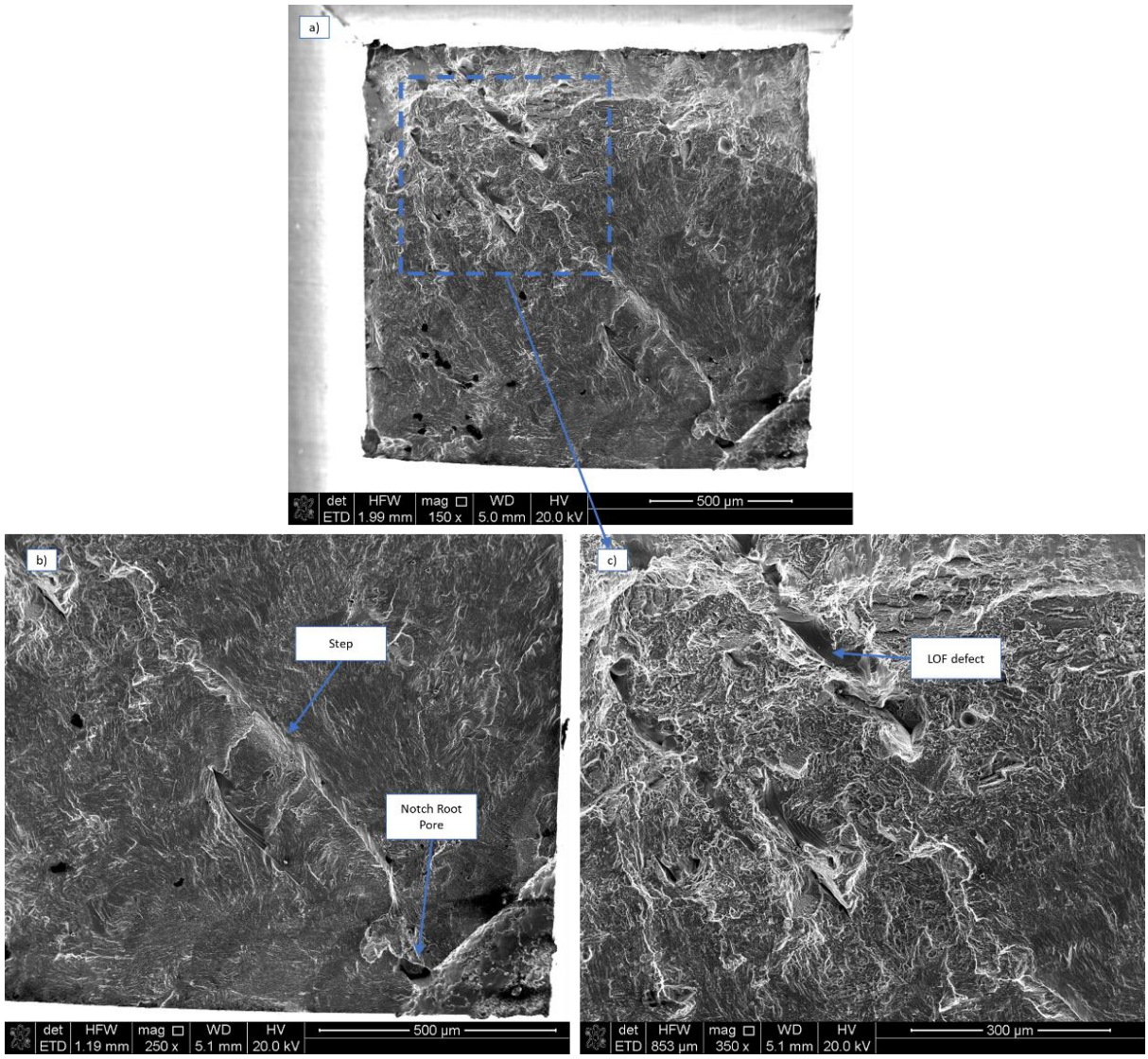

Figure 6.9. Sample 3 post fracture SEM image (140,433 cycles), (a), with (b) and (c) close up images of the fracture surface.

6.5 Results

6.5.1 Crack Deflections, Initiation and Defects

Each sample exhibited very different behavior at the notch root, this early crack behavior is one possible explanation for the significant variation seen in the short crack growth rates. Sample one has three distinct (un-joined) individual notch cracks, as seen in Figure 6.10, the current cycles are 100,000 (pre-crack only) and the largest crack length is 135 μm. The image is looking directly at the notch in the 1 direction (into the page), the cracks are confirmed by the orthogonal slice taken at a distance of 5 μm back from the notch, the crack is growing out of the page in the direction of the reader. Each initiated crack is mostly parallel and the distances between cracks at the notch root are steady, both cracks i) and the lower part of iii) are approximately 30 μm from the plane of crack ii).

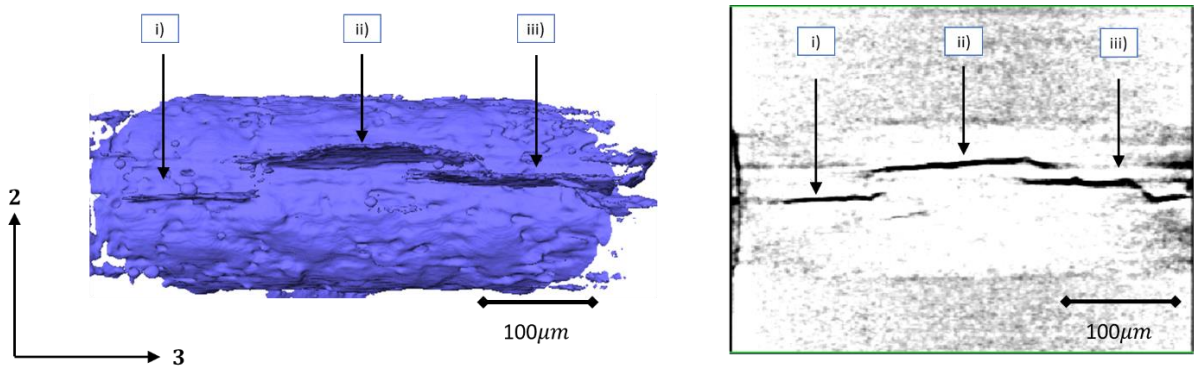

Figure 6.10. Sample 1, 3D Avizo rendering and 2D orthogonal slice at the notch root showing three individual cracks at 100,000 cycles at crack length of 135 μm.

Figure 6.11 shows sample 2, notably there is a larger notch, 200 μm deeper, so the notch face is significantly wider, there is five distinct (un-joined) cracks at the notch face, there is also a large number of micro cracks and evidence of crack bridging and overlap between crack iv) and v). The image is looking directly at the notch in the 1 direction, the orthogonal slice view is taken 5 μm back from the notch face and the cracks show bridging within 5 μm of growth is which is different to the behavior seen in sample 1. The current cycles for this sample are 78,000 and the largest crack length is 162 μm. There is no distinct pattern of distances apart or a preference for a parallel plane, except for crack five every crack is having some movement in the 2 direction (loading direction).

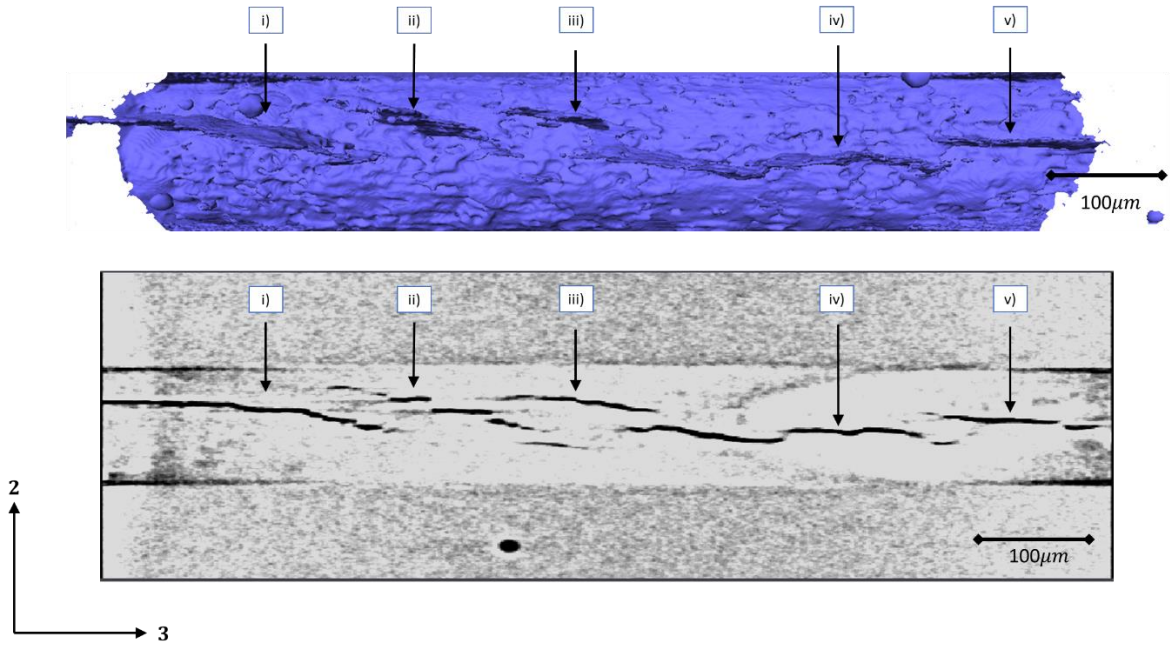

Figure 6.11. Sample 2, 3D Avizo rendering and 2D orthogonal slice at the notch root showing five individual cracks (and numerous micro cracks) at 78,000 cycles and a crack length of 162 μm.

Figure 6.12 shows sample 3 which had a large pore (100 μm tall) less than 5 μm from the edge of the notch. The crack is assumed to have initiated at the pore as it is evident there is two main large cracks either side of the pore. The orthogonal slice view is taken 5 μm back from the notch root, the crack is growing out of the page, current cycles for this sample are 73,000 and the crack length is 215 μm. There are four distinct (un-joined) cracks at the notch face, there is relatively parallel crack growth, although the pore side of the sample is preferred and similar to sample 2 we see crack movement in the 2 direction (loading). Sample 3 had over 200 μm in crack length at the least amount of cycles, at this point the crack growth rate reduced and largely remained static until after 100,000 cycles.

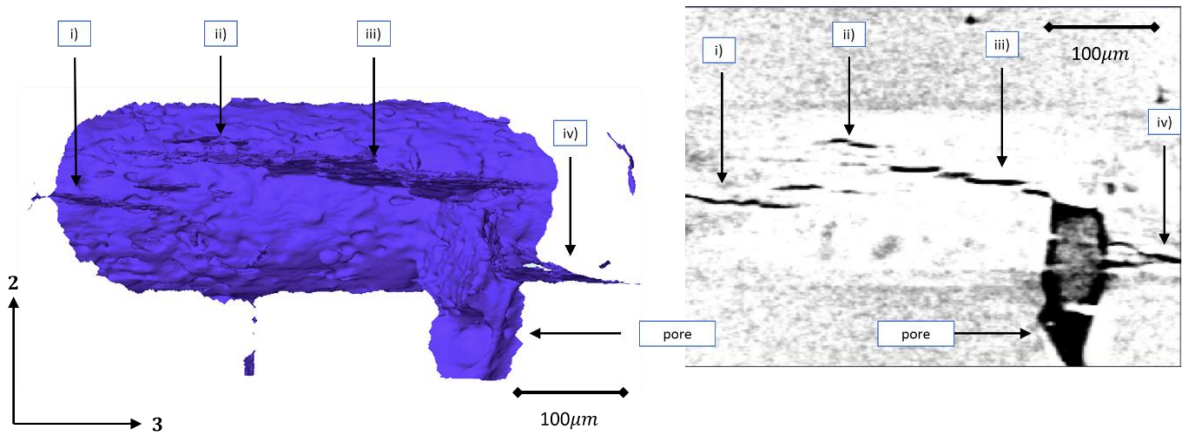

Figure 6.12. Sample 3, 3D Avizo rendering and 2D orthogonal slice at the notch root showing four individual cracks at 73,000 cycles and a crack length of 215 μm.

Sample 1 exhibited a crack bifurcation and steps at the free surface and within the bulk as highlighted in Figure 6.13. To analyze these deflections measurements were taken using orthogonal views and three dimensional renderings in Avizo, the error in measurement is analogous to the tomography scan resolution and added human error, reported values are rounded to the nearest whole number and are indicative only. The three individual cracks had all bridged by 105,550 cycles, the preference for the crack plane was the top crack, ii) in Figure 6.10.

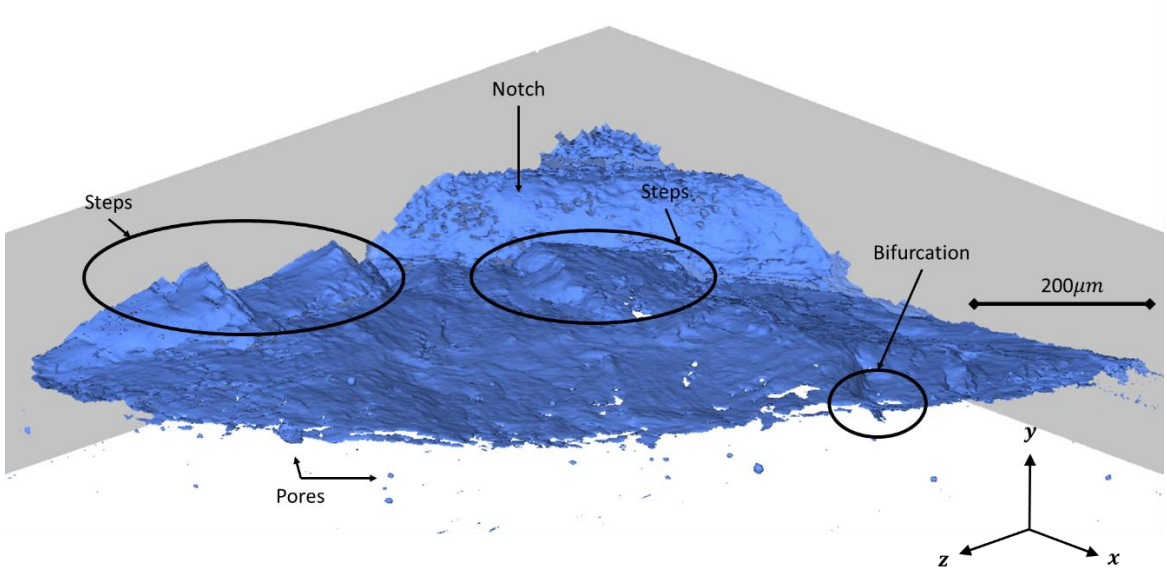

Figure 6.13. Sample 1 at 120,550 cycles, showing steps at free surface and notch root (crack initiation site), a bifurcation has also occurred at the crack front.

The free surface steps are measured and correlated to the applicable cycles to see if there was any impact on the FCG, or any discernable reason for the steps. Figure 6.14 shows the entire crack surface and indicates the largest steps seen, which are at the surface. The steps began below the longer term crack plane and remained between 24 and 50 μm away, by measuring the tortuous crack path and comparing with the indicated 500 μm direct crack length, we see that the steps add approximately 70 μm in length. The crack in this location travels almost 15% more than the crack in the center of the bulk material for the same overall crack length. There is no impact to the crack length to cycles data as this measured tortuous crack was still not the largest crack length in the material. One potential reason for the steps seen and the multiple cracks at the notch is the 30 μm build layer, as sample 1 was of the optimized build condition with less defects, the build layer could be a more dominant driver than the limited porosity seen for the short crack growth.

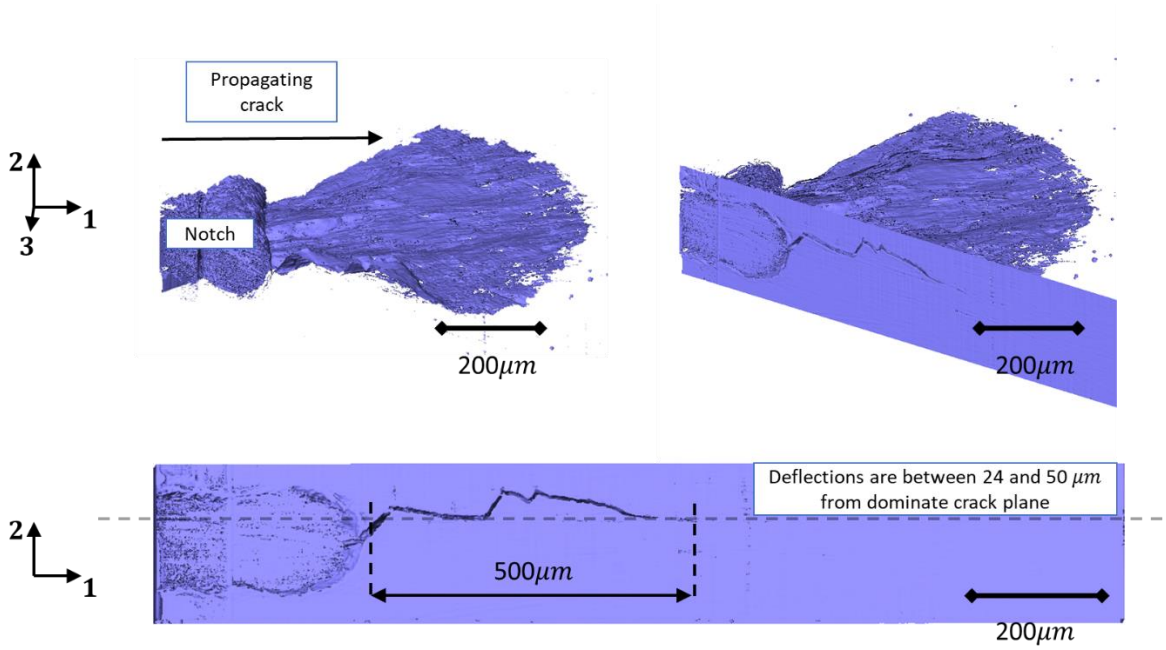

Figure 6.14. Sample 1, 120,550 cycles showing free surface steps and the entire crack surface.

Figure 6.15. shows the two pores that come within close proximity to the fracture surface and a small bifurcation. The large spherical pore marked (i), is 26 μm in width and the small pore is less than 6 μm. In both locations the crack does not deflect towards the pores, the distance between the fracture surface and the pores is under 10 μm. The small pore was located 100 µm from the bifurcation, the large pore was in the bulk of the sample and the crack within the vicinity of both

pores was largely a steady parallel fracture surface. It is likely that the longer crack behavior was dominated by the vertical build direction so the pore was not significant enough to cause a crack deflection. The indicated bifurcation is at an angle of 50 degrees and has a length of 60 μm, the bifurctation occurred as the crack slightly deflected, the other branch of this bifurcation rejoined the main crack plane.

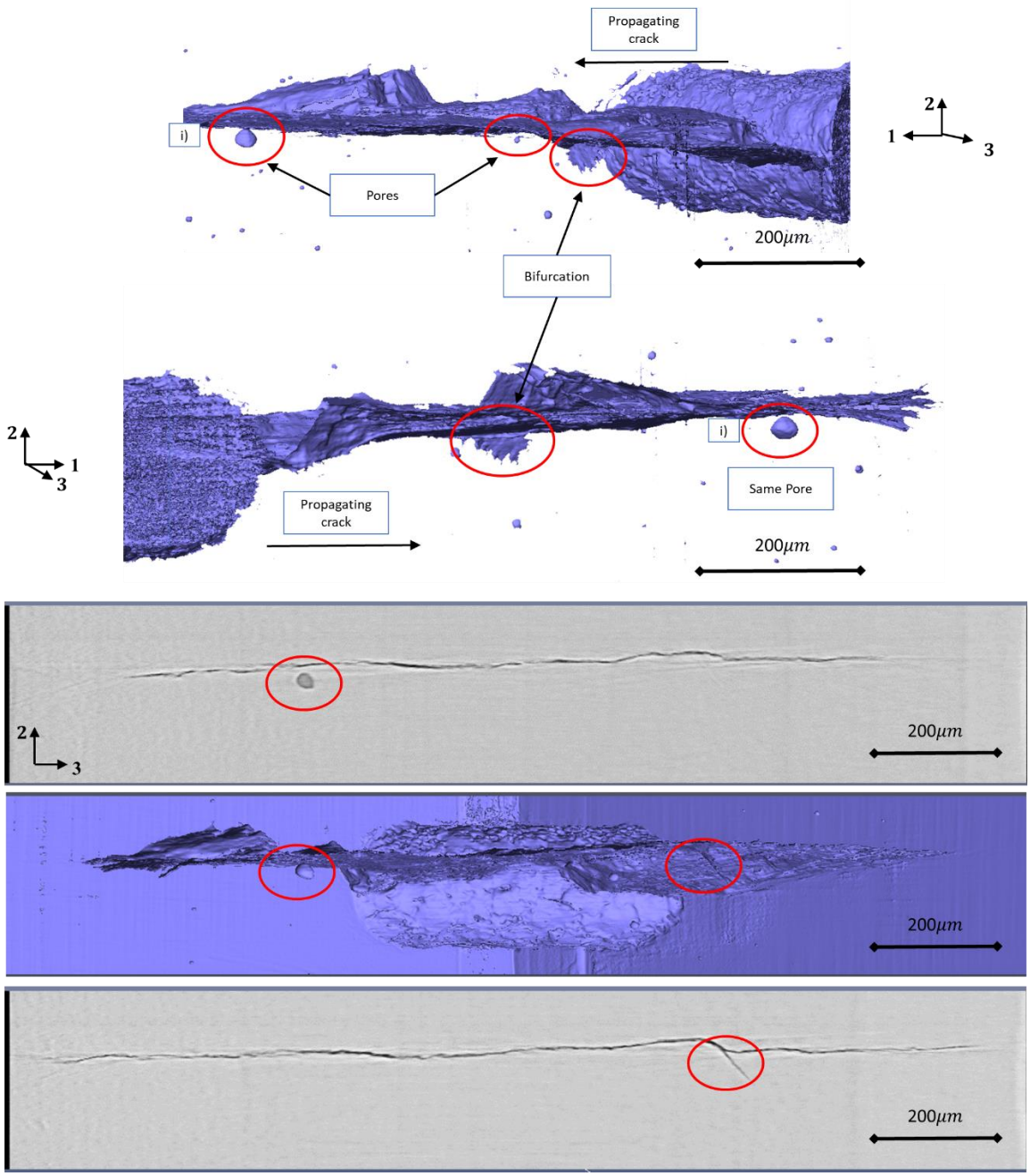

Figure 6.15. Different 3D rendering views showing sample 1 crack surface, pores and a bifurcation, in the bottom images the crack is growing from the notch towards the reader.

Although there was significant porosity in samples 2 and 3 the only encountered porosity defect was sample 3 at the notch root, this adds little scientific information so is not discussed further in the section. Sample 1 however, did have a crack path that propagated through two small pores, a pore of approximately 6 μm and a pore less than 5 μm in diameter. Both of these interactions coincide with steps in the fracture surface and are located within the crack path as the crack amalgamates back with the more dominant steady parallel crack.

Sample 2 and 3 had in common the larger number of disparate cracks at the notch which over a very short period amalgamated with the parallel steady crack plane, the length scale over which this happened was significantly different to sample 1. Sample 2 took approximately 100 μm, sample 3 75 μm and sample 1 300 μm, to become a relatively flat stable single fracture surface, although with some crack deflections still occurring . The extra crack surfaces seen in the first 100 μm of crack growth in sample 2 and 3 can potentially explain the lower FCG rate as there is energy expended in creating these. As the pre-cracking lengths were on the order of 150 μm the fatigue crack growth data reported below does not indicate this variability.

In sample 2 the early steps were larger in number than that seen in sample 1, Figure 6.16 (top) shows a 40 μm step which is typical for this sample and Figure 6.11 shows the number of steps and cracks. Figure 6.16 (bottom) shows the crack plane at a slice 90 μm from the notch, the 'noise' or surface profile of this crack front aligns with the fracture surface seen in the SEM images, Figure 6.8 and differs from that seen in sample 1. Figure 6.17 shows the three dimensional nature of the crack and indicates a small 20 μm crack deviation at the free surface, this was the largest edge deflection seen for sample 2 beyond 100 μm in measured crack length.

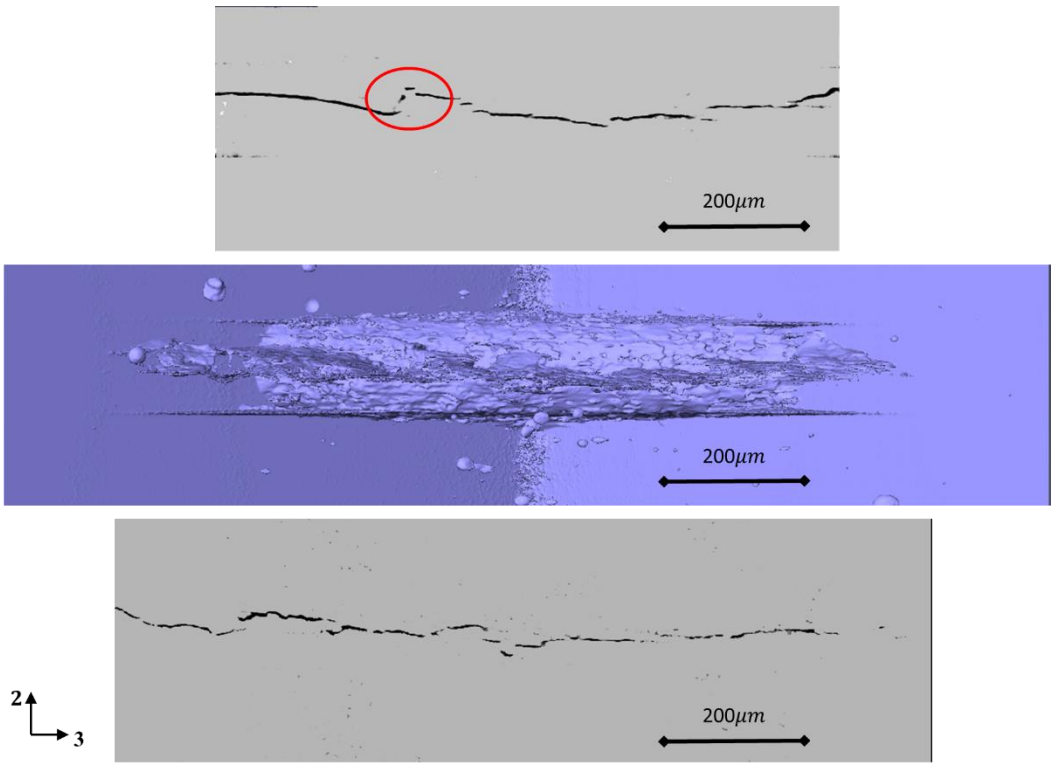

Figure 6.16. Different 3D rendering views showing sample 2 crack morphology, crack growing from the notch towards the reader. 50 μm out from the notch (top) and 90 μm out from the notch (bottom).

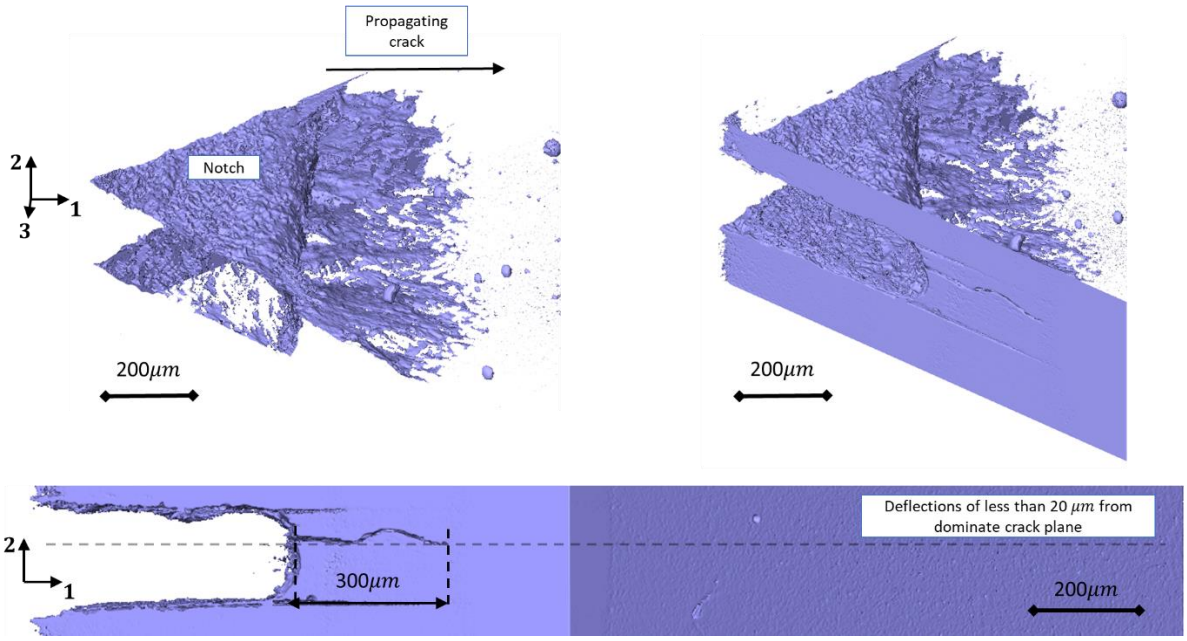

Figure 6.17. Sample 1, 102,6000 cycles showing a free surface step and the entire crack surface.

Sample 3 was a horizontal trial build and did not experience any crack bifurcation or significant steps until after the last tomography scan, the SEM image at Figure 6.9 shows a large step. Largely the crack initiation and short growth seen by the tomography scan was dominated by the significant void directly at the notch root.

As mentioned, the behavior of the multiple initiated cracks at the notch was not captured in the tomography data due to the pre-cracks being longer than the crack length required to amalgamate the individual cracks into one dominant fracture surface. As this behavior is of interest the observed crack deflections, bridging of crack surfaces and any bifurcations are noted in Table 6.2. As the general surface roughness of the fracture surface for sample 2 and 3 (sample 1 is relatively smooth) is of the order of 10 μm, only deflections larger than this 'noise' are reported.

Table 6.2. Showing measurements of observed crack deflections, bridging of cracks surfaces and bifurcations for samples 1, 2 and 3. Minimum crack deflection distance reported, 10 μm.

Sample	Nominal Crack Length (μm)	Distance Deflected (μm)	Note	Location
1	0-30	34	Bridging	Crack length = Pre-crack length
	0-30	35	Bridging	Crack length = Pre-crack length
	0-30	56	Bridging	Crack length = Pre-crack length
	0-30	64	Edge Deflection	Crack length = Pre-crack length
	30-135	35	Bifurcation/Bridging	Crack length = Pre-crack length
	178	57	Bridging	Tomography Scan 5 (102,550 cycles)
	350	58	Bifurcation/Bridging	Tomography Scan 15 (112,550 cycles)
	423	35	Bifurcation/Edge Deflection	Tomography Scan 17 (115,550 cycles)
	632	60	Bifurcation	Tomography Scan 23 (122,550 cycles)
2	0-30	55	Bridging	Crack length = Pre-crack length
	0-30	40	Bridging	Crack length = Pre-crack length
	0-30	34	Edge Deflection	Crack length = Pre-crack length
	0-30	11.7	Deflection	Crack length = Pre-crack length
	0-30	10	Deflection	Crack length = Pre-crack length
	30-50	24	Bridging	Crack length = Pre-crack length
	30-50	74	Edge Deflection	Crack length = Pre-crack length
	50-110	27	Bridging	Crack length = Pre-crack length
	162	20	Edge Deflection	Tomography Scan 1 (78,000 cycles)
	162	34	Deflection	Tomography Scan 1 (78,000 cycles)
	162	29	Deflection	Tomography Scan 1 (78,000 cycles)
	206	39	Deflection	Tomography Scan 9 (84,600 cycles)
3	0-15	25	Bridging	Crack length = Pre-crack length
	0-15	14	Bifurcation at Large Pore	Crack length = Pre-crack length
	183	11	Deflection	Tomography Scan 8 (83,600 cycles)

6.5.2 Short Fatigue Crack Growth

As discussed in Section 2.4, the previous work studied the same material in compact tension form. In that work the authors provide stress intensity range, ΔK, verse crack growth per cycle, $\frac{da}{dN}$ data plots for five sample in the trial build condition, Figure 6.18 replots this data with black and red indicating samples of the equivalent build layer to notch orientation as per sample 2 and 3 respectively [64].

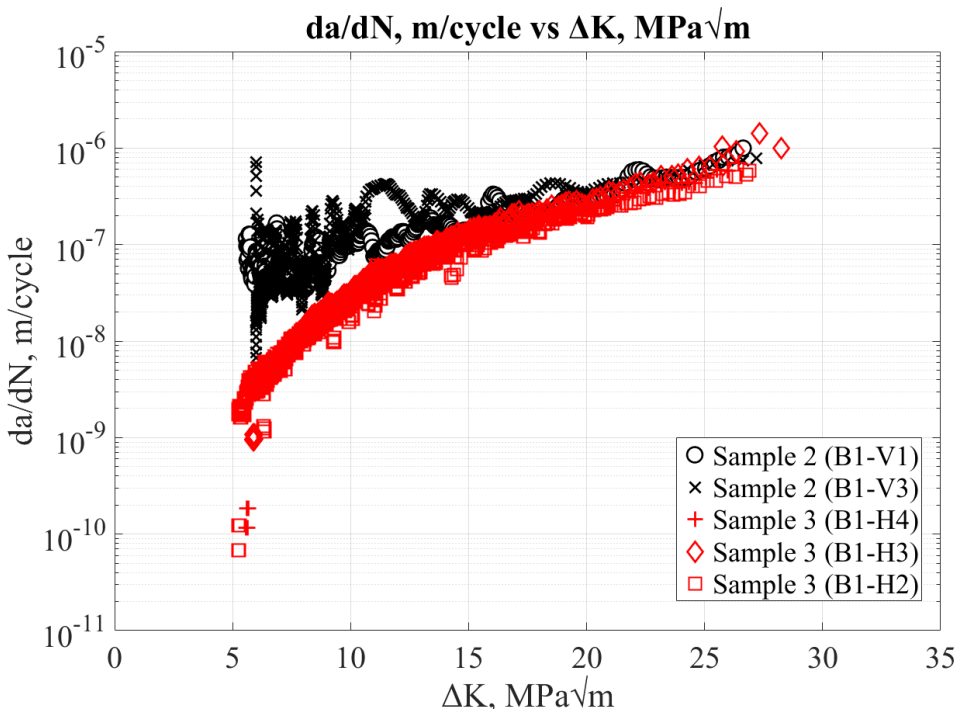

Figure 6.18. da/dN vs ΔK for compact tension samples with the same notch to build layer orientation as sample 2 (black) and sample 3 (red), adopted from Liu et al. [64].

From the short FCG measurements taken (Section 6.2) the crack size verse the number of cycles are plotted in Figure 6.19. Confirming the visual observations, the crack growth rate for sample 1 was significantly higher than for samples 2 or 3. Of note, the number of cycles to the start of the fast fracture is the final data point and was measured as per Section 6.4. Samples 1, 2 and 3 fractured at 148,269, 123,548 and 140,433 cycles respectively.

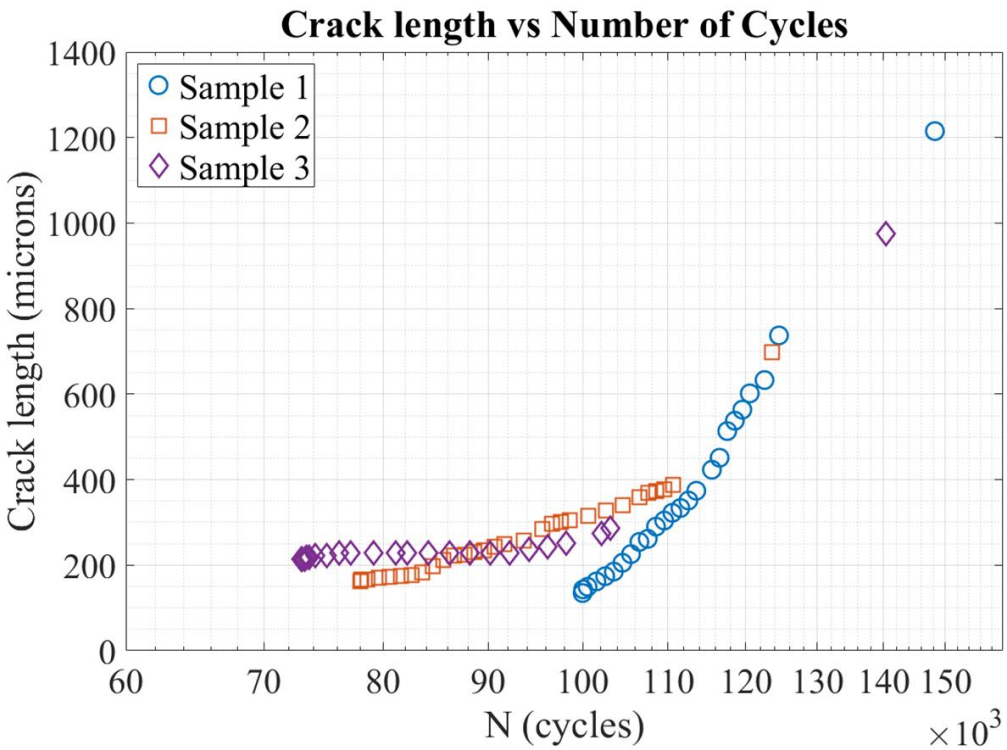

Figure 6.19. Crack length vs cycles plot for samples 1, 2 and 3.

6.5.3 Microindentation Hardness

Vickers Hardness (VH) testing was conducted on samples 1 and 2 to establish any difference between the apparent strength of the two build conditions. The VH testing followed ASTM E384-17, with the use of a line of ten indentations at 30 μm apart, as depicted in Figure 6.20 [99]. A force of 25 gf and a time of 13 seconds per indentation was used. Results are given in Table 6.3, the trial build conditions have a significantly lower VH result.

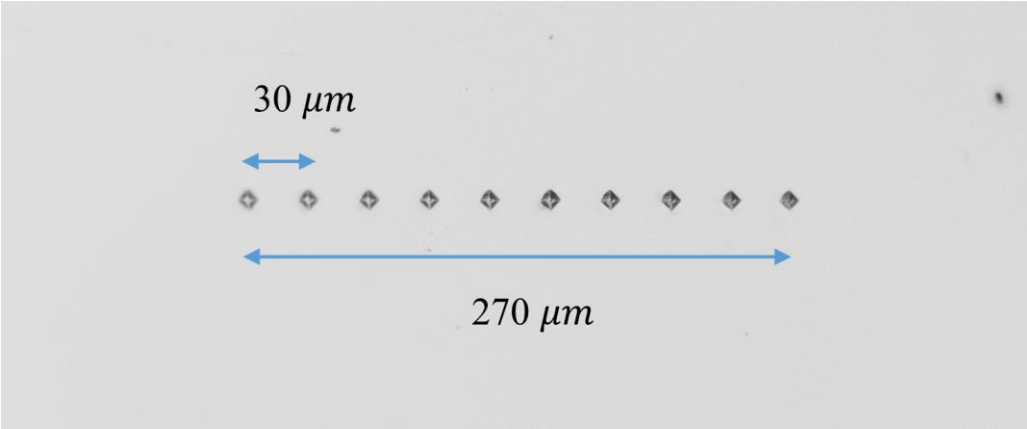

Figure 6.20. Vickers Hardness indentations on sample 2.

Table 6.3. Results from Vickers hardness microindentation testing on two different build conditions.

	Sample 1	**Sample 2**
Build Condition	Trial	Optimized
Mean VH	365	430
Median VH	365.36	432.01
Standard Deviation	14.81	7.29

6.6 Discussion

Motivation for this work comes from the lack of understanding of the short FCG and particularly the lack of literature on short FCG in additive manufactured Ti-6Al-4V. Current availability of crack growth data for AM Ti-6Al-4V is restricted to researchers considering the long FCG properties. Understanding the mechanism for short FCG variability may help to understand the variance in fatigue properties seen in long FCG studies.

From the literature review we know that the short crack growth will be highly dependent on microstructural characteristics and we expect the material tested to have a fine α' microstructure [1]. We also expect to have a prior β grain influence on strain localization and most importantly build layers showing as tracks at fixed intervals within the microstructure. The material tested has

had the parent CT sample microstructure previously characterized. For sample 2 and 3 equivalent materials (trial condition) the microstructure showed the formation of columnar prior β grains and equiaxed prior β grains, notably the prior β grains are separated by the build layers [64]. Sample 1 was similar with columnar prior β grains along the build direction [64].

Viet Duc le et al. clearly shows these elongated columnar grains in the building direction, notably this corresponds to perpendicular to the crack path in sample 1 [41]. One of the questions in the reviewed study was which of the two parameters, the microstructure (build direction related) or the porosity was more damaging to fatigue properties. Similar to this work Viet Duc le et al. also reported the worst fatigue properties for the crack front parallel to the build direction (8mm dog bone samples), for long FCG tests [41]. A clear link to porosity was shown for samples with build directions equivalent to sample 2 and 3 but inconclusive for samples equivalent to sample 1.

In terms of reported long FCG rates for as built SLM Ti-6Al-4V there is conflicting reported data on the fatigue resistance of sample 1 equivalent tests, with the build layer and crack plane parallel. Leuders et al. reported significant variation in the FCG rate for sample 1 equivalents and a similar but slightly lower FCG rate for sample 2 equivalent, at low ΔK values (although with less scatter) [2]. At high ΔK values sample 1 equivalent tests had significantly higher FCG rates [2]. Cain et al. differ as they reported FCG rates for sample 2 equivalent build directions as higher than the sample 1 equivalent [3]. For these reported results the microstructure and residual stress are deemed the dominant drivers. In terms of the sample 1 short FCG reported in this study, we have shown that having the crack plane parallel to the build layer is the most damaging, we have also shown that the measured crack deflections appear to be related to the size of the build layer (discussed below). Also the relatively flat fracture surface implies that the crack is likely propagating along the build layer.

Cain et al., Edwards and Ramula, Leuders et al. and Liu et al. all found that the crack plane to build direction equivalent to sample 3 has the highest FCG resistance for as built SLM Ti=6Al-4V [2], [3], [5], [64]. Within this work we see the short fatigue crack growth behavior follow this trend. Cain reports a fracture toughness as significantly higher for the sample 3 build direction over 1 and 2 [3]. Similar to the results shown in Figure 6.18, Leuders et al. shows a decrease in the

variability of the FCG at higher ΔK for sample 2 build directions [2]. If the columnar grain structure reported in the sample 2 CT parent is aligned with the crack plane, this could be expected to increase the FCG rate, this is contrary to the results in literature and this study. The fracture surface for sample 2 was characterized as 'rough' and this sample exhibited the most crack deflections. There was also a significantly larger number of independent crack surfaces through the initiation and early growth. This sample was of the trial build condition and had a large number of defects, we expect some local elastoplastic behavior which would cause toughening of the material. The effects of residual stress relative to the crack plane, as discussed by Vranken et al. show that FCG rates for sample 2 and 3 orientations should be similar, this study finds the short FCG rates to agree [58]. Furthermore, Cain et al. suggests the microstructure anisotropy to be slightly more favorable for fatigue resistance in sample 3 equivalent tests, again this work agrees [3]. Sample 3 had little or no crack deflections, this suggests the more favorable microstructural anisotropy could be a reason for the lowest short FCG rate.

The crack deflections for as built AM Ti-6Al-4V in the near threshold region have been studied by Galarraga et al., the study shows that for cracks growing parallel to the horizontal or vertical build direction different mechanisms cause deflections [100]. The build layer for that study was 50 μm and the crack locally was shown to deviate from the average propagation plane over distances in line with the microstructural features, for sample 1 equivalent build directions. The build layers were shown to contribute to the deflection of the crack front, although these region boundaries contained complicated microstructures [100].

Sample 1 had the largest crack growth per cycle of all three samples yet the build condition was optimized (reduced size and occurrence of porosity). The fracture surface was smooth and the crack growth typical. Of the nine crack defections measured four were of the order of 30 μm and five were of the order of 60 μm, this suggest a correlation to the build layer. Crack propagation along the build direction in this work is shown to be the most damaging.

As the material studied in this work contains a predominately fine α' microstructure the preference for the steps seen is likely related to the build layers, the steps shown in Galarraga et al. were related to the coarse alpha regions typical of EBM, whereas SLM does not exhibit these

regions [100]. Furthermore, in the presence of fine microstructures the crack paths were shown to be largely continuous [100]. Tao et al. also states that for an α' acicular martensitic microstructure the crack path is less tortuous due the grain structure [101].

The fatigue resistance to crack propagation has been shown to relate to the size of movements away from the parallel propagating crack path [102]. Overall sample 2 did exhibit more movements away from the parallel crack plane, this was most evident in the initial crack growth (crack length < 100 μm). This early crack behavior is likely to explain some of variation seen in the reported long FCG rates. Leuders et al. have reported considerable variation in the as built SLM AM Ti-6Al-4V which is significantly reduced with heat or HIP treatments [2]. As this removes build layer induced residual stress and changes the grain size the short crack path deflections could explain the lessor variation seen.

The long crack studies reviewed consider cracks that have a length and width considerably larger than size of the microstructural influences whereas the cracks in this work progress from microstructurally small to physically small (Table 1.1), the FCG properties of these different scale cracks differs considerably. Clearly further work is required to understand all regions of crack growth, particularly the microstructurally small crack deflections as seen in sample 1 and 2.

The same researchers mentioned above have also considered the residual stress and strongly suggest that the influence of porosity on the fatigue strength is larger than the influence of the microstructure [2]. To further understand the role of porosity Section 7 is used to characterize these defects.

7. POROSITY AND LACK OF FUSION ANALYSIS AND RESULTS

7.1 Background and Overview

Section 2 and the results from the previous work on the CT parents, showed that porosity was likely a significant driver in the variation of crack growth seen between samples [64]. As researchers have shown the irregular elongated pores can cause crack initiation and any defects can cause strain accumulation or carry plastic deformation (damage). As the damage tolerance of the tested material is likely a function of the size, number and shape of pores within the gauge volume an investigation was undertaken. Within this section, using Avizo, the pores in samples 1, 2 and 3 are characterized with respect to characteristics, sphericity, volume and quantity.

7.1 Measurement Methods

With reconstructions that have well defined contrast between the bulk material and cracks/pores Avizo can be used to isolate and analyze the porosity from tomography scans. There are numerous variables and this is again an iterative process. To confirm the shape and size of pores ImageJ was used to match pores and confirm the segmentation was correct. Of note, there is a threshold for upper and lower volumes of the segmented porosity that Avizo recognizes. The lower bound was set to 3 pixels in all directions for a minimum volume of 27 voxels, resolution is 1.3 μm. The upper bound was adjusted for each sample to remove the crack surface as this was recognized as a large pore.

Once optimized Avizo produces a table of results in which each pore can be physically identified via a set of cross hairs, the table contains data which includes the volume, area, center location and greatest length. Figure 7.1 shows an example of a highlighted pore (large green LOF defect) in sample 3, included is an extract from the data tables for this pore (in blue).

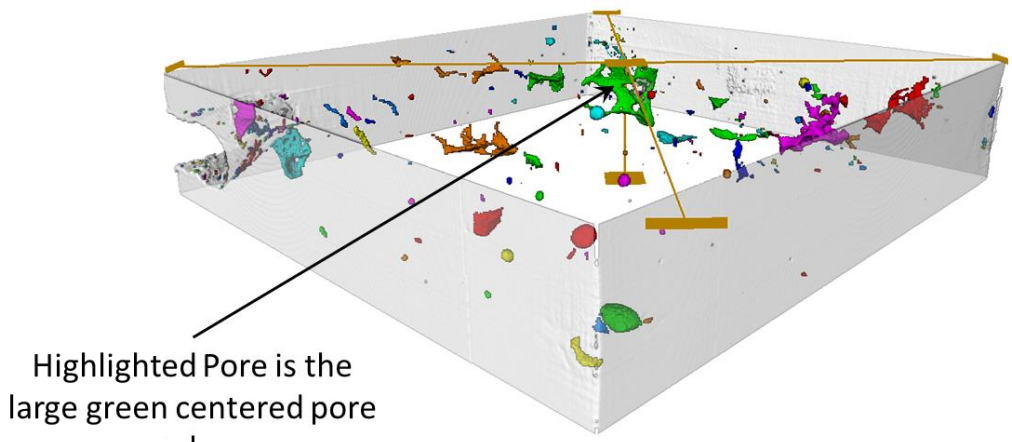

	Volume3d	Area3d	BaryCenterX	BaryCenterY	BaryCenterZ	Mean	FirstPointX	FirstPointY	FirstPointZ	Minimum	Maximum	Length3d	index
1	37812	15839.6	968.386	263.41	63.0231	1	965	224	0	1	1	152.216	3
2	78864	35108.8	807.557	766.58	61.6518	1	804	776	0	1	1	172.456	4
3	3867	1318.27	472.876	935.384	6.93457	1	475	926	0	1	1	25.2909	6
4	9357	4385.84	688.239	1067.13	35.0227	1	678	1059	0	1	1	85.502	7

Figure 7.1. Example of the Avzio data attributed to each identified pore, pore of interest (large green) highlighted by the yellow cross hairs.

From this table any indicated porosity within the notch area/crack surface were manually removed by considering the location data and confirming on the three dimensional volume. Then a set of data for pores within the bulk of the material was created. The volume fraction, V_f, was computed by summing the pore volumes, V_p, and dividing by the gauge volume, V_g, (with notch volume subtracted) in voxels as per Equation 7.1. Table 7.1 contains the results and applicable volume measurement values. These results are in line with Leuders et al. and Kasperovich et al [2], [55].

$$V_f = \frac{V_p}{V_g} \tag{7.1}$$

The sphericity, φ, of each pore was calculated using Equation 7.2 with values for the volume of each pore, V_p, and area of each pore, A_p, taken from the Avizo porosity analysis data table.

$$\varphi = \frac{\pi^{\frac{1}{3}}(6V_p)^{\frac{2}{3}}}{A_p} \tag{7.2}$$

Table 7.1. Volume fraction calculation data and results. Note, all volumes are in μm^3.

Sample	Gauge Volume (µm³)	Pore Volume (µm³)	Volume Fraction	Density (%)
1	8.61E+08	2.22E+04	2.58E-05	99.990
2	8.55E+08	6.05E+05	7.08E-04	99.929
3	7.28E+08	1.07E+06	3.20E-03	99.853

7.2 Visualization

The visualizations shown in Figures 7.2, 7.3 and 7.4 correlate the results of the volume fraction calculations. Furthermore, the non-spherical irregular pores are clearly visible in sample 3 and the larger average pore volumes in sample 2 are evident, when compared with sample 1.

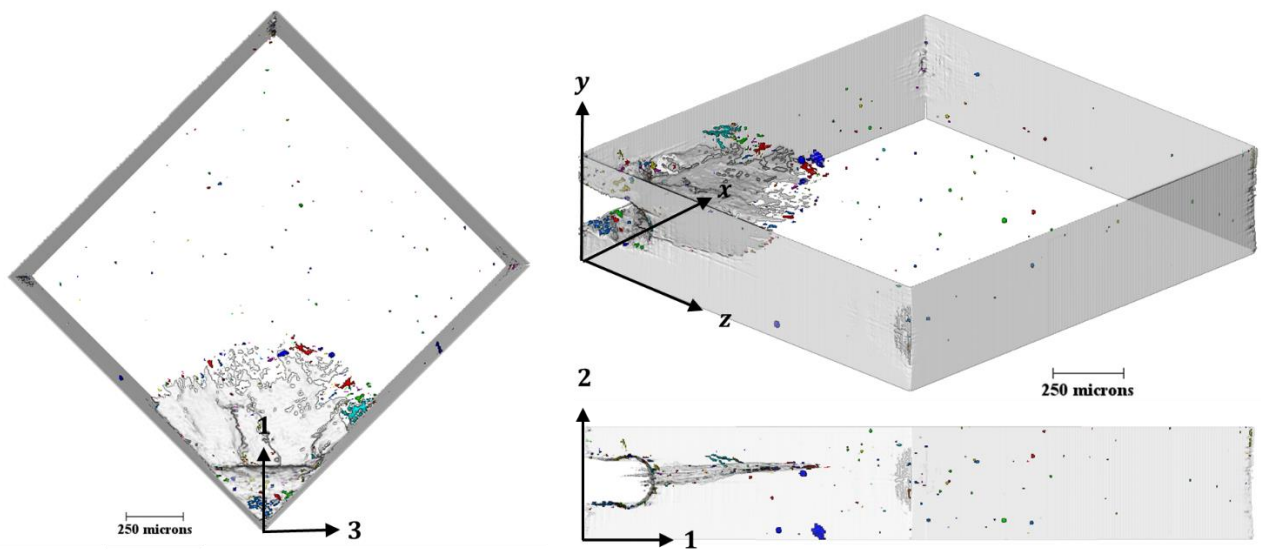

Figure 7.2. Sample 1 showing pores highlighted in color from the Avizo porosity analysis.

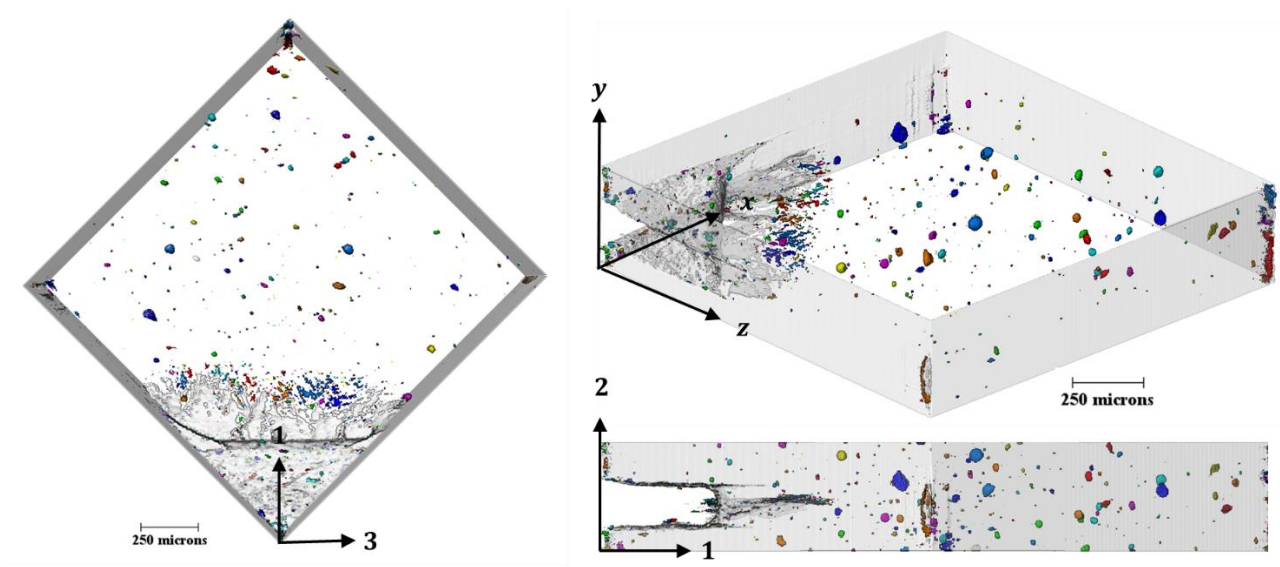

Figure 7.3. Sample 2 showing pores highlighted in color from the Avizo porosity analysis.

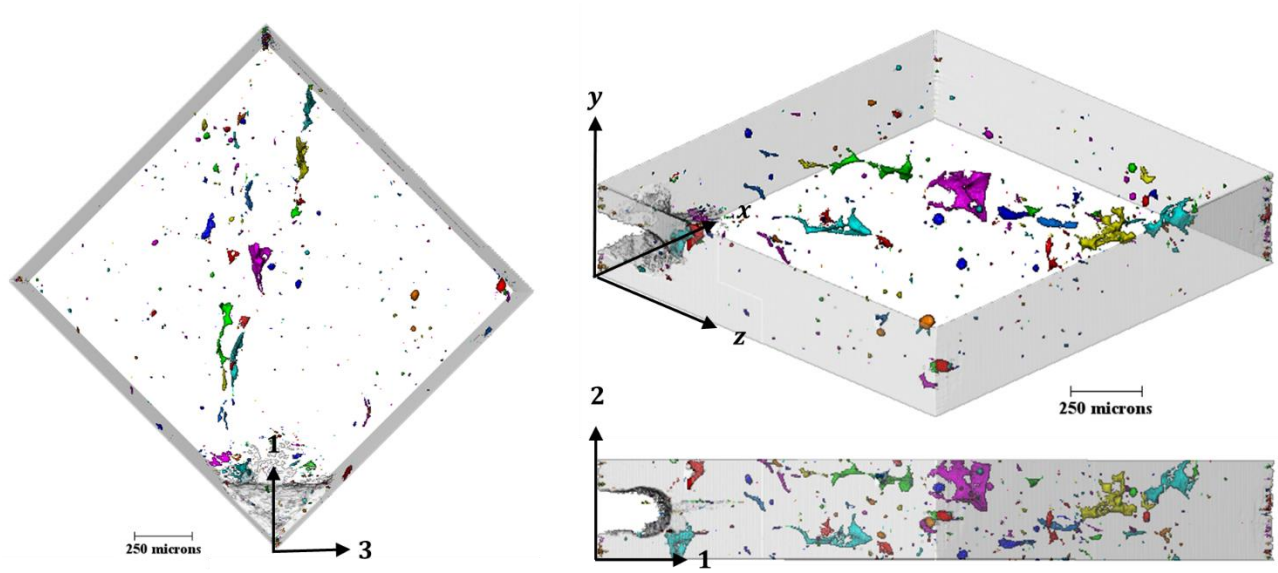

Figure 7.4. Sample 3 showing pores highlighted in color from the Avizo porosity analysis.

The extremely irregular pores can be examined as a surface such as Figure 7.5, which shows the sharp nature to the defect which could cause a local stress concentration point and possible fatigue crack initiation. The pore depicted is from sample 3, largest pore in Figure 7.4 (purple color).

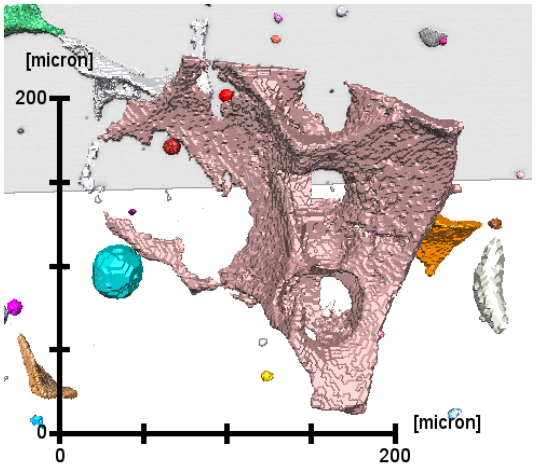

Figure 7.5. Exploded view of the largest pore seen in sample 3 (purple pore in Figure 7.4).

7.3 Scanning Electron Microscope Images

The porosity highlighted in the three dimensional renderings was also examined using an SEM on the post fracture surfaces of samples 1 – 3 and on sample 5. Figure 7.6 - 7.9 depict various porosity defects as discussed below. Figure 7.6 shows two of the pores seen in sample 2, notably within the pores is possible evidence of ridges which have been shown by Kasperovich et al. to be caused by fast cooling rates [55].

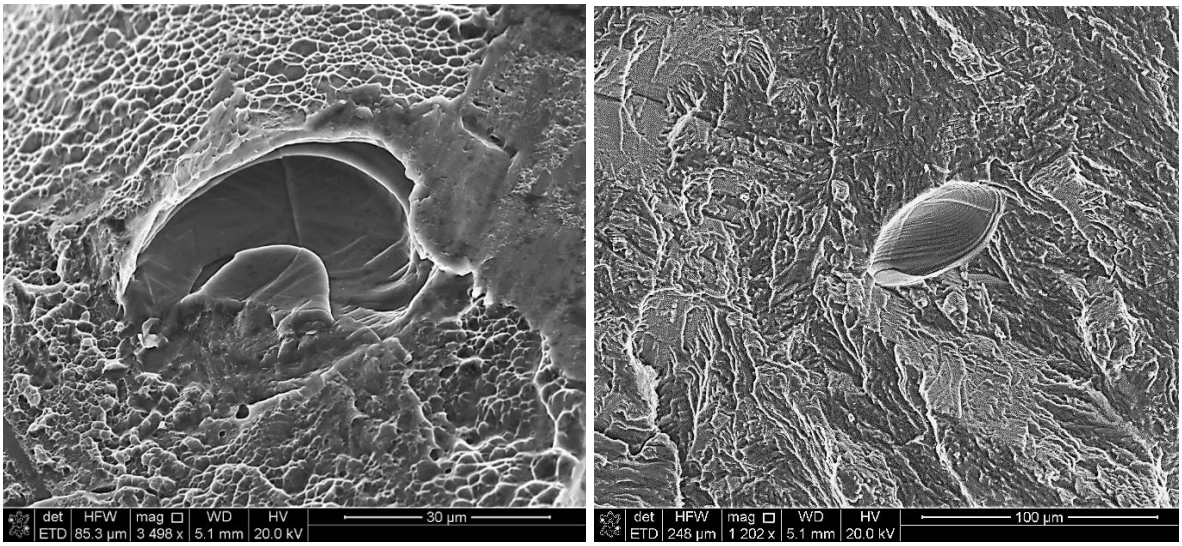

Figure 7.6. SEM images of sample 2 semi spherical porosity (both) showing possible internal ridges (right).

Figure 7.7 depicts sample 3 elongated irregular pores, within the pore (right) there is significant cracking evident and potential interconnectivity with the lower pore. The extreme sharpness of the pores within this sample is particularly apparent and the round structure inside the pore is why Figure 7.5 has its peculiar shape (left).

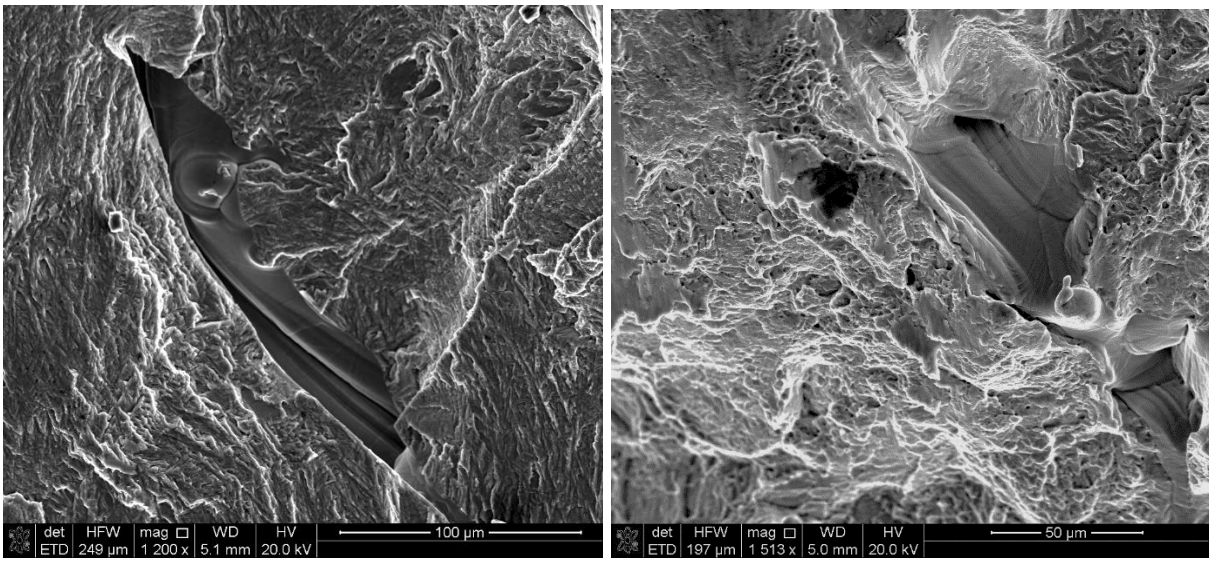

Figure 7.7. SEM images of sample 3 elongated and irregular shaped porosity.

Figure 7.8 is also from sample 3 and shows again an example of a round shape protruding into the cavity responsible for the form of Figure 7.5.

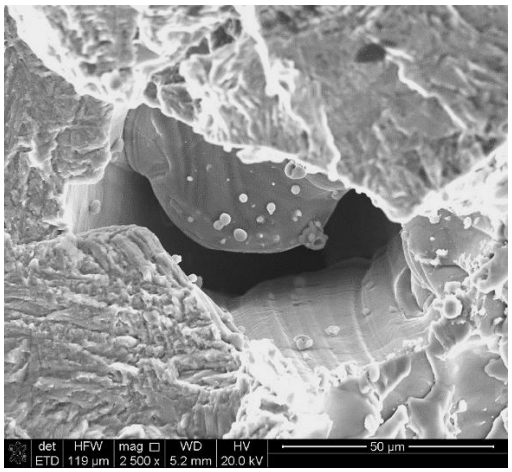

Figure 7.8. SEM image of sample 3 showing a LOF defect.

Sample 5 fractured during pre-cracking at a considerably lower number of fatigue cycles (24,200) and was not characterized further via µXSCT or EDD during this work. When inspected for defects with the SEM there was a large interconnected porosity defect (length > 600 µm) that included a number of un-melted powder particles. Figure 7.9 shows the extent of the defect which likely caused the low cycles to failure.

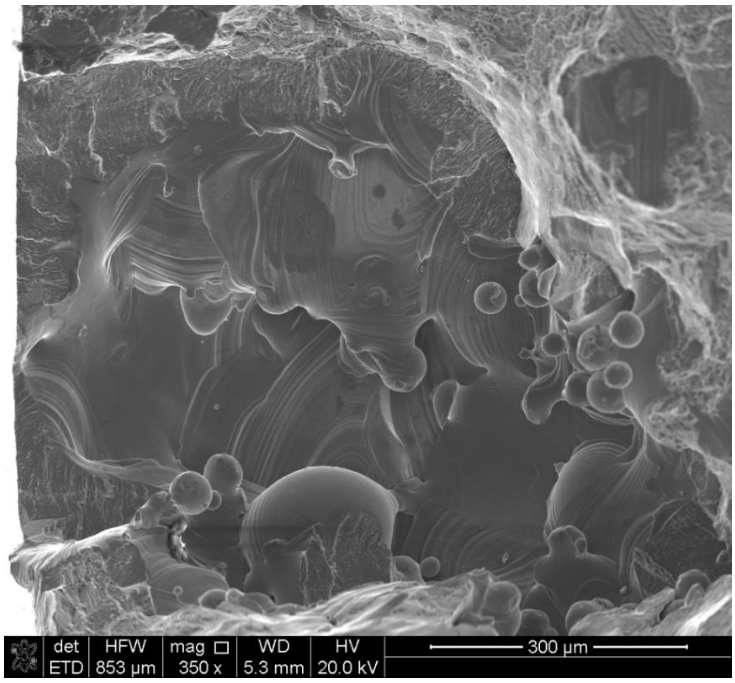

Figure 7.9. SEM image of sample 5 showing large (> 600 μm) porosity defect as the possible cause for failure at 24,200 cycles.

7.4 Build Direction

From literature we that know that LOF defects are related to the build direction as they are elongated in the direction parallel to the build layer and perpendicular to the build direction [49]. From Figure 7.4 we can see distinct lines of elongated pores slightly off axis in the 1 direction. In Figure 7.8 the expected build layer orientation has been marked with black dotted lines and the sample schematic given as a reference to the sample build layers and build layer to notch configuration. A step in the fracture surface discussed in Section 6 and shown in Figure 6.9 was also parallel to the elongated pores, this step is aligned with the large pore at the root notch.

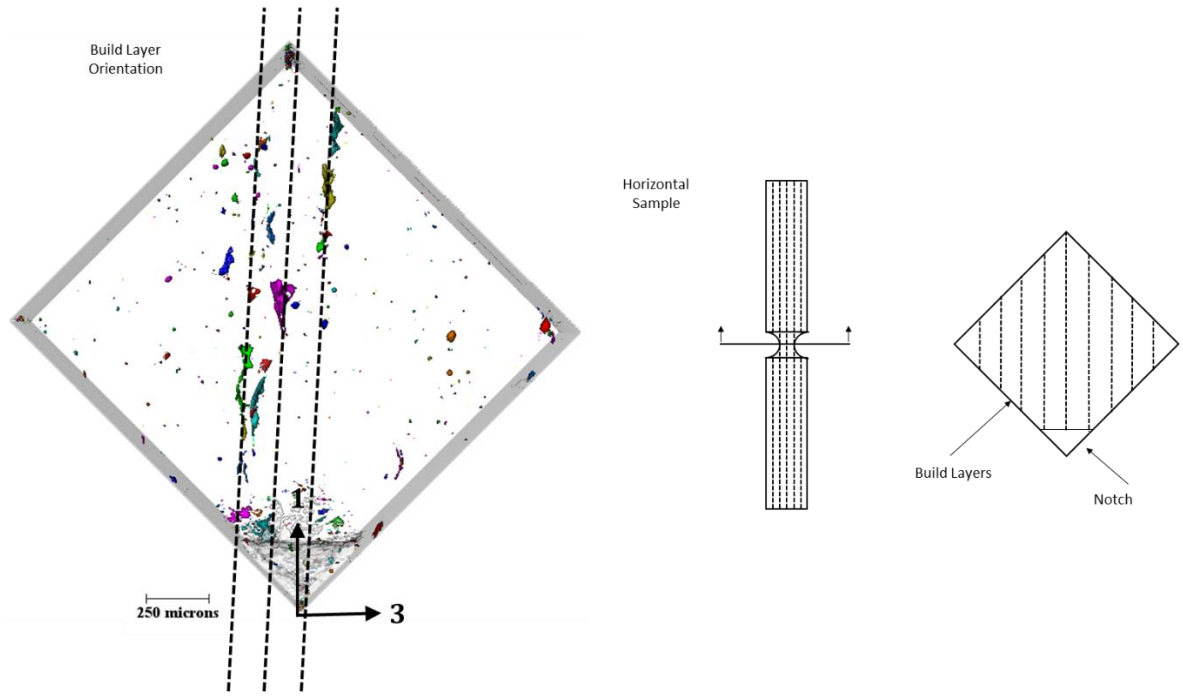

Figure 7.10. Sample 3 likely build layer to notch orientation using LOF defects elongated lengths as indication. Sample schematic from Figure 3.5 shown to illustrate build layers.

Sample 2 did not exhibit the obvious elongated pores from the porosity analysis within the gauge volume used for tomography scans, however from the fracture surface SEM images we can infer the build layers by considering the pores that became evident during the fatigue cycles post tomography and prior to final fracture. Figure 7.11 shows the elongated porosity defects evident from the SEM images in the fast fracture region, used to infer the build direction and an approximate schematic showing the build layers.

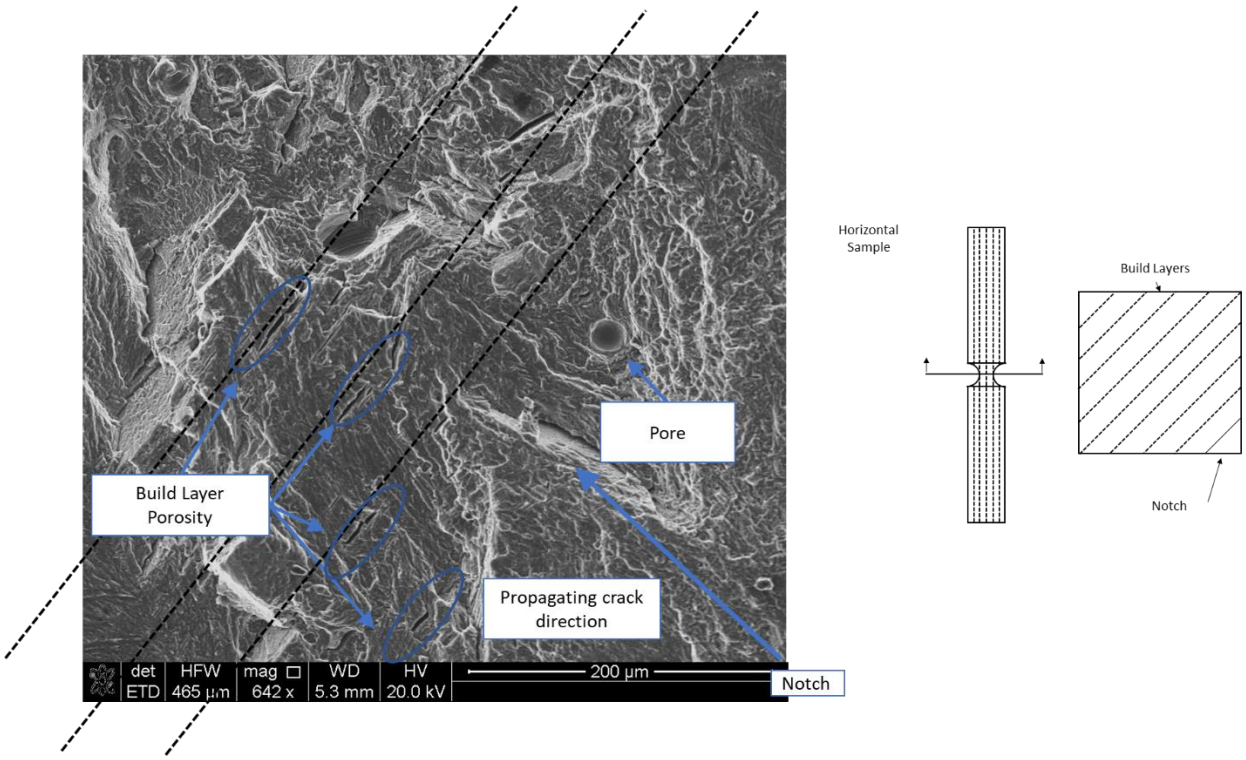

Figure 7.11. Sample 2, elongated porosity defects evident from the SEM images in the fast fracture region, used to infer the build direction. Sample schematic from Figure 3.5 shown to illustrate build layers.

7.5 Results

The results of the porosity analysis are presented as two cumulative distribution function (CDF) plots. The CDF plot at Figure 7.12 is the volume of pores (for pores >27 voxels), this gives an indication of the numbers of large pores and spread. To note, the total numbers of pores was 38, 194 and 268 for samples 1, 2 and 3 respectively. Figure 7.13 shows the results from the sphericity calculations using Equation 7.2, with a value of 1 meaning a perfect sphere.

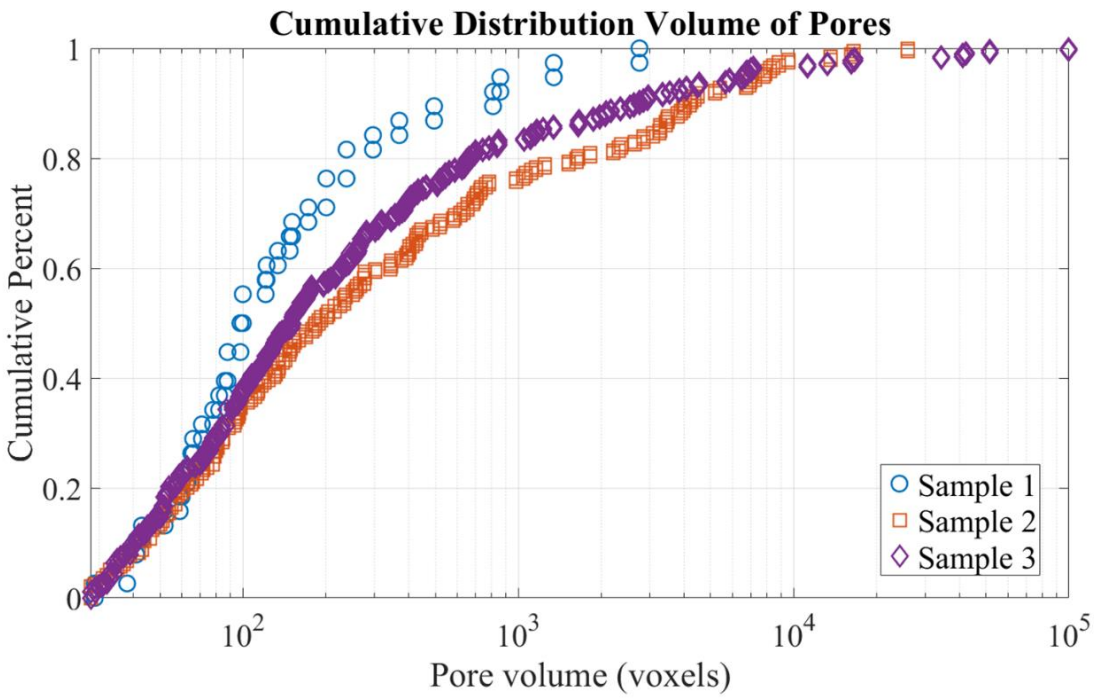

Figure 7.12. CDF plot of pore volumes with a minimum threshold set at 27 voxels.

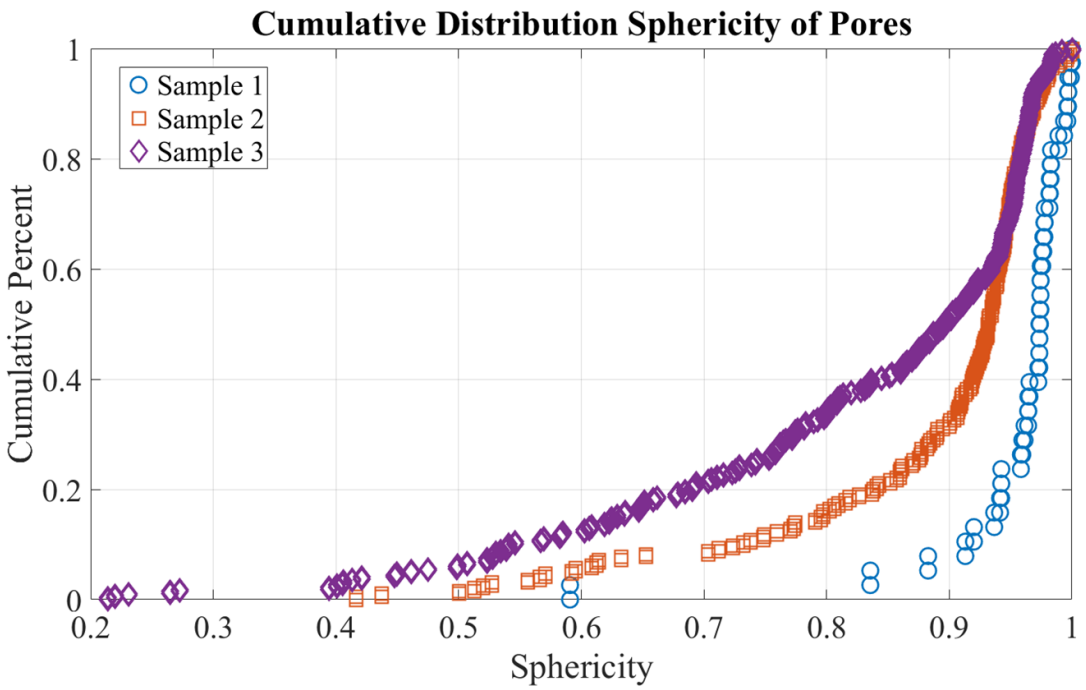

Figure 7.13. CDF plot of the sphericity of all pores above the minimum threshold of 27 voxels.

7.6 Discussion

Leuders et al. showed that for samples that failed at considerably lower cycle counts, generally the cracks had initiated from porosity defects [2]. Of the four samples fatigued to fracture, sample 5 was the only early failure, this was shown to agree with literature, a large LOF porosity defect was evident in SEM imaging (Figure 7.9) and this is the likely failure mode. Largely the threes samples considered had distinctly different porosity characterizations.

Sample 1 had the lowest volume fraction and the most spherical pores, this sample also had the largest crack growth rate with a typical fan shaped crack emanating from the corner notch. Sample 2 had the second largest volume fraction and majority of pores above the critical sphericity value of 0.7, suggested by Kasperovich et al. [55]. The crack growth was less than sample 1 and the fracture surface much less smooth. Sample 3 had the largest volume fraction and the largest number of pores below a sphericity value of 0.7, this indicates a significant number of potential stress concentrations points. This sample exhibited LOF defects throughout the bulk of the material and a significantly lower crack growth rate.

All three samples (1-3) reached final fracture between 120-150,000 cycles, although they had very different defects and fracture surface characteristics. The main difference was the cycles to pre-crack which include the initiation through to 150-200 μm. Sample 1 had the largest number of cycles and smallest crack length. Sample 3 had the large pore at the notch root and sample 2 had significantly more porosity than sample 1.

Leuders et al. suggest that micron sized porosity mainly affects the fatigue strength and it is the residual stress and microstructure which greatly affects the fatigue crack growth. In this study sample one had minimal porosity and yet the largest crack growth rate. This suggests that the short fatigue crack growth seen may be mostly affected by residual stress or microstructure. The short crack growth variability is very dependent on porosity levels, size and location in terms of initiation (sample 3) and local elastoplastic behavior (sample 2 and 3).

Edwards et al. had varied FCG behavior and this can be shown to be likely due to the LOF defects similar to those seen in sample 3 [5]. The worst performing sample in that study had the loading

applied parallel to the build direction which resulted in the largest area of the defects being 'pulled' apart, this was detrimental to the crack initiation phase and subsequent growth. In sample 3 the fatigue loading was applied parallel to the largest area of the LOF defects, which may explain the slower FCG than was expected from this non optimized build condition, the crack did initiate at the large porosity defect. As both samples 2 and 3 were trial build condition with a large number of defects we expect to see some local elastoplastic behavior and toughening of the material which would also contribute to lower short FCG rates reported in this study.

8. ENERGY DISPERSIVE DIFFRACTION EXPERIMENTAL METHOD

8.1 Background and Overview

In-situ, axial loaded Energy Dispersive Diffraction experiments were conducted at the Argonne National Laboratory, Advanced Photon Source (APS), beamline 6-BM between July 30thth and August 5th, 2018. A series of EDD scans were taken with intervals of cyclic loading and tomography scans on a single sample, (sample 1). In total 3 loaded and 1 unloaded EDD scan, 1 far field strain EDD scan and 3 tomography scans were taken. The aim of this experiment was to capture strain related data for a region of interest which included the propagating crack front and any bulk material defects whilst under a constant load. Of interest was to see if this characterization method could be applied to such small regions of interest, if all six strain components could be computed and whether or not any new information can be gathered to help explain the short crack growth properties of AM Ti-6Al-4V.

8.2 In-Situ Loading and Sample Mounting

In order to conduct in-situ loading for the purposes of taking EDD scans under load or for the interrupted fatigue cycling, the same load frame and basic setup used for tomography scans, described in Section 4, was utilized. The main difference from the previous experimental setup is the control software. Prior to this beam time, the load frame had successfully been connected to the native APS control software, EPICS, this greatly simplifies and de-risks the setup with no need for the previously used CME2 software, python script or generic laptop.

The sample mounting system and method was unchanged from the previous experiment. For the static loading the drive motor was controlled via the APS GUI in the same way the rotational stage drive motors are controlled, real time force readout in Newtons was also available. For cycling through EPICS a simple macro is used to initiate parameters and conduct cycling. As the time constraint was less for this experiment the cycling was conducted at 0.5 Hz to ensure no slipping between scans (critical), cycle parameters are recorded in Table 3.4. Figure 8.1 shows the portable load frame mounted to the 6-BM stage.

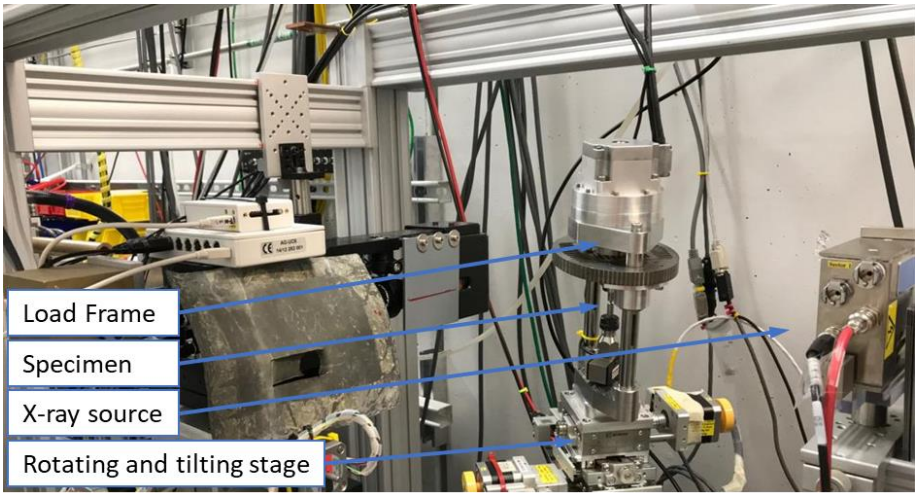

Figure 8.1. Experimental setup used for EDD at 6-BM, APS.

8.3 Region of Interest

Considerable thought went into the selection of the region of interest as there was time constraints, crack growth propagation lengths, grid size, beam spot size and overall data resolution to consider. Ultimately a three dimensional grid was chosen, as depicted in Figure 8.2, of note is the elongated gauge volume length in the beam direction (inherent to EDD experiments) and the 5 μm overlap used for each grid location. The total grid dimensions are 6 x 24 individual grid locations resulting in a 155 x 630 μm region of interest when accounting for the 5 μm overlap. The grid coordinate system is shown as aligned with the lab system with the gauge volume fixed in the beam direction. The sample was then rotated through the fixed gauge volume with nine unique configurations as discussed in detail below.

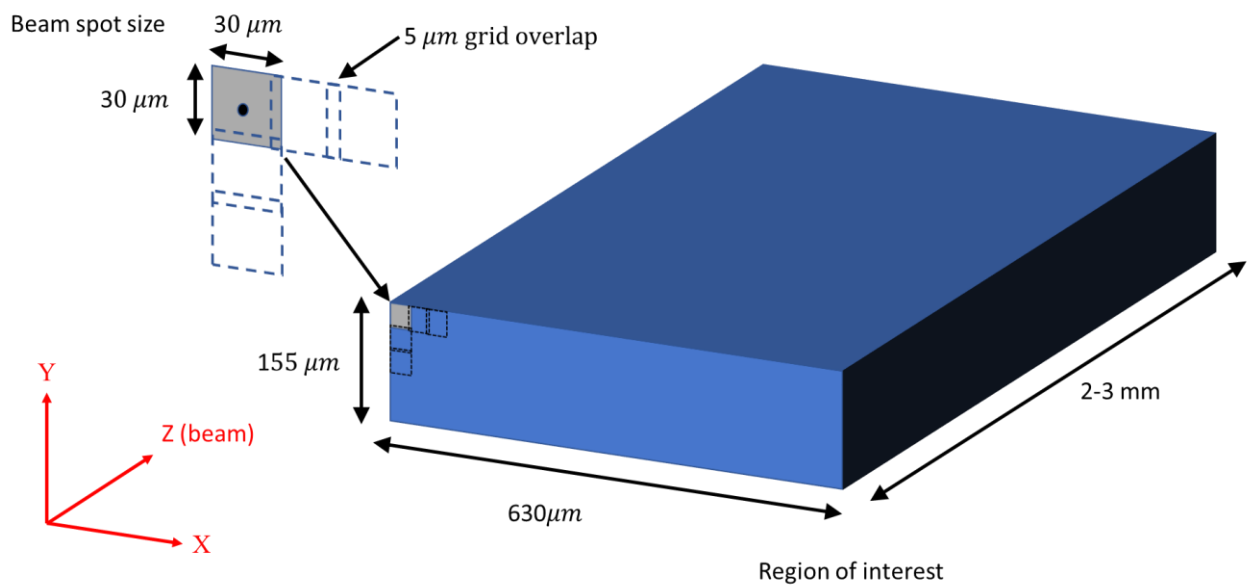

Figure 8.2. EDD grid on region of interest only (sample not shown), showing beam spot size of 30 x 30 μm, with a 5 μm overlap. The total number of grid locations was 6 x 24 which resulted in a 155 x 630 μm region of interest. To note, the elongated (2-3 mm) gauge volume length in the beam direction. Coordinate system is the fixed lab system.

The chosen grid was required to be located on the 1.5 x 1.5 mm gauge volume in order to see the crack front propagating into the region of interest. Three coordinate systems, two fixed to the sample and one fixed to the lab are also required. Figure 8.3 shows the coordinate systems and region of interest overlaid on the sample gauge volume.

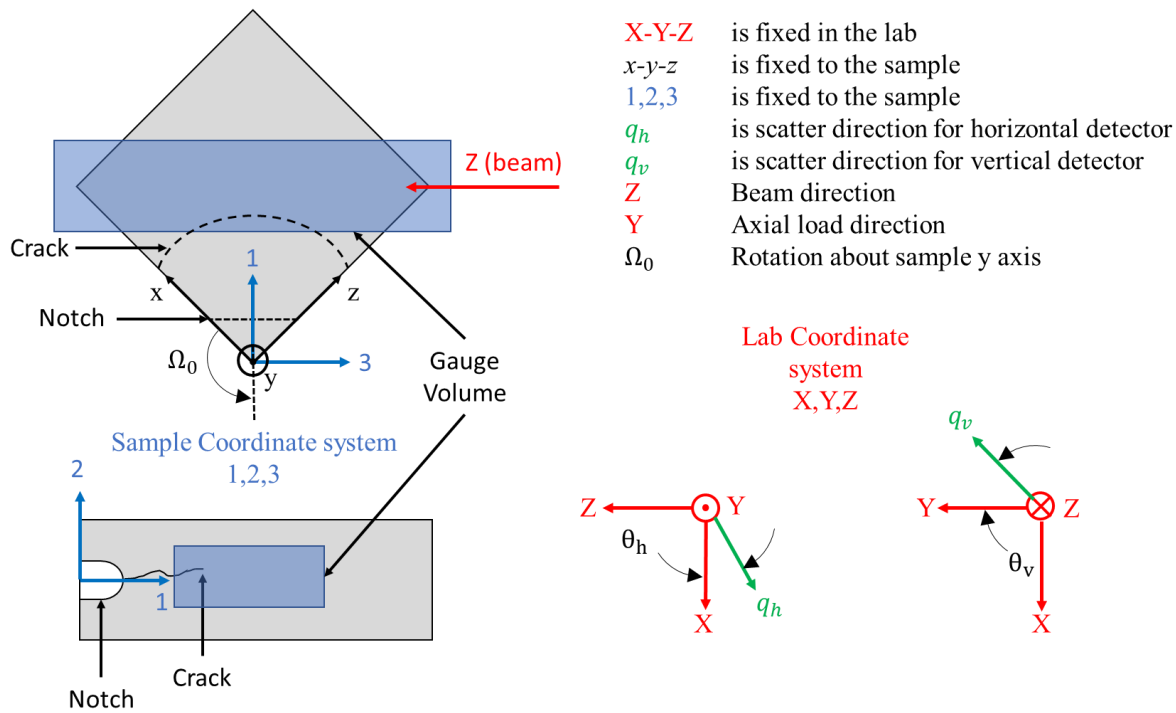

Figure 8.3. Chosen region of interest overlaid on a schematic of the sample, showing interaction with propagating crack front. Three coordinate systems, two fixed to the sample and one fixed to the lab are also depicted.

8.4 Beam Settings

The EDD beam settings were primarily the 30 x 30 μm x 2-3 mm beam spot size and gauge length, 5 μm overlap and the 50 sec exposure time required to gather sufficient data per grid point. The experimentally obtained lattice strains that are obtained for each grid point are defined by the average of the strains over the entire beam spot size (including in the elongated beam direction). The APS 6-BM beam line setup, as configured for EDD experiments uses a polychromatic beam provided via bending magnets. The beam is processed through three slits and one filter in order to harden the beam. Two germanium detectors, of horizontal and vertical orientation, with scattering angles q_h and q_v are placed at angles of $2\theta_h = 4.75°$ and $2\theta_v = 4.75°$ to the Y and X lab coordinated system axes, respectively.

8.1 Strain Measurement Experimental Method

A series of tomography scans were taken, the first was used to fix the location of the crack front, the resolution for all scans was 1.172 μm. After the initial tomography scan the grid was placed with approximately 50 μm of crack length protruding into the region of interest, parallel to the 630 μm length. The crack front was centered in the region of interest along the 155 μm length, this position allowed for up to 580 μm of crack growth and ≈75 μm of crack deflection.

After each EDD scan, fatigue cycles were conducted at 825 N, the same load as pre-cracking and the in-situ FCG experiment. Cycle blocks were kept to 200 – 1000 cycles, and the raw radiographs checked for crack growth (in case of any abnormally large crack growth) once deemed as a sufficient level of growth an EDD scan was initiated. The goal of the experiment was to achieve total crack growth over the three EDD scans of 100 – 200 μm. Figure 8.4 shows the crack evolution into the region of interest, through the three load steps, total crack growth was approximately 150 μm and a total of 2000 cycles were added between load steps.

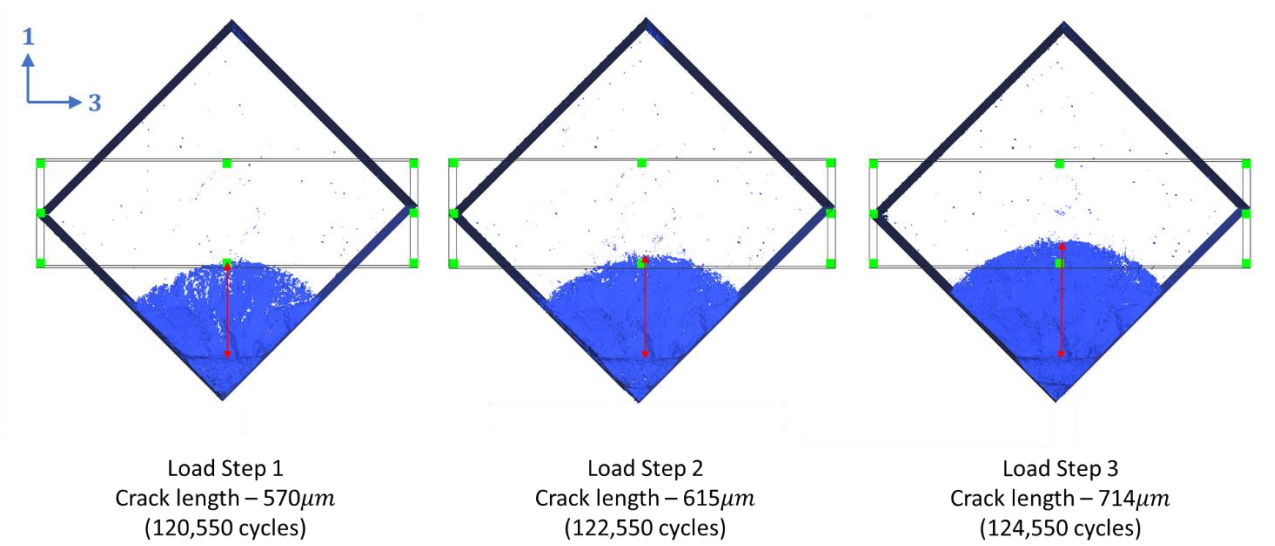

Figure 8.4. FCG propagation into the region of interest used for EDD experiment. Total fatigue cycles between each load step is 2000 cycles. Crack growth was approximately 150 μm total.

Each of the four full region of interest EDD scans took approximately 18 hours, estimated by 144 grid locations for nine unique rotations and 50 s per location, assuming no beam down time. The EDD scans were automated through a series of rotations and grid steps, three were taken with a

constant load of 825 N and one unloaded. As per Section 2.3.2, the EDD strain measurement principle requires an estimate for the strain free lattice parameter, d_o. For this experiment an estimate for d_o was measured by taking an EDD line scan at a sufficient distance from the cracked gauge volume. Figure 8.5 show the results of the line scan, counts and inter-planar spacing (Angstroms) which are plotted corresponding to the third α peak, a normal distribution was fitted and the mean result of 2.22598 Å used for an estimate of d_o.

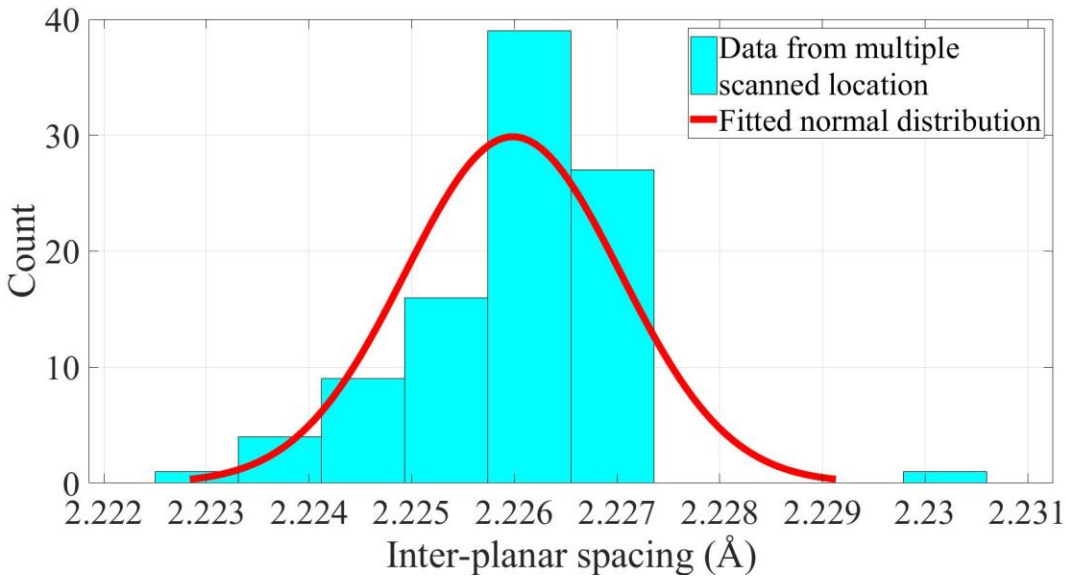

Figure 8.5. Results from an unloaded EDD line scan far from the gauge volume, showing inter-planar spacing corresponding to the third α peak. Fitted with a normal distribution the mean value of 2.22598 Å is used for the strain free lattice parameter estimate.

8.2 Strain Measurement Calculations

Previous work by Bandyopadhyay et al. included conducting an APS 6-BM EDD experiment on Linear Friction Welding (LFW) of titanium (covered in section 2, literature review) [77]. The author was able to successfully compute 5 components of the elastic strain tensor from EDD line scans, using a series of rotations giving seven unique configurations, five from Ω and two from χ [77]. A goal for this work was to obtain all six strain components, via an improvement in measurement techniques suggested by the authors. Figure 8.6 shows the orientation of the rotations with respect to the lab coordinate system and the sample, Ω is the sample rotation around the Y axis and χ is the rotation about the rotated Z axis (Z').

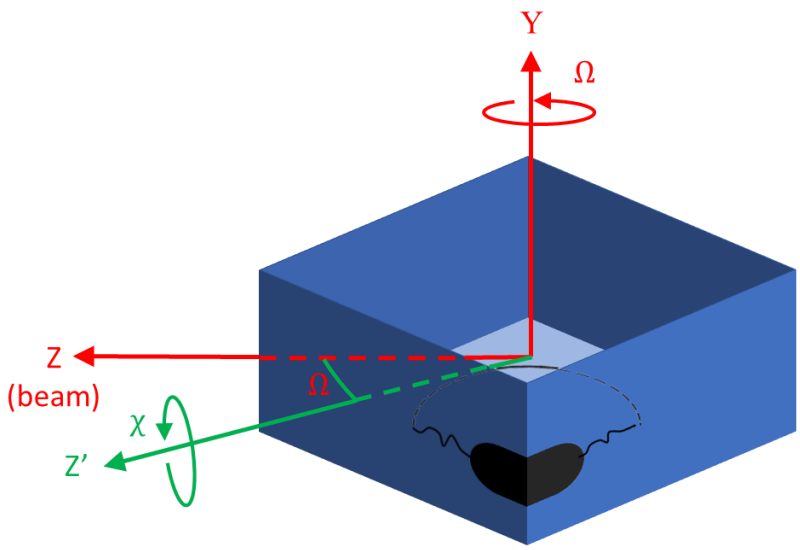

Figure 8.6. Sample rotation coordinate system used during EDD experiment.

The rotations used for this work are given in Figure 8.7, the Ω was set to -10°, 0° and 10° with the χ rotated through -8°, 0° and 8° for each Ω. Therefore, this work differs from the previous by having nine unique configurations.

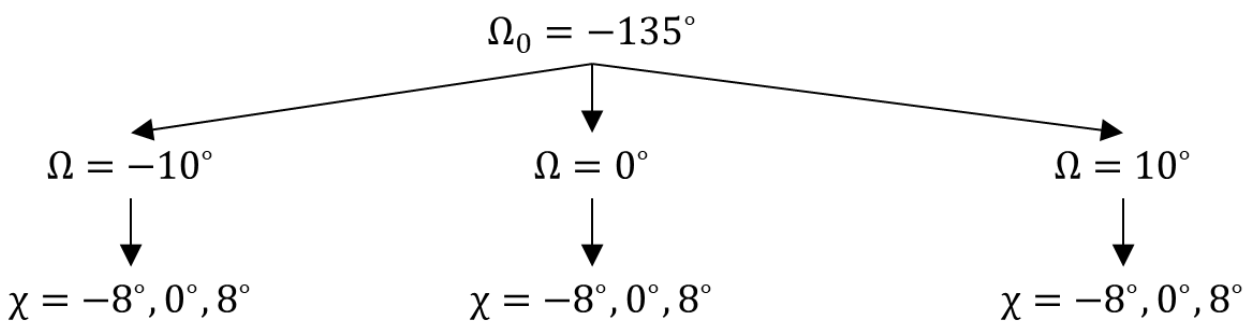

Figure 8.7. Rotation angles used during EDD sample, three Ω angles with three χ angles for each Ω were used for a total of nine unique configurations.

8.3 Strain Measurement Results

Post processing of the EDD experimental data involves obtaining the lattice strains via a peak fitting method and then calculating the six strain components using the lattice strains. An example of a diffraction pattern obtained is given in Figure 8.8, with a peak fit via the Pseudo-Voight peak fit function in MATLAB. The material exhibited highly textured characteristics with only the third

α peak being consistently present throughout the region of interest, significant noise was also present. No β phase peaks were detected and this was in-line with the expected microstructure of elongated grains, and primarily martensitic α' phase [11], [48], [64].

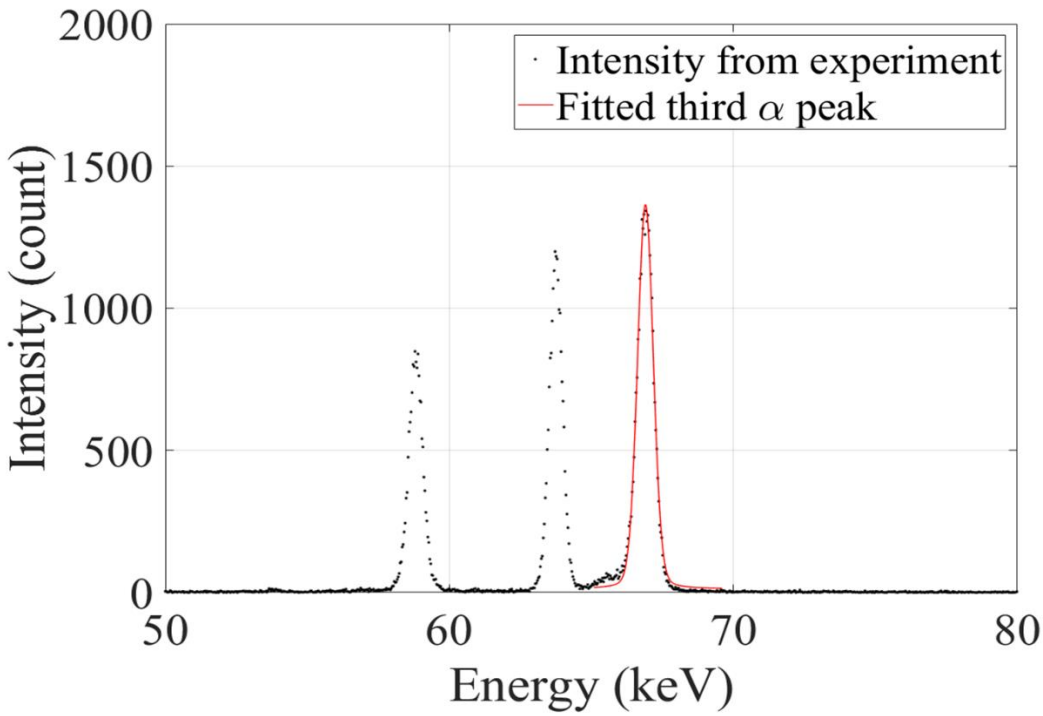

Figure 8.8. Example of a diffraction pattern obtained, peak fit via MATLAB Pseudo-Voight function shown in red.

From the peak fits the obtained energies, E_h^{hkl} and E_v^{hkl} are combined with the experimentally estimated strain free lattice parameter, d_0^{hkl}, planks constant, h, velocity of light, c, and detector take of angles, θ_h and θ_v. These values are used to compute the lattice strains, ε_{q_h} and ε_{q_v}, Equations 8.1 and 8.2, states these relationships.

$$\varepsilon_{q_h} = \frac{E_h^{hkl} - \frac{hc}{2d_0^{hkl}\sin\theta_h}}{\frac{hc}{2d_0^{hkl}\sin\theta_h}} \tag{8.1}$$

and

$$\varepsilon_{q_v} = \frac{E_v^{hkl} - \frac{hc}{2d_0^{hkl}\sin\theta_v}}{\frac{hc}{2d_0^{hkl}\sin\theta_v}} \tag{8.2}$$

Two equations for each combination of Ω and χ are computed using Equations 8.3, 8.4 and 8.5. ε_{q_h} is related to the horizontal detector, ε_{q_v} is related to the vertical detector, $\boldsymbol{\varepsilon}'$ refer to strain in the x-y-z coordinate system and $\mathbf{R}$ describes the rotation matrix relations. Equations 8.6 give the rotation matrices, $\mathbf{R}_{\boldsymbol{\Omega_0}}$, $\mathbf{R}_{\boldsymbol{\Omega}}$ and $\mathbf{R}_{\boldsymbol{\chi}}$.

$$\varepsilon_{q_h} = \boldsymbol{q_h}\mathbf{R}\boldsymbol{\varepsilon}'\mathbf{R}^{\mathbf{T}}\boldsymbol{q_h^{\mathbf{T}}} \tag{8.3}$$

$$\varepsilon_{q_v} = \boldsymbol{q_v}\mathbf{R}\boldsymbol{\varepsilon}'\mathbf{R}^{\mathbf{T}}\boldsymbol{q_v^{\mathbf{T}}} \tag{8.4}$$

and

$$\mathbf{R} = \mathbf{R}_{\boldsymbol{\Omega_0}}\mathbf{R}_{\boldsymbol{\Omega}}\mathbf{R}_{\boldsymbol{\chi}} \tag{8.5}$$

$$\mathbf{R}_{\boldsymbol{\Omega}} = \begin{bmatrix} \cos\Omega & 0 & -\sin\Omega \\ 0 & 1 & 0 \\ \sin\Omega & 0 & \cos\Omega \end{bmatrix}, \mathbf{R}_{\boldsymbol{\chi}} = \begin{bmatrix} \cos\chi & -\sin\chi & 0 \\ \sin\chi & \cos\chi & 0 \\ 0 & 0 & 1 \end{bmatrix}, \mathbf{R}_{\boldsymbol{\Omega_0}} = \begin{bmatrix} \cos\Omega_0 & 0 & -\sin\Omega_0 \\ 0 & 1 & 0 \\ \sin\Omega_0 & 0 & \cos\Omega_0 \end{bmatrix} \tag{8.6}$$

These pairs of equations (8.3 and 8.4) combined with the six unknown strain components form an over determined linear system of 18 equations and 6 unknowns, in the form of Equation 8.7, with x being the strain components, A the coefficients and b the lattice strains.

$$\mathbf{Ax} = \mathbf{b} \tag{8.7}$$

As per the method outlined by Bandyopadhyay et al. the system is solved using the MATLAB $lsqlin$ function, a least squares method where the L^2 norm of the residual is minimized [77].The $lsqlin$ method requires a set of bounds, the bounds used were plus and minus infinity, Equation 8.8 states the $lsqlin$ curve fitting problem, which minimizes $\mathbf{Ax} - \mathbf{b}$.

$$\min_{\mathbf{x}} \frac{1}{2}\|\mathbf{Ax} - \mathbf{b}\|^2 \tag{8.8}$$

8.4 Strain Measurement Accuracy

There is two sources of error within the reported strain values, one is the EDD experimental error of the order of 10^{-4} and the other is the error associated with the least squares solution of the strain tensor and is of the order of 10^{-6}. The accuracy of the obtained strain components are discussed by Bandyopadhyay et al., the authors compute the condition number ($\mathbf{A^T A}$) as a way to measure the accuracy of the inverse operator $(\mathbf{A^T A})^{-1}$ [77].As the condition number (Cond ($\mathbf{A}$)) increases the inverse operator becomes less reliable and the least squares minimization becomes ill defined. In this work Cond ($\mathbf{A}$) was plotted against the initial rotation Ω_0 , as shown in Figure 8.8, a large value for Cond ($\mathbf{A}$) occurs at the initial Ω_0 $(-135°)$ angle. As such the initial value was taken as $-136°$ for the following results which minimized the numerical error.

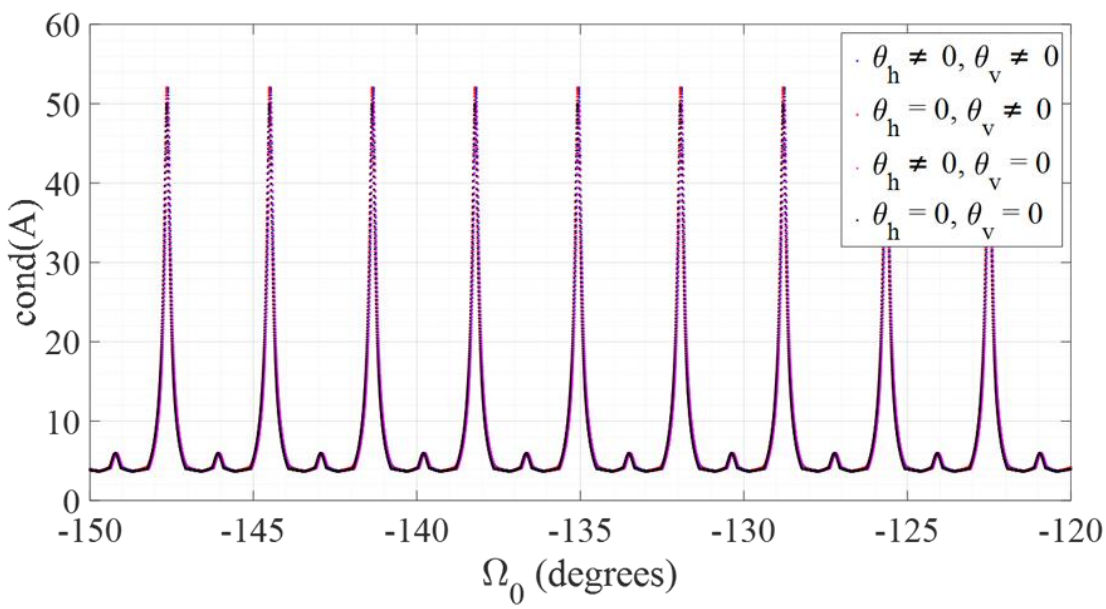

Figure 8.9. Figure 8.10. Showing the accuracy of the inversion process as sensitive to Ω_0 rotation [77].

9. ENERGY DISPERSIVE DIFFRACTION ANALYSIS AND RESULTS

9.1 Background and Overview

Sections 6 and 7 showed there was some correlation between the porosity and the FCG behaviors for the tested material. The results from the EDD experiment tended to agree by showing regions of higher strain that included pores within the elongated gauge volume. To show this the crack front and pores characterized by the tomography scans are compared to the strain component contour plots.

9.2 Estimate for Plastic Zone

Before the EDD experiment was conducted a first order approximation was calculated for the plastic zone size ahead of the crack tip, using the classical formula shown at Equation 9.1 which stems from the 1950s work of Irwin and Williams [103]. The plastic zone r_p, was estimated using the approximate stress intensity factor, K_{max}, for a penny-wise corner crack in a semi-infinite plate, Equation 9.2 [104]. It must be stressed that this is a simplified relation only used to ensure that the region of interest was larger enough to obtain the crack tip strain behaviors.

$$r_p = \alpha \left(\frac{K_{max}}{\sigma_{ys}}\right)^2 \tag{9.1}$$

$$K_{max} = 1.41\sigma_{max}\sqrt{a} \tag{9.2}$$

For Equation 9.2, σ_{max} is the maximum applied stress and a is the crack length. For Equation 9.1, σ_{ys} is taken as (900 Mpa) and as α varies from $\frac{1}{\pi}$ to $\frac{1}{3\pi}$ for plane stress at the surface to plane strain in the bulk, a range using these extreme was calculated. The resulting range is approximately 30 - 100 μm.

9.3 Results

The strain results are presented as a series of contour plots showing strain components. The loading direction for all results is in the 2 direction. Both axis's for the contour plots are in mm, with the x axis representing the 630 μm width and the y axis representing the 155 μm height of the scanned region of interest ((1, 2) plane). Figure 9.1 shows the region of interest tomography plot for load step 3, with all the porosity in the z (beam) direction collapsed on to the one plane, there are 22 visible porosity defects and the propagating crack in shown in blue.

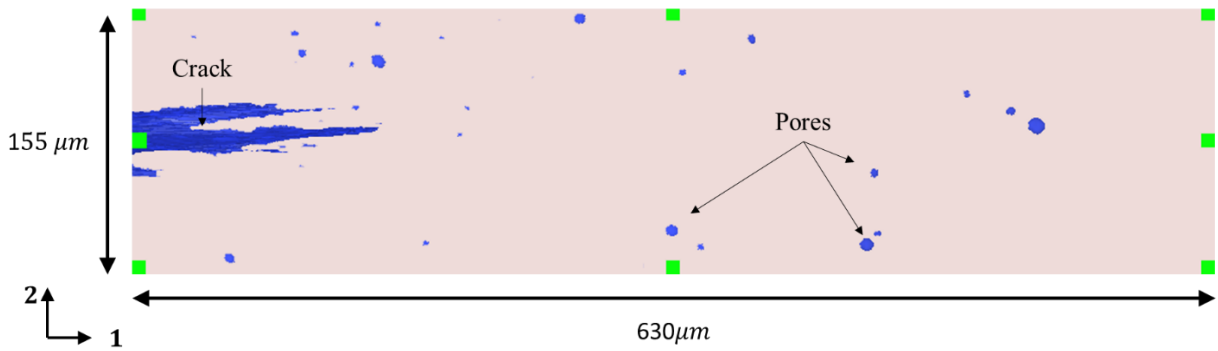

Figure 9.1. Load step 3 tomography scan of the region of interest, all porosity throughout the volume collapsed onto the (1, 2) plane, crack and pores shown in blue.

Figure 9.2 shows the strains calculated at load step 1, of interest is the ε_{22}, and a potential correlation between the strain hotspots and the identified pores in Figure 9.1. The remaining loads steps 2 and 3 are depicted in Figures 9.3 and 9.4, which show the evolution of the crack tip and potential porosity related strains, these are discussed below.

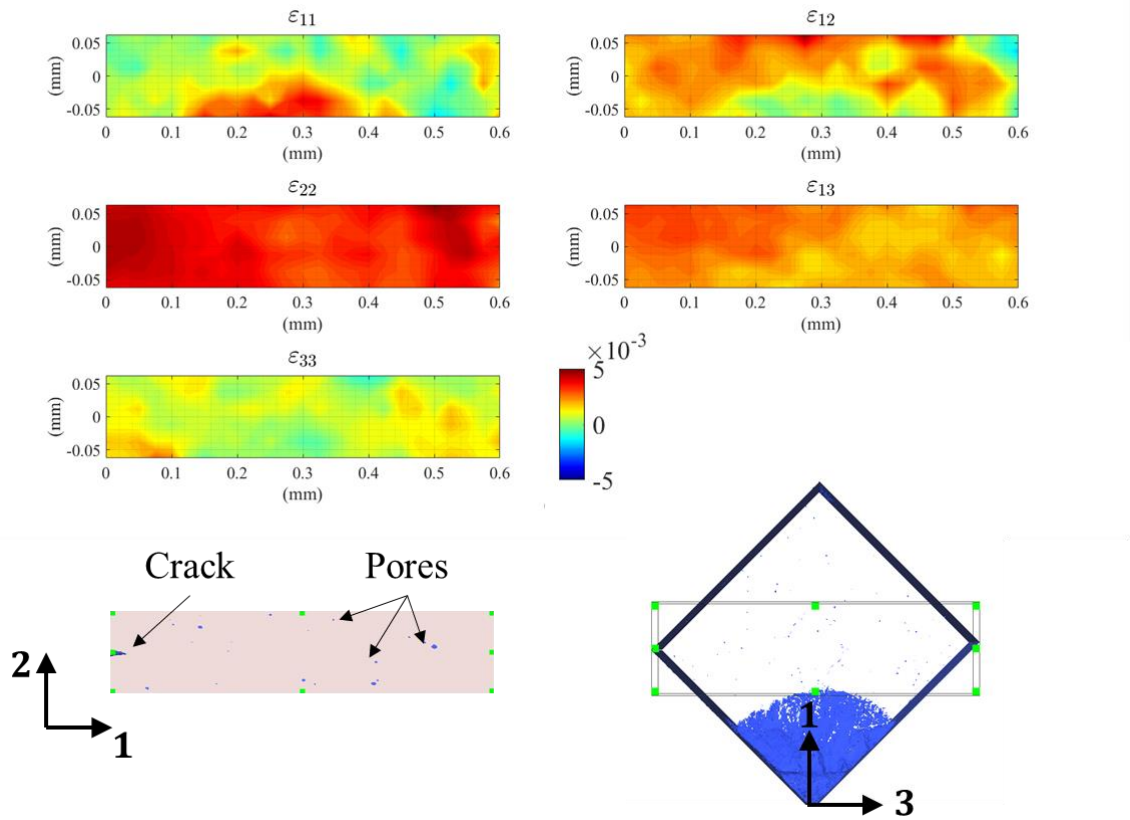

Figure 9.2. Sample 1, load step 1, EDD strain component contour plots (top) and region of interest tomography scans (bottom). Load at 825 N and total cycles 120,550.

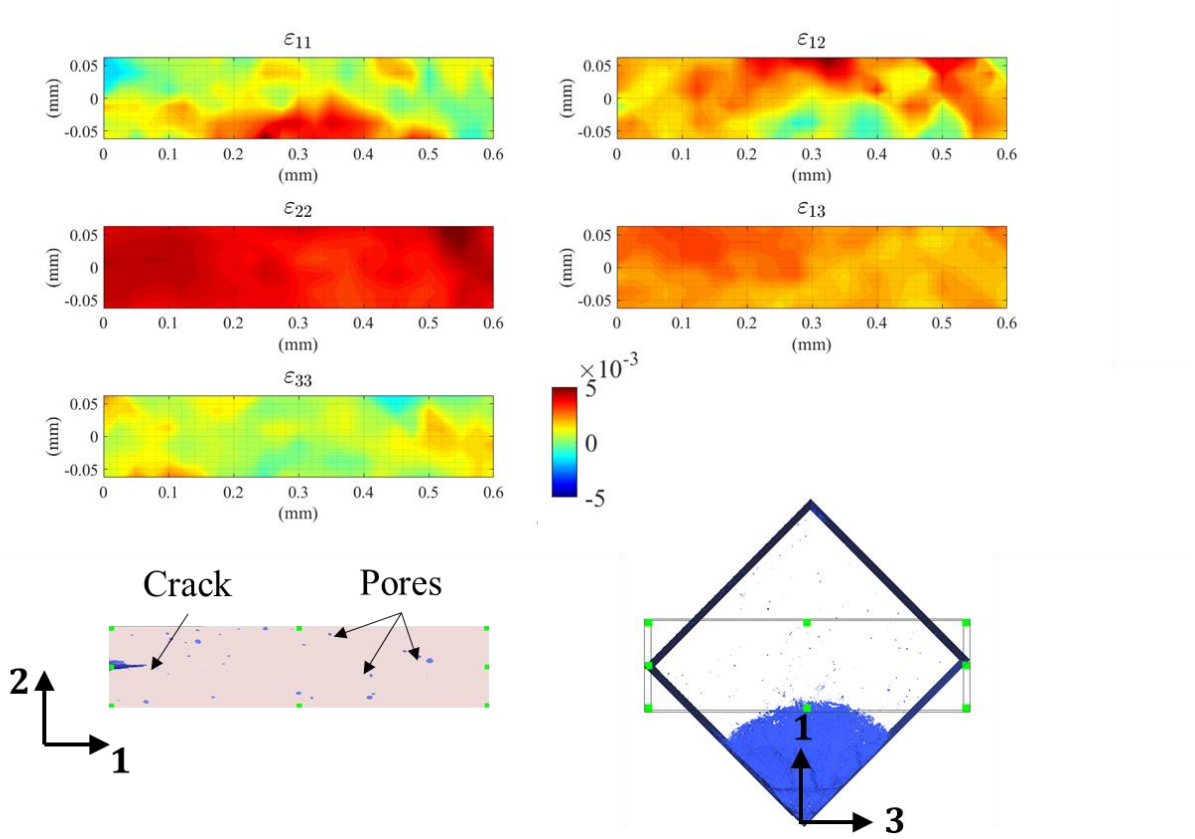

Figure 9.3. Sample 1, load step 2, EDD strain component contour plots (top) and region of interest tomography scans (bottom). Load at 825 N and total cycles 122,550.

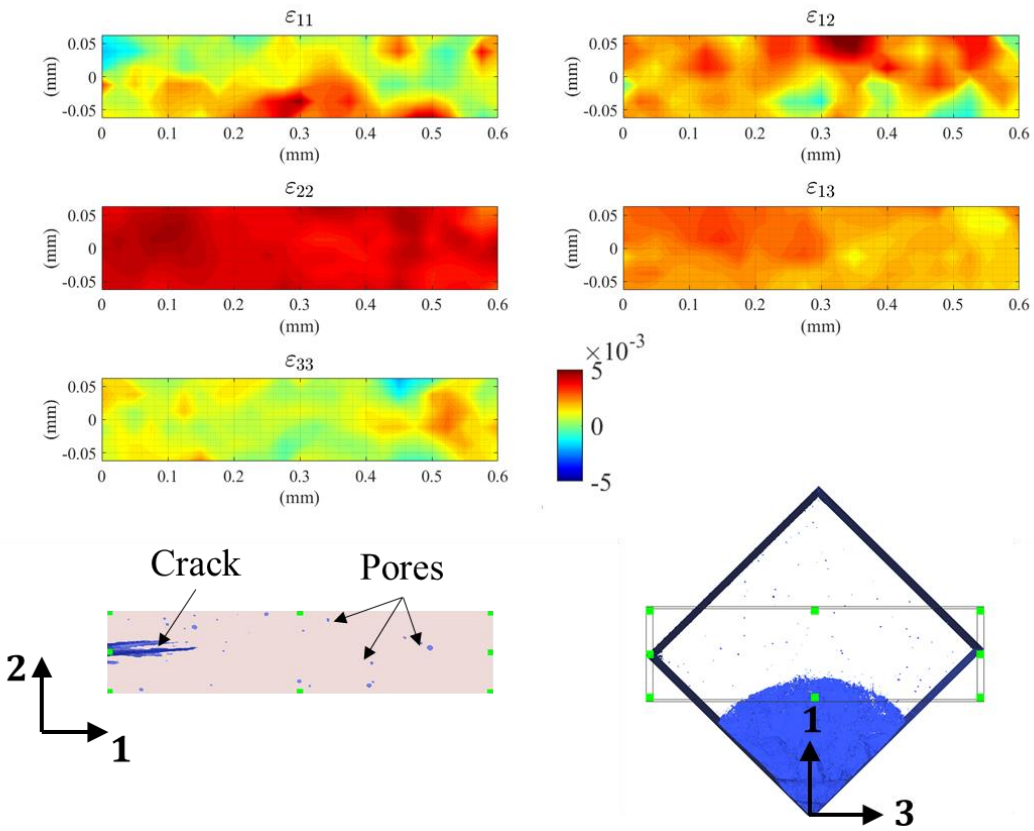

Figure 9.4. Sample 1, load step 3, EDD strain component contour plots (top) and region of interest tomography scans (bottom). Load at 825 N and total cycles 124,550.

Figure 9.5 shows the unloaded EDD scan (taken after load step 3), clearly the ε_{22} strain is at minimal values as well as the strain on the (1,2) plane in the 1 direction. The ε_{12} component still shows considerable hotspots on the same order as the stressed load step 3.

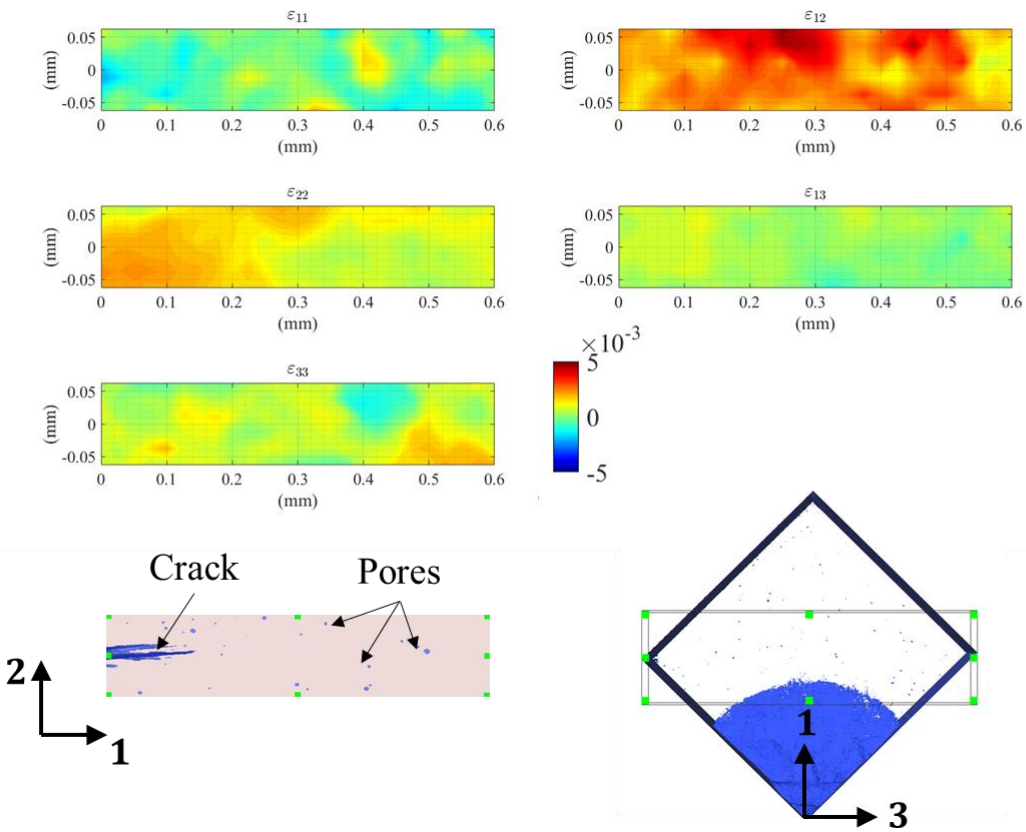

Figure 9.5. Sample 1, EDD strain component contour plots (top) and region of interest tomography scans (bottom). Load at 0 N and total cycles 124,550.

From the work of Gong et al. we can obtain an estimate for Young's Modulus for SLM AM Ti-6Al-4V, of $E = 110\ GPa$, and Poisson's ratio from literature as, $\nu = 0.31$ [105]. As the volume of the material that the elastic strains are measured over is reasonably large (2 mm in the beam direction), we can take the isotopic relations and use the Generalized Hooke's Law. The stress tensor, σ_{ij} and strain tensor, ε_{ij} are related by the stiffness matrix, C_{ijkl}, with only two independent coefficients, Equation 9.3. Equation 9.4 gives the index notation form of the isotropic stress-strain relationship with Lame's modulus, λ and the shear modulus, μ, given as Equations 9.5 and 9.6 respectively.

$$\sigma_{ij} = C_{ijkl}\varepsilon_{kl} \tag{9.3}$$

$$\sigma_{ij} = \lambda\varepsilon_{kk}\delta_{ij} + 2\mu\varepsilon_{ij} \tag{9.4}$$

$$\lambda = \frac{E\upsilon}{(1+\upsilon)(1-2\upsilon)} \tag{9.5}$$

$$\mu = \frac{E}{2(1+\upsilon)} \tag{9.6}$$

From the EDD elastic strain contour plots above we can see that the loaded ε_{22} component (in the loading direction) varies from $4.0 - 5.0\ e^{-3}$ within the region of the crack tip. The ε_{11} and ε_{33} on average from $0 - 1.0\ e^{-3}$ within the region of the crack tip. From this we can report an estimated stress range, $\Delta\sigma_{22}$ for the stresses seen in the region of the crack tip as, 335 – 830 MPa.

9.4 Discussion

The ε_{22} component evolution shows the crack tip affected zone moving into the region of interest as the crack propagates. The crack tip strain region in load step 1 is on the same order as the first order approximation of 30 - 100 μm. An exact measurement of these region is not possible from this data with any level of certainly, due to the low resolution and small region of interest. We can however, say that clearly the crack tip zone is moving into the region of interest and interacting with the anisotropic strain fields.

A number of pores show correlation with hotspots, although the three individual pores indicated in Figure 9.1 do not 'light up' until the sample is unloaded, potentially this could be an indication of the effects of residual stresses within the material. The issue with commenting on the individual pores is again the elongated gauge volume, the noise that exists within this region is possibly greater the strain around the individual porosity defects. Despite this the strain that is averaged through this region is showing as a hotspot and through the three load steps is increasing in magnitude. This anisotropic strain response could be related to the damage tolerance or fatigue life aspects for this material. In all load steps the highest strain values are seen not only around the propagating crack, but also within other regions of the material, this includes in the unloaded state with ε_{12} showing strain values as high as the crack tip in load step 3.

LEFM assumes the plastic zone around the crack tip is small compared to the size of the crack which is not applicable for short cracks. With a real world material such as this showing anisotropic strain response throughout the bulk material (potentially defect driven), and the short crack growth being related to the anisotropic microstructure this may explain some of the variation seen in Regime I crack growth, which in turn provides a variation in results for Regime II, Paris regime.

It is reasonable to assume that part of the reason for the lower crack growth rates in sample 2 and 3 is due to similar anisotropic strain behavior that would be exacerbated by the larger and less spherical porosity. If the pore size was larger we would expect a larger strain response, for elongated non spherical pores this would be even more pronounced. So although the crack is not physically growing (sample 3) the material likely has small regions which are highly strained, such as around the LOF defects.

This strain response makes lifing the material difficult with standard Damage Tolerance methods. It is likely a larger number of small undetectable flaws within the regions of porosity are present, once a critical number of cracks or accumulated plastic damage has been reached the crack propagation rate will increase or the material could fail immediately. Sample 2 and 3 both exhibit this behavior to some extent, low crack growth rates, followed by a large increase in growth rate and then failure, both samples failed at slightly lower cycles to sample 1.

10. CONCLUSIONS AND RECOMMENDATIONS

10.1 Conclusion

This research aimed to contribute to the knowledge of short crack growth and damage tolerance properties of SLM AM Ti-6Al-4V. The primary focus was on the crack behavior with respect to defects and anisotropies within the material. Very little research has been conducted on short crack growth in this material with the larger focus being on the long FCG, optimizing of AM process and production of more favorable microstructures. A secondary focus of this work was to consider whether EDD on very small samples was able to provide a useful real world understanding of the evolving strain fields around defects and the tip of a short crack. SLM AM Ti-6Al-4V samples with small (1.5 x 1.5 mm) notched cross sections were fatigued and studied using in-situ loading µXSCT and EDD methods. From this work crack path behavior, porosity and local lattice strain was studied.

From the results of the tomography scans we can see that sample 1 (optimized condition / vertical build / crack plane parallel to build layer) had a cleaner microstructure with significantly less porosity and a smooth fracture surface. Interestingly this sample had the fastest FCG rate of the three samples tested. There was three distinct cracks that initiated at the notch root and these remained separated with limited bridging until a crack length of approximately 300 μm, from which point the crack largely assumed a steady parallel crack until ultimately fast fracture. Although crack deflections were seen this largely did not impact the cracks characteristic length, similarly two spherical porosity defects were encountered by the crack tip, this was during steps in the crack as it moved back towards the main crack plane. Furthermore, two more pores were bypassed, one larger than 20 μm came within less than 10 μm from the propagating crack tip in the steady parallel phase and did not cause any deflection.

Sample 2 (trial condition / horizontal build / crack plane propagating through successive build layers) exhibited a significantly larger number and size of (mainly spherical) pores. Despite the poor build quality and excess defects this sample grew at a stagnated rate, from the tomography results we see that at the notch there is 5 distinct cracks, numerous micro cracks and a significant amount of crack deflection and bridging in the loading direction. Unlike sample 1 this behavior

largely subsided by the time the crack was 100 μm in length. This sample had the second lowest crack growth rate and the fracture surface was rough, showing signs of the material being pulled apart, this was also evident in the crack reconstructions.

Sample three (trial condition / horizontal build / crack plane propagating along the build layers at 90 degrees) was basically a defect driven crack initiation with a large 100 μm LOF defect seen adjacent to the notch. There were four distinct notch cracks, two from either side of the large pore, there was similar behavior to sample 2 with regards to fracture surface. Notably, due to the notch to build layer orientation a large step was evident running parallel to the LOF defects (and therefore perpendicular to the build direction). This sample exhibited significant LOF defects throughout the bulk of the material and had the lowest reported density (99.853%). Of note, is this sample actually had the lowest FCG rate of all three samples tested. From this study we can see that for short crack growth potentially defects are not the only or main driver for initiation and growth.

The difference in the fracture surfaces was very pronounced, a microindentation analysis was undertaken with the Vickers Hardness values indicating that the optimized build condition was a higher strength material. This variance in strength can explain some of the fracture surface behaviors.

Of the mechanisms considered for short FCG this study found that microstructural impacts for as built SLM Ti-6Al-4V have the largest impact. The conflicting long FCG for sample 1 equivalents was explored in terms of short FCG with this orientation shown to be the most damaging. There is evidence of build layer related crack defections and a smooth fracture surface, porosity (at the lowest volume fraction) was shown to most likely not impact the short FCG rate. Sample 2 and 3 were likely to have had some local elastoplastic behavior around defects, this would produce a toughening effect on the fracture properties. Sample 2 and 3 were shown to agree with the longer FCG rate, residual stress and anisotropic microstructure induced impacts.

The investigation into the use of EDD on a very small region of interest (smaller than the elongated gauge volume inherent to EDD) was successful. From this work all six elastic strain tensor components were reliably computed and the lattice strain in the loading direction was seen to evolve as the crack grew into the region of interest.

10.2 Recommendations

To confirm some of the suggestions within this work, namely the role of the microstructure and in particular the build layer influence, EBSD mapping of the sectioned samples is currently in progress. In terms of future work, a similar study using only an optimized build condition with various build directions could be tested to identify its role in short crack growth, including the pertinent mechanisms such as microstructurally or defect driven behavior, this may help to further understand the variance of fatigue life reported in literature for SLM AM Ti-6Al-4V.

If further investigations were to be considered a significant amount of care with regards to the build conditions, notch locations and sample selection would be required. In terms of the current research considerable work went in to characterizing the short FCG in material that was not representative of the quality that is currently able to be produced. Numerous studies have covered the optimization of build parameters and perfected the stated use of energy density as measure of quality. To correctly consider the build layer to notch orientations a careful approach to ensuring the orientations are tracked throughout the manufacturing process is required. This would then allow for a rigid test matrix of a larger sample size of representative materials and orientations. For the limited porosity seen in currently produced SLM Ti-6Al-4V a selection of a notch location that includes pores within the expected crack plane would be required to study any interactions. Finally, in order to correctly capture the microstructural impacts to short FCG in this material there needs to be a considered and rigorous approach to the characterization of the microstructure.

APPENDIX

μXSCT EXPERIMENT DATA

Sample 1					
Center Shift Value	Exp #	Load _Cycles (N)	Cycles	Drive Motor Counts	Load_Scan (N)
	1	N/a	0	0	N/a
	2	N/a	0	0	30
1275.50	3	N/a	0	0	21
1276.00	4	N/a	0	0	776
1280.00	5	830	50	-72000	825
1281.00	6	816	500	-72000	812
1282.00	7	828	1000	-72000	813
1282.00	8	806	1000	-73900	835
1282.00	9	817	1000	-73000	825
1282.00	10	825	1000	-74000	824
1282.50	11	816	1000	-74000	21
1282.50	12	N/a	N/a	N/a	820
1282.50	13	815	1000	-75000	825
1282.50	14	825	1000	-75500	828
1282.50	15	821	1000	-75500	822
1282.50	16	830	1000	-76000	826
1282.50	17	808	1000	-7000 -75000	829
1282.50	18	N/a	N/a	-7000 -76500	824
1282.50	19	819	1000	-8000 -77000	825
1282.50	20	819	1000	-8000 -77000	826
1282.50	21	823	1000	-6000 -78000	823
1282.50	22	821	2000	-6000 -78000	823
1282.50	23	821	1000	-6000 -78000	830
1282.50	24	816	1000	-6000 -78000	829
1282.50	25	820	1000	-7000 -79000	820
1282.50	26	821	1000	-7000 -79000	825
1282.50	27	800	1000	-8000 -79000	825
		total	20550		

Sample 2					
Center Shift Value	**Exp #**	**Load _Cycles (N)**	**Cycles**	**Drive Motor Counts**	**Load_Scan (N)**
1282.00	28	N/a	0	-73800	840
1283.00	29	780	100	-73800	835
1284.00	30	800	500	-82000	812
1284.50	31	810	1000	-83500	825
1285.00	32	830	1000	-86500	828
1285.00	33	830	1000	-87500	828
1285.00	34	830	1000	-88700	830
1285.50	35	829	1000	-89000	831
1286.00	36	821	1000	-89000	829
1286.00	37	830	1000	-90000	820
1286.00	38	831	1000	-90500	820
1286.00	39	825	1000	-90500	831
1286.00	40	818	1000	-91000	823
1286.00	41	825	1000	-91500	825
1286.00	42	822	1000	-92000	827
1286.00	43	817	1000	-92000	825
1286.00	44	830	2000	-93000	824
1286.00	45	824	2000	-93000	820
1286.00	46	819	1000	-93500	825
1286.00	47	830	1000	-94500	825
1286.00	48	828	1000	-94500	819
1286.00	49	817	2000	-95500	824
1286.00	50	825	2000	-95500 -8000	816
1286.00	51	813	0		
1286.00	52	818	2000	-98000 -11000	824
1286.00	53	829	2000	-99000 -11000	836
1286.00	54	840	1000	-99000 -11001	828
1286.00	55	830	1000	-99000 -11002	813
1286.00	56	833	1000	-99500 -11003	821
1286.00	57	830	1000	-99700 -11004	826
		total	32600		

Sample 3					
Center Value	**Exp #**	**Load _Cycles (N)**	**Cycles**	**Counts**	**Load_Scan (N)**
1280.00	58	N/a	0	-88500	831
1281.50	59	780	50	-88500	821
1281.50	60	825	200	-93000	815
1282.00	61	828	200	-95500	833
1282.00	62	817	200	-95700	825
1283.00	63	820	500	-97000	826
1283.00	64	831	1000	-98000	825
1284.00	65	834	1000	-99000	829
1284.00	66	818	1000	-98500	825
1284.00	67	825	2000	-99000	825
1284.50	68	819	2000	-99000	828
1284.50	69	825	1000	-100000	808
1284.50	70	831	2000	-101000	835
1284.50	71	852	2000	-101000	845
1284.50	72	811	2000	-100000	778
1284.50	73	787	2000	-101000	793
1284.50	74	843	2000	-103000	840
1284.50	75	826	2000	-103000	847
1284.50	76		2000	-102000	823
1284.50	77	821	2000	-104000	829
1278.00	78	825	4000	-104000	825
1280.00	79	825	1000	-105000	837
		total	30150		

REFERENCES

[1] D. Agius, K. Kourousis, and C. Wallbrink, "A Review of the As-Built SLM Ti-6Al-4V Mechanical Properties towards Achieving Fatigue Resistant Designs," *Metals (Basel).*, vol. 8, no. 1, p. 75, 2018.

[2] S. Leuders *et al.*, "On the mechanical behaviour of titanium alloy TiAl6V4 manufactured by selective laser melting: Fatigue resistance and crack growth performance," *Int. J. Fatigue*, vol. 48, pp. 300–307, 2013.

[3] V. Cain, L. Thijs, J. Van Humbeeck, B. Van Hooreweder, and R. Knutsen, "Crack propagation and fracture toughness of Ti6Al4V alloy produced by selective laser melting," *Addit. Manuf.*, vol. 5, pp. 68–76, 2015.

[4] T. Vilaro, C. Colin, and J. D. Bartout, "As-fabricated and heat-treated microstructures of the Ti-6Al-4V alloy processed by selective laser melting," *Metall. Mater. Trans. A Phys. Metall. Mater. Sci.*, vol. 42, no. 10, pp. 3190–3199, 2011.

[5] P. Edwards and M. Ramulu, "Effect of build direction on the fracture toughness and fatigue crack growth in selective laser melted Ti-6Al-4-‰V," *Fatigue Fract. Eng. Mater. Struct.*, vol. 38, no. 10, pp. 1228–1236, 2015.

[6] J.-P. Kruth, M. Badrossamay, E. Yasa, J. Deckers, L. Thijs, and J. Van Humbeeck, "Part and material properties in selective laser melting of metals," *16th Int. Symp. Electromachining*, no. January 2015, pp. 1–12, 2010.

[7] Y. Huang and M. C. L. March, "Frontiers of Additive Manufacturing Research and Education," *NSF Work. Rep.*, no. March, pp. 1–26, 2014.

[8] W. Gao *et al.*, "The status, challenges, and future of additive manufacturing in engineering," *CAD Comput. Aided Des.*, vol. 69, pp. 65–89, 2015.

[9] E. C. Santos, M. Shiomi, K. Osakada, and T. Laoui, "Rapid manufacturing of metal components by laser forming," *Int. J. Mach. Tools Manuf.*, vol. 46, no. 12–13, pp. 1459–1468, 2006.

[10] C. Lindemann, U. Jahnke, M. Moi, and R. Koch, "Analyzing product lifecycle costs for a better understanding of cost drivers in additive manufacturing," *Int. Solid Free. Fabr. Symp.*, vol. 23, pp. 177–188, 2012.

[11] L. E. Murr *et al.*, "Metal Fabrication by Additive Manufacturing Using Laser and Electron Beam Melting Technologies," *J. Mater. Sci. Technol.*, vol. 28, no. 1, pp. 1–14, 2012.

[12] R. Jones, "Fatigue crack growth and damage tolerance," *Fatigue Fract. Eng. Mater. Struct.*, vol. 37, no. 5, pp. 463–483, 2014.

[13] C. F. Tiffany, J. P. Gallagher, and C. A. Babish, "Threats To Aircraft Structural Safety , Including a Compendium of Selected Structural Accidents / Incidents," *Security*, 2010.

[14] N. Pugno, M. Ciavarella, P. Cornetti, and A. Carpinteri, "A generalized Paris' law for fatigue crack growth," *J. Mech. Phys. Solids*, vol. 54, no. 7, pp. 1333–1349, 2006.

[15] A. . Griffith, "The Phenomena of rupture and flow in liquids," *R. Soc.*, vol. 221, pp. 163–198, 1920.

[16] R. Society, "Surface Energy and Surface Tension in Solids and Liquids Author (s): E . Orowan Source : Proceedings of the Royal Society of London . Series A , Mathematical and Physical Published by : Royal Society Stable URL : https://www.jstor.org/stable/77634," vol. 316, no. 1527, pp. 473–491, 2018.

[17] R. J. Allen, G. S. Booth, and T. Jutla, "A review of fatigue crack growth characterization by linear elastic fracture mechanics (LEFM). Part I—principles and methods of data generation," *Fatigue Fract. Eng. Mater. Struct.*, vol. 11, no. I, pp. 45–69, 1988.

[18] J. Schijve, "Four lectures on fatigue crack growth," *Eng. Fract. Mech.*, vol. 11, no. 1, pp. 167–168, 1979.

[19] K. J. MILLER, "the Short Crack Problem," *Fatigue Fract. Eng. Mater. Struct.*, vol. 5, no. 3, pp. 223–232, 1982.

[20] S. Suresh and R. O. Ritchie, "Propagation of short fatigue cracks," *Int. Met. Rev.*, vol. 29, no. 1, pp. 445–475, 1984.

[21] S. Pearson, "Initiation of fatigue cracks in commercial aluminium alloys and the subsequent propagation of very short cracks," *Eng. Fract. Mech.*, vol. 7, no. 2, 1975.

[22] R. J. Donahue, H. M. I. Clark, P. Atanmo, R. Kumble, and A. J. McEvily, "Crack opening displacement and the rate of fatigue crack growth," *Int. J. Fract. Mech.*, vol. 8, no. 2, pp. 209–219, 1972.

[23] R. O. Ritchie and J. Lankford, "Small fatigue cracks: A statement of the problem and potential solutions," *Mater. Sci. Eng.*, vol. 84, no. C, pp. 11–16, 1986.

[24] D. A. Lados, D. Apelian, P. C. Paris, and J. K. Donald, "Closure mechanisms in Al-Si-Mg cast alloys and long-crack to small-crack corrections," *Int. J. Fatigue*, vol. 27, no. 10–12, pp. 1463–1472, 2005.

[25] P. J. E. Forsyth, "A two stage process of fatigue crack growth," in *Proceedings of the Crack Propagation Symposium*, 1961, vol. 1, pp. 76–94.

[26] I. X. C. Boettner, "CRACK METALS It has been proposed that growth of a fatigue crack proceeds by a two stage process .(1-3j The first stage is considered to be an extension of the intrusion process which initiated the crack . Hence growth in this stage takes place by a cycl."

[27] G. R. Yoder, L. A. Cooley, and T. W. Crooker, "Quantitative analysis of microstructural effects on fatigue crack growth in widmanstätten Ti-6A1-4V and Ti-8Al-1Mo-1V," *Eng. Fract. Mech.*, vol. 11, no. 4, pp. 805–816, 1979.

[28] A. Navarro and E. R. d. L. Rios, "a Model for Short Fatigue Crack Propagation With an Interpretation of the Short-Long Crack Transition," *Fatigue Fract. Eng. Mater. Struct.*, vol. 10, no. 2, pp. 169–186, 1987.

[29] J. C. Newman, "The merging of fatigue and fracture mechanics concepts: A historical perspective," *Prog. Aerosp. Sci.*, vol. 34, no. 5–6, pp. 347–390, 1998.

[30] J. C. Newman, E. P. Phillips, and M. H. Swain, "Fatigue-life prediction methodology using small-crack theory," *Int. J. Fatigue*, vol. 21, no. 2, pp. 109–119, 1999.

[31] J. Lankford, "T h e g r o w t h of small fatigue cracks in," 1975.

[32] A. Rovinelli, M. D. Sangid, H. Proudhon, and W. Ludwig, "Using machine learning and a data-driven approach to identify the small fatigue crack driving force in polycrystalline materials," *npj Comput. Mater.*, vol. 4, no. 1, pp. 1–10, 2018.

[33] C. Q. Bowles and J. Schijve, "The role of inclusions in fatigue crack initiation in an aluminum alloy," *Int. J. Fract.*, vol. 9, no. 2, pp. 171–179, 1973.

[34] W. L. Morris, O. Buck, and H. L. Marcus, "Fatigue crack initiation and early propagation in Al 2219-T851," *Metall. Trans. A*, vol. 7, no. 7, pp. 1161–1165, 1976.

[35] C. Y. Kung and M. E. Fine, "Fatigue Crack initiation and microcrack growth in 2024-T4 and 2124-T4 aluminum alloys," *Metall. Trans. A*, vol. 10, no. 5, pp. 603–610, May 1979.

[36] D. Naragani *et al.*, "Investigation of fatigue crack initiation from a non-metallic inclusion via high energy x-ray diffraction microscopy," *Acta Mater.*, vol. 137, pp. 71–84, 2017.

[37] W. Elber, "The Significance of Fatigue Crack Closure," *Damage Toler. Aircr. Struct.*, pp. 230-230–13, 2018.

[38] "Standard Test Method for Measurement of Fatigue Crack Growth Rates BT - Standard Test Method for Measurement of Fatigue Crack Growth Rates." .

[39] W. E. Frazier, "Metal additive manufacturing: A review," *J. Mater. Eng. Perform.*, vol. 23, no. 6, pp. 1917–1928, 2014.

[40] K. F. Walker, Q. Liu, and M. Brandt, "Evaluation of fatigue crack propagation behaviour in Ti-6Al-4V manufactured by selective laser melting," *International Journal of Fatigue*, vol. 104. pp. 302–308, 2017.

[41] V. Le, E. Pessard, F. Morel, F. Edy, and I. R. T. J. Verne, "Influence of porosity on the fatigue behaviour of additively fabricated TA6V alloys," *MATEC Web Conf.*, vol. 165, pp. 1–9, 2018.

[42] ASTM International, "F2792-12a - Standard Terminology for Additive Manufacturing Technologies," *Am. Soc. Test. Mater.*, pp. 10–12, 2013.

[43] Y. Chen, Chi Zhou, and Jingyuan Lao, "A layerless additive manufacturing process based on CNC accumulation," *Rapid Prototyp. J.*, vol. 17, no. 3, pp. 218–227, 2011.

[44] Y. Yan, "Design Methodology and Materials for Additive Manufacturing of Magnetic Components," 2017.

[45] J. P. Kruth, "Material Incress Manufacturing by Rapid Prototyping Techniques," *CIRP Ann. - Manuf. Technol.*, vol. 40, no. 2, pp. 603–614, 1991.

[46] E. Herderick, "Additive manufacturing of metals: A review," *Mater. Sci. Technol.*, no. MS, p. 1413, 2011.

[47] G. Kasperovich and J. Hausmann, "Improvement of fatigue resistance and ductility of TiAl6V4 processed by selective laser melting," *J. Mater. Process. Technol.*, vol. 220, pp. 202–214, 2015.

[48] L. Thijs, F. Verhaeghe, T. Craeghs, J. Van Humbeeck, and J. P. Kruth, "A study of the microstructural evolution during selective laser melting of Ti-6Al-4V," *Acta Mater.*, vol. 58, no. 9, pp. 3303–3312, 2010.

[49] Q. C. Liu, J. Elambasseril, S. J. Sun, M. Leary, M. Brandt, and P. K. Sharp, "The Effect of Manufacturing Defects on the Fatigue Behaviour of Ti-6Al-4V Specimens Fabricated Using Selective Laser Melting," *Adv. Mater. Res.*, vol. 891–892, pp. 1519–1524, 2014.

[50] H. Gong, K. Rafi, H. Gu, T. Starr, and B. Stucker, "Analysis of defect generation in Ti-6Al-4V parts made using powder bed fusion additive manufacturing processes," *Addit. Manuf.*, vol. 1, pp. 87–98, 2014.

[51] H. Gong, K. Rafi, T. Starr, and B. Stucker, "Generation An Detection Of Defects In Metallic Parts Fabricated By Selective Laser Melting And Electron Beam Melting And Their Effects On Mechanical Properties," *Solid Free. Fabr. Proc.*, no. December, pp. 424–439, 2013.

[52] W. E. King *et al.*, "Observation of keyhole-mode laser melting in laser powder-bed fusion additive manufacturing," *J. Mater. Process. Technol.*, vol. 214, no. 12, pp. 2915–2925, 2014.

[53] S. Leuders, S. Meiners, L. Wu, A. Taube, T. Tröster, and T. Niendorf, "Structural components manufactured by Selective Laser Melting and Investment Casting—Impact of the process route on the damage mechanism under cyclic loading," *J. Mater. Process. Technol.*, vol. 248, no. May, pp. 130–142, 2017.

[54] B. Van Hooreweder, D. Moens, R. Boonen, J.-P. Kruth, and P. Sas, "Analysis of Fracture Toughness and Crack Propagation of Ti6Al4V Produced by Selective Laser Melting," *Adv. Eng. Mater.*, vol. 14, no. 1-2, pp. 92–97, Nov. 2011.

[55] G. Kasperovich, J. Haubrich, J. Gussone, and G. Requena, "Correlation between porosity and processing parameters in TiAl6V4 produced by selective laser melting," *Mater. Des.*, vol. 105, pp. 160–170, 2016.

[56] T. A. Book and M. D. Sangid, "Strain localization in Ti-6Al-4V Widmanstätten microstructures produced by additive manufacturing," *Mater. Charact.*, vol. 122, pp. 104–112, 2016.

[57] M. Thöne and S. Leuders, "Influence of heat-treatment on Selective Laser Melting products – e.g. Ti6Al4V," *Sff*, no. June 2015, pp. 492–498, 2012.

[58] B. Vrancken, L. Thijs, J.-P. Kruth, and J. Van Humbeeck, "Heat treatment of Ti6Al4V produced by Selective Laser Melting: Microstructure and mechanical properties," *J. Alloys Compd.*, vol. 541, pp. 177–185, 2012.

[59] C. Qiu, N. J. E. Adkins, and M. M. Attallah, "Microstructure and tensile properties of selectively laser-melted and of HIPed laser-melted Ti-6Al-4V," *Mater. Sci. Eng. A*, vol. 578, pp. 230–239, 2013.

[60] F. Wang, S. Williams, P. Colegrove, and A. A. Antonysamy, "Microstructure and mechanical properties of wire and arc additive manufactured Ti-6Al-4V," *Metall. Mater. Trans. A Phys. Metall. Mater. Sci.*, vol. 44, no. 2, pp. 968–977, 2013.

[61] P. Li, D. H. Warner, A. Fatemi, and N. Phan, "Critical assessment of the fatigue performance of additively manufactured Ti-6Al-4V and perspective for future research," *Int. J. Fatigue*, vol. 85, pp. 130–143, 2016.

[62] C. Qiu, C. Panwisawas, M. Ward, H. C. Basoalto, J. W. Brooks, and M. M. Attallah, "On the role of melt flow into the surface structure and porosity development during selective laser melting," *Acta Mater.*, vol. 96, pp. 72–79, 2015.

[63] R. H. Morgan, A. J. Papworth, C. Sutcliffe, P. Fox, and W. O'Neill, "High density net shape components by direct laser re-melting of single-phase powders," *J. Mater. Sci.*, vol. 37, no. 15, pp. 3093–3100, 2002.

[64] Q. Liu, C. Wallbrink, and W. Hu, "Effect of Build Condition and Direction on Fatigue Crack Growth Rates of Selective Laser Melted Ti - 6Al - 4V Specimens," no. November, pp. 27–29, 2017.

[65] P. Mercelis and J. P. Kruth, "Residual stresses in selective laser sintering and selective laser melting," *Rapid Prototyp. J.*, vol. 12, no. 5, pp. 254–265, 2006.

[66] E. Maire and P. J. Withers, "Quantitative X-ray tomography," *Int. Mater. Rev.*, vol. 59, no. 1, pp. 1–43, 2014.

[67] S. Titarenko, V. Titarenko, A. Kyrieleis, and P. J. Withers, "A priori information in a regularized sinogram-based method for removing ring artefacts in tomography," *J. Synchrotron Radiat.*, vol. 17, no. 4, pp. 540–549, 2010.

[68] G. Davis, A. Evershed, J. Elliott, and D. Mills, "Quantitative x-ray microtomography with a conventional source," no. August, p. 78040I, 2010.

[69] A. Sakellariou, T. J. Sawkins, T. J. Senden, and A. Limaye, "X-ray tomography for mesoscale physics applications," *Phys. A Stat. Mech. its Appl.*, vol. 339, no. 1–2, pp. 152–158, 2004.

[70] A. C. Kak and M. Slaney, "Principles of Computerized Tomographic Imaging (Philadelphia, PA: SIAM)," 2001.

[71] A. Pyzalla *et al.*, "Simultaneous tomography and diffraction analysis of creep damage," *Science (80-.).*, vol. 308, no. 5718, pp. 92–95, 2005.

[72] N. S. Rossini, M. Dassisti, K. Y. Benyounis, and A. G. Olabi, "Methods of measuring residual stresses in components."

[73] A. Steuwer, J. R. Santisteban, M. Turski, P. J. Withers, and T. Buslaps, "High-resolution strain mapping in bulk samples using full-profile analysis of energy dispersive synchrotron X-ray diffraction data," *Nucl. Instruments Methods Phys. Res. Sect. B Beam Interact. with Mater. Atoms*, vol. 238, no. 1–4, pp. 200–204, 2005.

[74] P. J. Withers, "Residual stress and its role in failure," *Reports Prog. Phys.*, vol. 70, no. 12, pp. 2211–2264, 2007.

[75] C. Genzel, I. A. Denks, J. Gibmeier, M. Klaus, and G. Wagener, "The materials science synchrotron beamline EDDI for energy-dispersive diffraction analysis," *Nucl. Instruments Methods Phys. Res. Sect. A Accel. Spectrometers, Detect. Assoc. Equip.*, vol. 578, no. 1, pp. 23–33, 2007.

[76] P. J. Withers, H. K. D. H. Bhadeshia, P. J. Withers, and H. K. D. H. Bhadeshia, "Residual stress . Part 1 – Measurement techniques Residual stress Part 1 – Measurement techniques," vol. 0836, no. 2001, 2013.

[77] Ritwik Bandyopadhyay; John Rotella; Diwakar Naragani; Jun-Sang Park; Michael Eff; Michael Sangid;, "Residual strain analysis in linear friction welds of similar and dissimilar titanium alloys using energy dispersive x-ray diffraction," *Metall and Mat Trans A*, In Print, 2018.

[78] A. Alexander M. Korsunsky, B. * Steve P. Collins, d S. R. A. O. c Mark R. Daymond, and A. and K. E. Jamesa, "Fast residual stress mapping using energy-dispersive synchrotron X-ray diffraction on station 16.3 at the SRS," *J. Synchrotron Radiat.*, vol. 9, no. 2, pp. 77–81, 2002.

[79] M. Croft *et al.*, "Strain profiling of fatigue crack overload effects using energy dispersive X-ray diffraction," in *International Journal of Fatigue*, 2005, vol. 27, no. 10–12, pp. 1408–1419.

[80] T. Fuß, M. Meixner, M. Klaus, and C. Genzel, "Residual Stress Analysis by Energy-Dispersive Synchrotron Diffraction: Concepts for High Resolution Depth Profiling in Real Space," *Mater. Sci. Forum*, vol. 768–769, pp. 44–51, 2013.

[81] V. Honkimäki and P. Suortti, "Energy-dispersive diffraction with synchrotron radiation and a germanium detector," *J. Synchrotron Radiat.*, vol. 14, no. 4, pp. 331–338, 2007.

[82] M. R. Daymond, M. A. M. Bourke, R. Von Dreele, B. Clausen, and T. Lorentzen, "Use of Rietveld refinement for Elastic Macro strain Determination & for Evaluation of Plastic strain History from Different Spectra," vol. 82, no. 4, 1998.

[83] A. Steuwer, M. Rahman, A. Shterenlikht, M. E. Fitzpatrick, L. Edwards, and P. J. Withers, "The evolution of crack-tip stresses during a fatigue overload event," *Acta Mater.*, vol. 58, no. 11, pp. 4039–4052, 2010.

[84] M. N. James, D. G. Hattingh, D. J. Huges, L. W. Wei, E. A. Patterson, and J. Q. Da Fonseca, "Synchrotron diffraction investigation of the distribution and influence of residual stresses in fatigue," *Fatigue Fract. Eng. Mater. Struct.*, vol. 27, pp. 609–622, 2004.

[85] I. Bhamji, M. Preuss, P. L. Threadgill, and A. C. Addison, "Solid state joining of metals by linear friction welding: a literature review," *Mater. Sci. Technol.*, vol. 27, no. 1, pp. 2–12, 2011.

[86] M. R. Daymond and N. W. Bonner, "Measurement of strain in a titanium linear friction weld by neutron diffraction," vol. 325, pp. 130–137, 2003.

[87] S. L. M. Solutions, "SLM Material data-SLM 250 HL," *available www. slm-solutions. com*, 2012.

[88] W. D. Pilkey and D. F. Pilkey, *Peterson's stress concentration factors*. John Wiley & Sons, 2008.

[89] S. T. Carter, J. Rotella, R. F. Agyei, X. Xiao, and M. D. Sangid, "Measuring fatigue crack deflections via cracking of constituent particles in AA7050 via in situ x-ray synchrotron-based micro-tomography," *Int. J. Fatigue*, vol. 116, no. May, pp. 490–504, 2018.

[90] J. C. Newman *et al.*, "Crack-Closure Behavior of 7050 Aluminum Alloy near Threshold Conditions for Wide Range in Load Ratios and Constant Kmax Tests," *J. ASTM Int.*, vol. 7, no. 4, p. 102490, 2010.

[91] Department of Defense, *Handbook Metallic Materials and Elements for Aerospace Vehicles Structures*, no. January. 2003.

[92] C. Controls, "CME 2 User Guide," no. January, 2014.

[93] D. Gürsoy, F. De Carlo, X. Xiao, and C. Jacobsen, "TomoPy: A framework for the analysis of synchrotron tomographic data," *J. Synchrotron Radiat.*, vol. 21, no. 5, pp. 1188–1193, 2014.

[94] B. Münch, P. Trtik, F. Marone, and M. Stampanoni, "Stripe and ring artifact removal with combined wavelet-Fourier filtering," *EMPA Act.*, vol. 17, no. 2009–2010 EMPA ACTIVITIES, pp. 34–35, 2009.

[95] E. X. Miqueles, J. Rinkel, F. O'Dowd, and J. S. V. Bermúdez, "Generalized Titarenko's algorithm for ring artefacts reduction," *J. Synchrotron Radiat.*, vol. 21, no. 6, pp. 1333–1346, 2014.

[96] D. Jha, H. O. Sørensen, S. Dobberschütz, R. Feidenhans'L, and S. L. S. Stipp, "Adaptive center determination for effective suppression of ring artifacts in tomography images," *Appl. Phys. Lett.*, vol. 105, no. 14, 2014.

[97] T. Ferreira and W. Rasband, "The ImageJ 1.44 User Guide," *Manager*, pp. 1–199, 2011.

[98] ThermoFisher Scientific, "Thermo Scientific Avizo Software 9," p. 169, 2018.

[99] "Standard Test Method for Microindentation Hardness of Materials BT - Standard Test Method for Microindentation Hardness of Materials." 17AD.

[100] H. Galarraga, R. J. Warren, D. A. Lados, R. R. Dehoff, and M. M. Kirka, "Fatigue crack growth mechanisms at the microstructure scale in as-fabricated and heat treated Ti-6Al-4V ELI manufactured by electron beam melting (EBM)," *Eng. Fract. Mech.*, vol. 176, no. March, pp. 263–280, 2017.

[101] J. Tao, S. Hu, and L. Ji, "Effect of micromorphology at the fatigue crack tip on the crack growth in electron beam welded Ti-6Al-4V joint," *Mater. Charact.*, vol. 120, pp. 185–194, 2016.

[102] H. Do, "Fatigue crack growth threshold : implications ," vol. 19, no. 1, pp. 145–149, 1998.

[103] R. A. de Sousa, J. T. P. de Castro, L. F. Martha, and A. A. de Oliveira Lopes, "Improved Estimates of Plastic Zones Around Crack Tips Part 1: the Effects of the T-Stresses and of the Westergaard Stress Function," no. 1, 2011.

[104] R. I. Stephens, A. Fatemi, R. R. Stephens, and H. O. Fuchs, *Metal fatigue in engineering*. John Wiley & Sons, 2000.

[105] H. Gong, K. Rafi, H. Gu, G. D. Janaki Ram, T. Starr, and B. Stucker, "Influence of defects on mechanical properties of Ti-6Al-4V components produced by selective laser melting and electron beam melting," *Mater. Des.*, vol. 86, pp. 545–554, 2015.